UCRL-16279

University of California

Ernest O. Lawrence Radiation Laboratory

QUADRUPOLE COUPLING IN RARE EARTH CRYSTALS

TWO-WEEK LOAN COPY

This is a Library Circulating Copy which may be borrowed for two weeks. For a personal retention copy, call Tech. Info. Division, Ext. 5545

Berkeley, California

DISCLAIMER

This document was prepared as an account of work sponsored by the United States Government. While this document is believed to contain correct information, neither the United States Government nor any agency thereof, nor the Regents of the University of California, nor any of their employees, makes any warranty, express or implied, or assumes any legal responsibility for the accuracy, completeness, or usefulness of any information, apparatus, product, or process disclosed, or represents that its use would not infringe privately owned rights. Reference herein to any specific commercial product, process, or service by its trade name, trademark, manufacturer, or otherwise, does not necessarily constitute or imply its endorsement, recommendation, or favoring by the United States Government or any agency thereof, or the Regents of the University of California. The views and opinions of authors expressed herein do not necessarily state or reflect those of the United States Government or any agency thereof or the Regents of the University of California.

UNIVERSITY OF CALIFORNIA

Lawrence Radiation Laboratory
Berkeley, California

AEC Contract No. W-7405-eng-48

QUADRUPOLE COUPLING IN RARE EARTH CRYSTALS

Johan Blok

(Ph.D. Thesis)

September 1965

QUADRUPOLE COUPLING IN RARE EARTH CRYSTALS

Contents

ABSTRACT v

I. INTRODUCTION 1

II. THEORETICAL BACKGROUND 3

A. Nuclear Orientation 3

B. Orientation Parameters 4

C. Crystal Field Interactions 6

III. CRYOGENIC APPARATUS 9

A. Demagnetization Cryostat 9

B. Magnetic Thermometer 11

C. Electromagnet 13

D. Radiation Detectors 13

1. Scintillation counters 13

2. Semiconductor detectors 14

IV. QUADRUPOLE ANTISHIELDING 15

A. Introduction 15

B. The Cooling Salts 18

1. Neodymium ethylsulfate 18

2. Cerium magnesium nitrate 19

C. Experimental Technique 20

D. Experiments in NES 23

1. La^{140} 23

2. Eu^{154} 29

3. Gd^{159} 35

4. 7-day Lu^{177} 41

E. Experiments in CMN 49

1. La^{140} 49

2. Eu^{154} 58

3. Gd^{159} 59

4. 7-day Lu^{177} 59

F. Discussion 60

V. THERMODYNAMIC TEMPERATURE SCALE OF NEODYMIUM ETHYLSULFATE BELOW 1°K 66

A. Introduction 66

B. The T-T* Relationship for NES 66

1. Description of the method 69

2. Experimental procedure 70

C. The Thermodynamic Temperature Scale of NES at Extremely Low Temperatures 81

D. Discussion 85

VI. 155-DAY Lu^{177} 88

A. Introduction 88

B. The Decay Scheme 89

1. Source preparation 89

2. Coincidence experiments 90

3. Gamma-ray energies and relative intensities 95

C. Nuclear Orientation of Lu^{177m} 96

1. Alignment in NES 96

2. Relaxation effects in Lu^{177m} alignment 104

ACKNOWLEDGEMENTS 107

APPENDIX 108

REFERENCES 113

QUADRUPOLE COUPLING IN RARE EARTH CRYSTALS

Johan Blok

Lawrence Radiation Laboratory
University of California
Berkeley, California

July 23, 1965

ABSTRACT

The electric field gradient at the nucleus was obtained for the rare earth ethylsulfates and double nitrates of La^{+3}, Eu^{+3}, Gd^{+3}, and Lu^{+3} by measuring the quadrupole coupling constants via nuclear orientation. From a comparison with the calculated antishielding factor and the measured crystal field gradients we arrive at the ionic shielding factors for the rare earths. These shielding factors are observed to vary considerably through the rare earths. These experiments also yielded the nuclear quadrupole moment of La^{140}. We obtained $Q = +0.121(12)$ barns.

These measurements required a precise knowledge of the temperature susceptibility relationship for cerium magnesium nitrate and for neodymium ethylsulfate. The temperature scale for cerium magnesium nitrate has recently been determined quite accurately; thus it was used without reservations. For neodymium ethylsulfate, however, we determined the temperature scale at low temperatures using gamma-ray heating and nuclear orientation. We found considerable discrepancy with the previously published work.

We also made an exhaustive study of the decay of 155-day Lu^{177}. We determined the relative intensities and precise energies of many of the gamma rays in this complex decay. From nuclear orientation of the 7-day and the 155-day Lu^{177} isomers we determined the ratio of the nuclear quadrupole moments of the 155-day metastable state and the 7-day ground state. We found $Q_m/Q_g = +2.33(25)$. For gamma rays following the 1-second intermediate state in Hf^{177} we found the unattenuated value of the anisotropy. We conclude that no reorientation takes place in this 1-second state.

I. INTRODUCTION

It has been predicted theoretically[1,2] and established experimentally[3,4] that when an ion is placed in a paramagnetic salt unusually high field gradients are set up at the nucleus due to distortion of the closed electron shells of the ion by the external crystal field gradient (CFG). This field gradient could then interact with the nuclear quadrupole moment and give an appreciable contribution to the Spin Hamiltonian.[5] Thus at the sufficiently low temperatures (about 0.01 °K) obtained by adiabatic demagnetization of the paramagnetic salt, the nuclei will be aligned even in the absence of any other hfs interaction. This effect is especially noticeable in S-state ions since here all other alignment mechanisms are small.

We set out to determine the magnitude of the field gradient at the nucleus in the rare earth ethylsulfates and double nitrates. Isotopes of all available S-state rare earth ions were grown as impurities into neodymium ethylsulfate (NES) and cerium magnesium nitrate (CMN) lattices. Nuclear alignment gave the quadrupole coupling constant, P, in the Spin Hamiltonian, $\mathcal{H} = P[I_z^2 - 1/3I(I+1)]$, for each ion. Since P is simply related to the field gradient at the nucleus and since the antishielding factor γ_N has been calculated quite reliably we could arrive at a value of the crystal field parameter A_2^0 for each ion. These values combined with the CFG at the ionic site measured via optical spectroscopy[6,7] led to values of the ionic shielding factor of the CFG, γ_E. This shielding factor showed considerable variation throughout the rare earths.

Our experiments with Lu^{+3} led us to two interesting discoveries. The 7-day isomer of Lu^{177}, the isotope chosen for the antishielding studies, has a rather large anisotropy in the ethylsulfate; up to 20% at the lowest temperatures obtained. This fact enabled us to make a very careful study of the temperature dependence of the anisotropy. Instead of the linear behavior of anisotropy with reciprocal temperature which is expected for pure quadrupole alignment,[8] we saw rather striking deviations. A look at other work with isotopes aligned in NES showed deviations consistent with our findings. From thermodynamic and nuclear orientation

measurements on a single crystal of NES we obtained a new temperature scale which gave much better agreement with the nuclear orientation data.

Also, during the Lu^{177} experiments a new isomer of this nucleus was found.[9] Subsequent study of this isomer[10,11,12] has shown it to be a three quasiparticle state with the high spin of 23/2. Three rotational bands of up to eight members are populated in its decay. It was thus an interesting candidate for nuclear orientation studies and the recent development of very high resolution lithium-drifted germanium counters[13,14] made it experimentally feasible. The anisotropies have been compared with predictions based on the spectroscopically determined decay scheme.[11] For gamma rays following the 1-second intermediate state in Hf^{177} we found the full, unattenuated value of the anisotropy. No reorientation has therefore taken place during the 1-second lifetime of this state.

II. THEORETICAL BACKGROUND

A. Nuclear Orientation

The general theory of nuclear orientation has been adequately discussed elsewhere[8,15,16] and only those aspects relating to this work will be touched upon here.

Orientation of the nuclei of an assembly of paramagnetic ions in a crystal is normally accomplished through the interaction of the nuclear spin, I, with the high internal magnetic fields (about 10^5 Oe) set up at the nucleus by the unpaired electrons around it. These electronic fields are oriented in space by means of, (a), a small external magnetic field (several hundred gauss)[17,18] or (b), the interaction of the electrons with an inhomogenious crystalline electric field.[19] However, since no such large internal magnetic fields exist for closed-shell ions, which we are to consider here; these methods are not applicable and orientation is achieved by other means. The direct interaction of an external magnetic field with the nuclear dipole is negligible since the small value of the nuclear dipole moment requires immense fields (about 10^5 Oe), even at $0.01^{\circ}K$, to produce an appreciable orientation. Thus, the only orientation mechanism which is still available is the interaction of the nuclear quadrupole moment with the gradient of the internal electric field. The origin of this field will be discussed in Section II. C.

The splitting of the nuclear energy levels via interaction with the nuclear quadrupole moment is given by the Spin Hamiltonian[5]

$$\mathcal{H} = P(M^2 - \tfrac{1}{3}I(I+1)) \qquad (1)$$

where I is the nuclear spin, M its component along the quantization axis (the crystalline c-axis in our case), and P, the quadrupole coupling constant, is proportional to the product of the nuclear quadrupole moment and the electric field gradient. Since +M and -M are equivalent, the quadrupole interaction leads to alignment of the nuclei rather than polarization.

B. Orientation Parameters

The degree of orientation, and hence the value of the quadrupole coupling constant, P, may be learned from studying the behavior of gamma radiation emitted by radioactive, oriented nuclei. The angular distribution of gamma radiation from an oriented system of nuclei is given by

$$W(\theta) = \sum_k B_k U_k F_k P_k(\cos\theta) \tag{2}$$

where θ is the angle the detector makes with the quantization axis (the crystalline c-axis). The $P_k(\cos\theta)$ are Legendre polynomials and contain the sole angular dependence of the radiation. The F_k depend on the angular momentum properties of the observed nuclear decay $I_0 \xrightarrow{L} I_1$, and are defined by[20]

$$F_k = (-1)^{I_1 - I_0 - 1} \sqrt{2I_0+1}\,(2L+1)C(LLk;1-1)W(I_0 I_0 LL;kI_1) \tag{3}$$

where W is a Racah coefficient. Note that the properties of the Clebsch-Gordan coefficients require that F_k vanishes unless $k \leq 2L$.

The U_k arise because the initial state, I_0, in the observed decay is not the aligned nucleus. The gamma transition is preceded by a beta transition from the oriented state. The U_k for the transition $I \xrightarrow{L'} I_0$ are given by[8]

$$U_k = \sqrt{(2I+1)(2I_0+1)}\,(-1)^{I+I_0-L'} W(III_0I_0;kL'). \tag{4}$$

Note that it is assumed that the gamma transition occurs very soon after the beta decay so that the environment does not have time to interact with the intermediate state I_0. This may require a lifetime of less than 10^{-9} sec for the state I_0.

Finally, the factors B_k in Eq.(2) measure the degree of orientation of the nuclear ensemble. These are defined by[21]

$$B_k(I) = \sum_M \sqrt{2k+1}\, C(IkI;M0)W(M) \tag{5}$$

where W(M) is the population of the nuclear substate M. The population can be expressed in terms of the Boltzman distribution

$$W(M) = \frac{\exp(-E_M/kT)}{\sum_M \exp(-E_M/kT)} \tag{6}$$

where E_M is the energy of the M substate given by

$$E_M = P(M^2 - \tfrac{1}{3}I(I+1)). \tag{7}$$

From the properties of the Clebsch-Gordan coefficients involved in B_k it is readily seen that B_k vanishes unless $k \leq 2I$. From direct numerical calculations we also see that the magnitude of B_k falls off rapidly with increasing k, thus only the first few terms in Eq.(2) need be considered. Furthermore, for gamma radiation, and for all other parity-conserving transitions, terms with k odd vanish as well. The angular distribution of gamma radiation in our case can therefore be expressed simply as

$$W(\theta) = 1 + B_2 U_2 F_2 P_2(\cos\theta). \tag{8}$$

For $P \ll kT$ we can expand the Boltzman factor in Eq.(6) to obtain a closed expression for B_2, namely

$$B_2 = -\frac{1}{3}\frac{P}{kT}\sqrt{\frac{1}{5}I(I+1)(2I-1)(2I+3)}. \tag{9}$$

Thus at a fixed angle θ the radiation intensity should vary linearly with the reciprocal temperature.

C. Crystal Field Interactions

The filled electron shells around an ion have spherical symmetry in the free-ion state, therefore these electrons should set up no hyperfine fields at the nucleus. When the ion is placed in a crystal, however, the quadrupole component of the electric field set up by the charge points in the ionic lattice can perturb the closed-shell configuration of the electron cloud, the perturbed electrons then setting up a large field gradient at the nucleus which can interact with the nucleus through the nuclear quadrupole moment. In a simple-minded way, one can picture the crystal field gradient to be set up by two isolated lattice charges located at $+z$ and $-z$ with respect to the nucleus along the symmetry axis of the crystal. These charges tend to attract the orbital electrons of the ion away from the nucleus. The electrons in the plane perpendicular to the symmetry axis are thus on the average closer to the nucleus than those along the symmetry axis. The nucleus thus sees an effective quadrupole field set up by the distorted electron shells in the same direction as the crystalline electric field. Since the quadrupole interaction decreases very rapidly with distance, falling of as $1/r^3$ in fact, one predicts that the field gradient set up by the distortion of the orbital electrons, which are quite close to the nucleus, will be much greater than that set up by the lattice charges since these are several atomic diameters away. The net effect is thus a large amplification of the field gradient felt by the nucleus. This effect, first proposed by Sternheimer,[1] has been named antishielding. We designate the interaction Hamiltonian as

$$\mathcal{H} = V_C + V_Q. \tag{10}$$

Here V_C is the interaction of the crystal field with the electrons, having the leading term

$$V_2^{\,0} = A_2^{\,0} \sum_i (3z_i^{\,2} - r_i^{\,2}) \tag{11}$$

where i ranges over the electrons. The interaction of the electrons with the nuclear quadrupole moment is represented by V_Q and can be expressed as

$$V_Q = \frac{e^2 Q}{2I(2I-1)} \sum_i \left[\frac{I(I+1)}{r_i^3} - \frac{3(\vec{r}_i \cdot \vec{I})^2}{r_i^5} \right] \tag{12}$$

where Q is the nuclear quadrupole moment. The crystal field gradient can now act upon the nucleus in two ways. First, the direct interaction of the crystal field gradient upon the nuclear quadrupole; and secondly, via the second order mechanism

$$\frac{-2\langle {}^1S_0 | V_2^{\,0} | {}^1D_2 \rangle \langle {}^1D_2 | V_Q | {}^1S_0 \rangle}{E({}^1D_2)} \tag{13}$$

where ${}^1D_2$ represents the only electron configuration for which the matrix elements will not vanish and $E({}^1D_2)$ represents the energy of this configuration above the S-state ground level. We can combine the angular dependence of Eq. 13 into a nearly-constant multiplicative factor and obtain for the radial dependence:

$$A \frac{\langle {}^1S_0 | r^2 | {}^1D_2 \rangle \langle {}^1D_2 | r^{-3} | {}^1S_0 \rangle}{E({}^1D_2)} \tag{14}$$

where A contains the angular factors. We observe that to maximize Eq. 14 we must use an excited configuration near the ground state to minimize the energy denominator; as well as maximizing the numerator matrix elements. Estimates of these matrix elements using calculated wave functions show that about 80% of the antishielding contribution arises from the interaction with the $5p^5 6p$ excited state; i.e.

$$A \frac{\langle 5p^6 | r^2 | 5p^5 6p \rangle \langle 5p^5 6p | r^{-3} | 5p^6 \rangle}{E(5p^5 6p)} . \tag{15}$$

In this way Judd, Lovejoy, and Shirley,[4] using the tabulated radial wave functions for Pr^{+3} given by Ridley[22] and Rajnak[23]; showed that the

major contribution to the hyperfine structure of Eu^{+3}, in which magnetic effects are very small due to the singlet character of the ground state, was due to the interaction represented by Eq. 15.

III. CRYOGENIC APPARATUS

A. Demagnetization Cryostat

A schematic representation of the demagnetization cryostat is shown in Fig. 1. The glass vacuum chamber (A) is sealed by means of a Housekeeper seal to a copper sleeve. The copper sleeve is attached to a thin-wall stainless steel pumping tube (B) by means of a removable soldered joint. A radiation baffle (C) is placed in the bottom of the pumping tube to intercept room-temperature radiation from the upper end of the tube. The upper end of the pumping tube has access to a mechanical pump and a diffusion pump to evacuate the chamber, or to a cylinder of helium gas to fill the chamber with a small atmosphere of helium for convective heat exchange between the paramagnetic materials and the surrounding liquid helium bath (D). The liquid helium is contained in a glass dewar (E) with a glass pumping tube (F) through which the vacuum space is evacuated before filling the dewar with liquid helium. A stainless steel baffle (G) is placed above the liquid level to intercept room-temperature radiation from above. The space above the liquid helium can then be pumped down to an equilibrium pressure of about 60 microns of mercury by means of a mechanical pump. With this vapor pressure the temperature of the liquid helium is about 0.95°K. The helium bath pumping tube (H) also forms the support of the cryostat assembly. The helium dewar is surrounded by another double walled glass dewar (J) filled with liquid nitrogen to minimize the heat influx to the liquid helium. The whole assembly fits in the 2 5/8-inch gap between the poles of the electromagnet (K).

The single crystal of paramagnetic salt to be cooled (L) is suspended in the vacuum chamber from a long, 3-mm diameter glass rod attached to the lower end of the pumping tube (B). A glycerin slurry of chromium potassium alum and a compressed pill of manganous ammonium sulfate (M) are placed halfway up the glass rod. When they are demagnetized from the fringe field of the electromagnet they absorb any residual gas in the vacuum chamber and absorb any heat conducted down

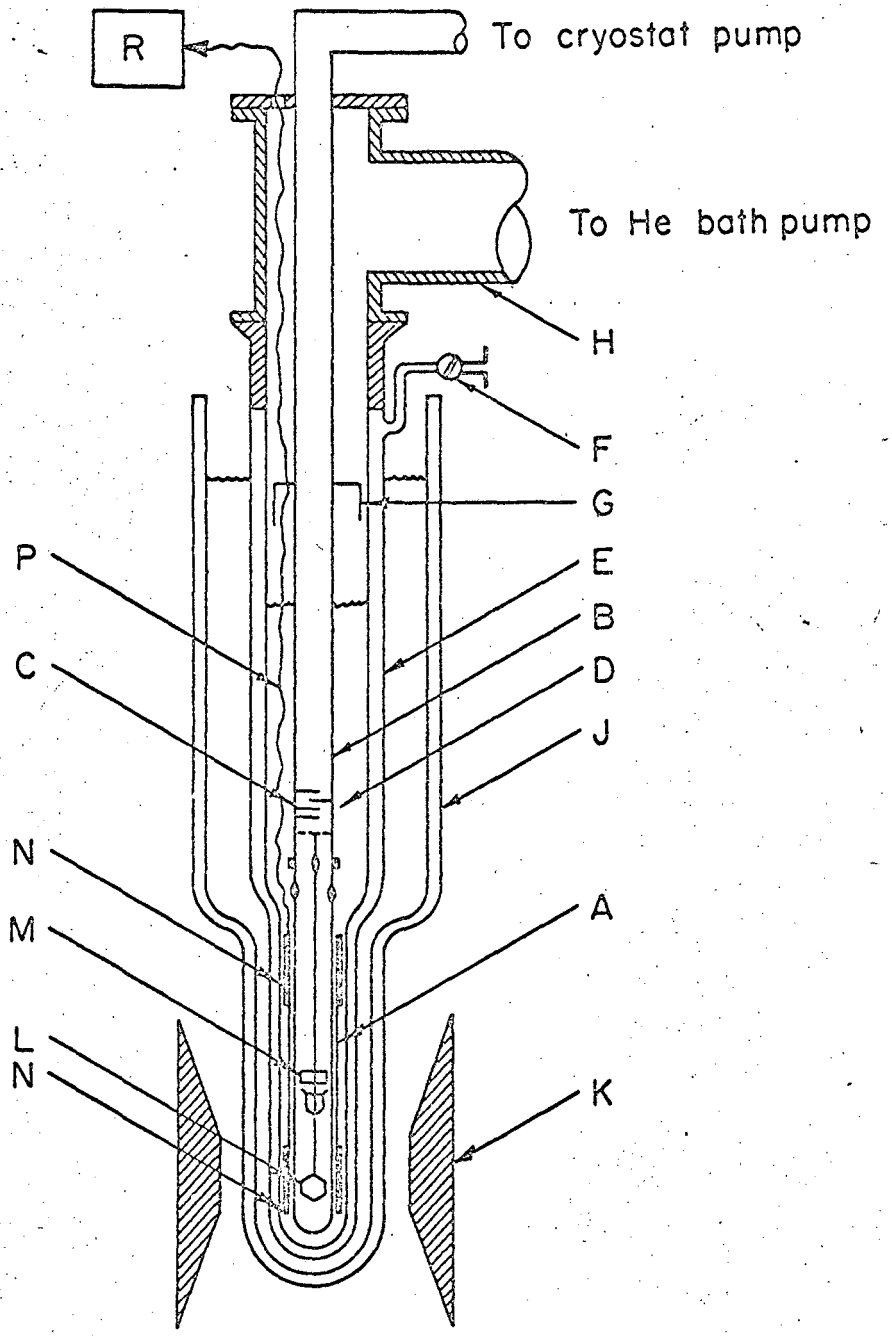

MU-36399

Fig. 1. Diagram of the demagnetization cryostat. The components are described in the text.

the glass rod. The glass vacuum chamber is painted with colloidal graphite to shield the paramagnetic salts from external radiation. The vacuum chamber is surrounded by mutual inductance coils (N) for susceptibility measurements. The leads from these coils (P) are taken out the top of the apparatus through a Kovar seal and are attached to a mutual inductance bridge circuit (R).

B. Magnetic Thermometer

Figure 1 shows two coaxially wound coil pairs surrounding the glass vacuum chamber of the cryostat (N). The lower coil-pair surrounds the paramagnetic single-crystal to be studied while the upper coil-pair surrounds no paramagnetic material whatever. A 20 cycle AC signal applied to the primary windings of the coil-pairs induces a voltage in each of the secondary windings. The difference between the two secondary voltages depends on the magnetic susceptibility of the paramagnetic crystal. Enough inductance is then added to the circuit from an external, calibrated mutual inductance bridge to give a zero net secondary voltage. The bridge used for this purpose is patterned after a previous model[24]; it allows the simultaneous adjustment of the amplitude and phase of the 20 cycle induced voltage. The net secondary voltage is amplified and fed to the vertical plates of an oscilloscope whose horizontal plates are driven by the primary signal. When the bridge is unbalanced, an elliptical pattern results. When the bridge is properly balanced the ellipse closes to a horizontal straight line. At the point of balance the amount of inductance added to the circuit from the bridge is a linear function of the magnetic susceptibility of the paramagnetic crystal in the cryostat. A schematic diagram of the bridge circuit is shown in Fig. 2.

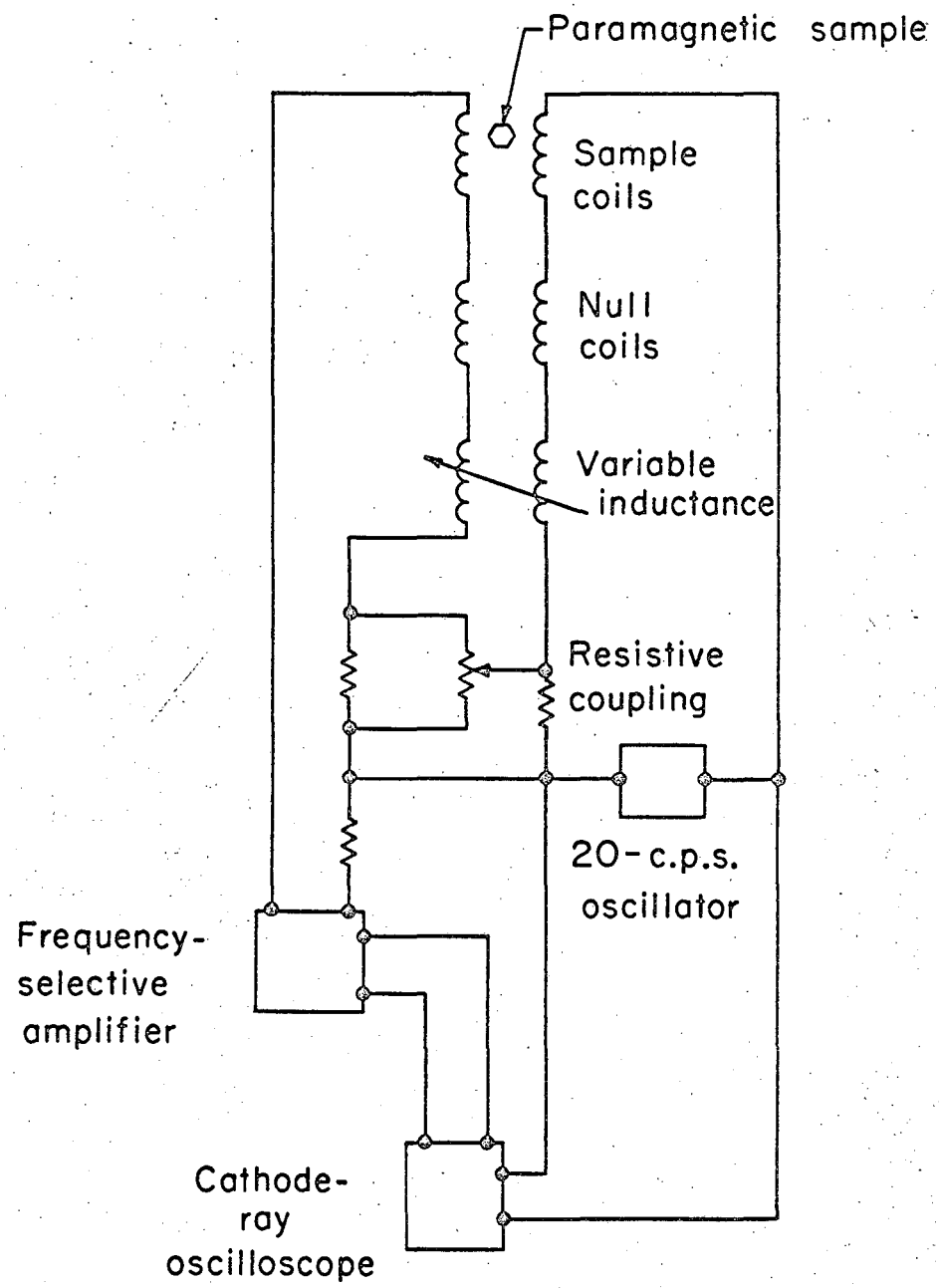

MU-36400

Fig. 2. Schematic of the mutual inductance bridge circuit used to measure the magnetic susceptibility of the paramagnetic salt at low temperatures.

C. Electromagnet

A water cooled, iron core electromagnet was used for adiabatic demagnetizations. The magnet, as well as its associated power supply was made by Spectromagnetic Industries of Hayward, California. The magnet pole tips tapered from a 12-inch to a 4-inch diameter over a distance of 1 1/2 inches leaving a usable space between the pole tips of 2 5/8 inches. The magnet was mounted on flanged wheels running along a track so that after demagnetization it could be rolled away to make room for gamma-ray counters or radioactive-heating sources.

The magnet power supply provided a maximum rectified current of 300 amps at 200 volts from a 208-volt, 60-cycle, 3-phase source. The transistorized regulator was capable of 0.001% regulation in the range 3 to 300 amps.

D. Radiation Detectors

1. Scintillation Counters

The early experiments were carried out using two NaI(Tl) scintillation counters. The crystals, 3-inch diameter by 3-inch long were mounted onto Dumont 6363 photomultiplier tubes. The output from the phototubes was fed through a preamplifier to a DD2 linear amplifier. The amplified pulses were sorted according to amplitude with a 256-channel pulse height analyzer (Technical Measurement Corp, North Haven, Conn.).

The scintillator-phototube-preamp combination was surrounded by an iron tube which served as a magnetic shield. The counters were positioned on an aluminum table equipped with flanged wheels. The table and the magnet moved along the same track, so the counting equipment could be rolled away while magnetization was in progress. The counters were mounted on aluminum bars, pivoted at the center of the table, which could slide over the table along a calibrated scale. In this way the counters could be accurately positioned at any angle with respect to the symmetry axis of the paramagnetic crystal in the cryostat.

To overcome these difficulties, we determined the antishielded crystal field gradient by direct measurement of the quadrupole coupling constant for ions in which the nuclear quadrupole moment was well-known. In general, such measurements will not yield the crystal field gradient unambiguously, since the 4f electrons also contribute to the field gradient at the nucleus. Furthermore, the magnetic hfs effects usually greatly exceed the quadrupole effect. For S-state ions, however, the 4f contribution vanishes so that the quadrupole coupling constant is due only to the crystal field gradient. In particular for the crystals of axial symmetry which we are to consider the quadrupole coupling constant is expressed simply as[45]

$$P = \frac{3eQ}{4I(2I-1)} \frac{\partial^2 V}{\partial z^2} . \tag{17}$$

In this equation Q is the nuclear quadrupole moment, e is the charge on one proton and I is the nuclear spin. The symmetry axis is taken along the z-direction. In the absence of electronic shielding the electrostatic potential, V, is given by

$$V = \frac{1}{-e} \sum_{n,m} r^n A_n^m Y_n^m(\theta,\phi). \tag{18}$$

Here, $-e$ is the charge on one electron and the $Y_n^m(\theta,\phi)$ are the usual spherical harmonics. In cartesian coordinates for crystals of axial symmetry, the leading term of Eq. 18 is

$$V_2^0 = \frac{1}{-e} A_2^0 (3z^2 - r^2). \tag{18a}$$

On differentiating twice with respect to z we obtain

$$\frac{\partial^2 V_2^0}{\partial z^2} = -\frac{4A_2^0}{e} . \tag{18b}$$

We multiply Eq. 18b by the antishielding factor, γ_N, to account for the antishielding effect of the electrons around the nucleus and obtain on substitution in Eq. 17:

$$P = \frac{3Q\gamma_N A_2^0}{I(2I-1)} . \tag{17a}$$

The Sternheimer antishielding factor, γ_∞ , is simply related to γ_N through the relationship $\gamma_N = 1 - \gamma_\infty$. Similarly we define the shielding factor γ_E, which is related to the usual ionic shielding factor σ_2 through the relationship $\gamma_E = 1 - \sigma_2$.

The S-state rare earth ions which occur in nature are tripositive lanthanum, gadolinium, and lutetium. La^{+3} and Lu^{+3} have a completely closed electron shell so that their spin Hamiltonian is simply given by Eq. 1. The magnetic hyperfine structure of Gd^{+3} has been experimentally determined[91] and is much smaller than the quadrupole splitting. Tripositive europium, although not an S-state ion, has no magnetic hyperfine structure since the ground state is a singlet, $^7F_0$. The quadrupole coupling constant arising from its six 4f electrons has been theoretically calculated,[29] thus the crystal-field contribution to the quadrupole coupling can also be determined for this ion. The crystal field gradients for the remaining rare earth ions were then obtained simply by interpolation.

B. The Cooling Salts

1. Neodymium Ethylsulfate

The ethylsulfates of all the lanthanide elements may be readily grown from aqueous solution. Their chemical composition is $M(C_2H_5SO_4)_3 \cdot 9H_2O$ where M^{+3} is the rare earth ion. The crystal structure of several members of the series, including neodymium ethylsulfate, has been determined by Ketelaar.[30] They form an isomorphous series of hexagonal prisms having a trigonal axis of symmetry. All the paramagnetic ions are equivalent and there is only one such ion per unit cell. Since it has historically been a favorite magnetic cooling salt, the thermal properties of neodymium ethylsulfate have been most intensively studied.

The Spin Hamiltonian of the neodymium ion can be written as[31]

$$\mathcal{H} = g_{\parallel}\beta H_z S_z + g_{\perp}\beta(H_x S_x + H_y S_y) + A S_z I_z + B(S_x I_x + S_y I_y) \qquad (19)$$

where $g_{\parallel} = 3.54$; $g_{\perp} = 2.07$; $S = 1/2$. For the odd isotopes, Nd^{143} and Nd^{145}, $I = 7/2$, $A = 0.0380$ and 0.0236, $B = 0.0199$ and 0.0124; while for the spin-zero even isotopes these quantities are zero. For a sample of natural abundance this leads to a magnetic specific heat, C, of $CT^2/R = 1.11 \times 10^{-3}$ at temperatures above about $0.25^{\circ}K$.

The magnetic properties of NES have been studied by Meyer.[32] The reliability of the relationship between the magnetic temperature and the absolute temperature which he derived has been questioned by several investigators however[33,34] and thus it seemed worth-while to repeat this measurement. The new measurements comprise Sec. V of this work.

2. Cerium Magnesium Nitrate

The rare earth double nitrates crystalize readily from aqueous solution as an isomorphous crystal series of chemical composition $A_2B_3(NO_3)_{12}\cdot 24H_2O$, where A is a trivalent rare earth ion and B is a divalent metal such as magnesium or zinc. Only the lighter rare earths form the double nitrate crystals; gadolinium magnesium nitrate being the heaviest to crystallize from solution. The heavier rare earths can be grown as impurity ions into the lighter double nitrates with varying degrees of success, however.

The crystal structure of cerium magnesium nitrate (CMN) has recently been determined[35] and is expected to be similar to that of the other double nitrates. The crystals are rhombohedral with space group $R\bar{3}$. The trivalent ions are all equivalent whereas the magnesium ions are of two kinds.

Since the ionic volume of the double nitrates is exceptionally large, the exchange interaction between ions is very small. Very low temperatures should therefore be reached upon adiabatic demagnetization of the salt. Similarly, the magnetic specific heat at these low temperatures should be rather low. Experimental determination of the thermal properties of CMN has verified these predictions.[36,37] The Spin Hamiltonian of the Ce^{+3} ion is given simply by:

$$\mathcal{H} = g_{\parallel}\beta H_z S_z + g_{\perp}\beta(H_x S_x + H_y S_y) \tag{20}$$

since there is no nuclear contribution for the spin-zero, even-even cerium isotopes. The g-factor is highly anistropic with $g_{\parallel} = 0.25$ and $g_{\perp} = 1.84$. The specific heat at low temperatures is extremely low, with $CT^2/R = 7.5 \times 10^{-6}$. Recently, the relationship between susceptibility and temperature has been accurately determined using nuclear orientation techniques.[33] We have used this new temperature scale to analize our CMN experiments.

C. Experimental Technique

The quadrupole coupling constant P, for the ions under investigation was obtained by determining the angular distribution of gamma radiation emitted by an oriented assembly of the nuclei as described in Sec. II. The desired isotope was substitutionally placed in the desired lattice by growing the crystal from a saturated solution of CMN or NES which contained a small amount of the active species. When the crystal contained roughly 100 microcuries of activity, it was removed from the growing solution, carefully dried, and washed several times with nonactive saturated solution. For this amount of activity, radioactive heating of the crystal was not an important factor. Approximately 1/2 erg per min was introduced from this source, compared to 20 to 30 ergs per min from extraneous sources for a typical crystal in the cryostat at low temperatures. A thin, nonactive layer grown around the active crystal prevented contamination of the apparatus through inadvertently touching the crystal. The crystal was then attached to a glass holder with "Duco" cement and this holder was in turn attached to the glass end of a tungsten-to-glass connection in the cryostat, as described in Sec. III. Likewise, a compressed pill of manganous ammonium sulfate and a glycerin slurry of chromium potassium alum was placed on the glass rod above the active crystal to reduce the conductive heat transfer to the crystal. When the cryostat was completely assembled as detailed in Sec. III, the sample chamber was opened to a helium atmosphere and the helium dewar was filled with liquid nitrogen, pre-cooling the entire asembly to $77^{\circ}K$. The sample chamber was then evacuated to about 10^{-6} mm Hg by pumping for 6 to 10 hours. The liquid nitrogen was then blown out of the dewar through a thin stainless-steel tube extending to the bottom of the dewar. The outer dewar was then filled with liquid nitrogen and the inner dewar filled with liquid helium. For heat exchange between the crystal and the bath, helium gas was admitted to about 10^{-3} mm Hg in the sample chamber. The temperature of the liquid helium was then lowered from $4.2^{\circ}K$ to about $0.96^{\circ}K$ through evaporative cooling by pumping away the

vapor above the boiling helium. At various intermediate temperatures, the susceptibility of the salt was measured to calibrate the mutual inductance bridge. The temperature of the helium bath was obtained from the 1958 He^4 vapor pressure scale[38] using a manometer to measure the pressure above the bath. At these temperatures, the paramagnetic salt behaves ideally; that is, the susceptibility follows Curie's law and a linear relationship is obtained between the mutual inductance bridge reading and the reciprocal temperature.

When the temperature of the salt had stabilized at the lowest temperature, the magnet was rolled around the cryostat and the field turned on. The relationship between magnetic field and power supply current had been previously determined using a rotating-coil gauss meter. The cryostat was then re-evacuated, the field turned off, the magnet rolled away, and the gamma-ray counters positioned around the cryostat. Two counters were usually used; located at 0° and 90°, the positions of maximum and minimum intensity in the radiation pattern. Radiation from the crystal was then counted for one to ten minutes, depending on the efficiency of the counter and the intensity of the gamma rays. Shorter counting periods than one minute usually gave insufficient statistical accuracy, while over periods of more than ten minutes electronic drifting in the counting circuit became a problem. Long counting periods also increase the uncertainty in temperature since extraneous heating warms the salt nonuniformly.[15] Upon completion of the counting period exchange gas was admitted to the sample chamber, bringing the salt back to the helium-bath temperature. At this temperature the radiation is essentially isotropic and so a normalizing count could be taken over the same time interval as before. Division of the "cold" count by the "warm" count then gave a radiation intensity distribution from the oriented nuclei independent of such unknowns as counter geometry and efficiency. The ratio of the cold count to the warm count can be written as

$$\frac{C}{W} = 1 + G_2(\Omega)G_2(B)B_2U_2F_2P_2(\cos\theta) \qquad (21)$$

where $G_2(\Omega)$ is the geometry correction and $G_2(B)$ is the background correction.

The geometry correction arises because the detector crystal intercepts a finite solid angle. The correction factors have been calculated for many scintillation-crystal shapes.[39] In our experiments the face of the detector was typically 10 to 20 cm from the radioactive source. At these distances the solid angle factor is typically between 0.90 and 0.97 for gamma-ray energies above 100 keV.

For an isotropic background, the background correction, $G_2(B)$, is given by

$$G_2(B) = \frac{P_w - B_w}{P_w} \tag{22}$$

where P_w is the integrated area under the photopeak for the warm count and B_w is that part of the area due to background. The expression for a nonisotropic background correction is somewhat more complex, being given by

$$G_2(B) = \frac{P_w - B_w}{P_w} + \frac{B_w}{P_w}\left(\frac{1 - \frac{C}{W}(B)}{1 - \frac{C}{W}(P)}\right) \tag{23}$$

where $\frac{C}{W}(B)$ is "cold-over-warm" for the background and $\frac{C}{W}(P)$ is "cold-over-warm" for the photopeak.

For very short-lived isotopes a further "decay" correction must be applied to the data. The radioactive decay rate can be written as

$$\frac{dN}{dt} = -N\frac{\ln 2}{\tau_{1/2}} \tag{24}$$

where $\tau_{1/2}$ is the half-life of the isotope and N is the number of atoms present. For time intervals small compared to $\tau_{1/2}$, Eq. 24 can be rewritten as

$$\frac{\Delta N}{N_0} = 1 - \frac{N}{N_0} \cong \frac{\ln 2}{\tau_{1/2}} \Delta t. \tag{25}$$

We must thus multiply the measured C/W by $(1 - \ln 2(\Delta t)/\tau_{1/2})$ to get the "true" anisotropy. In this expression Δt is taken as the time interval between the beginning of the cold count and the beginning of the warm count.

D. Experiments in NES

1. La^{140}

The experimental crystal field gradient V_2^0 for the rare earth ethylsulfates is plotted as a function of the number of 4f electrons in Fig. 3. The curve tends toward zero for the lighter rare earths and, indeed, becomes slightly negative at Pr^{+3}. This fact combined with the small quadrupole moment expected for the near-spherical La^{140} nucleus makes it exceedingly difficult to align this ion in the ethylsulfate. It was instructive, however, to see whether this negative value was due to a change in the crystal field parameter or in the shielding factor, γ_E. We measured the anisotropy of the 1597 keV gamma ray in the decay of La^{140} aligned in NES using a crystal with about 10 times the usual activity to obtain the necessary statistical accuracy. A multichannel analyzer is unsuitable for counting at such rapid rates since the counting rate is limited by the time it takes the analyzer to register a pulse. We therefore looked at the peak through a single channel analyzer, the output of which was fed to 5-mc scalars. Four experiments were performed from which we obtain $W(0)-W(90) = -0.0018(1.5)$ at $1/T = 50$, as shown in Table 1. Making suitable background and solid angle corrections we find $3/2\ B_2U_2F_2 = -0.0020(2)$.

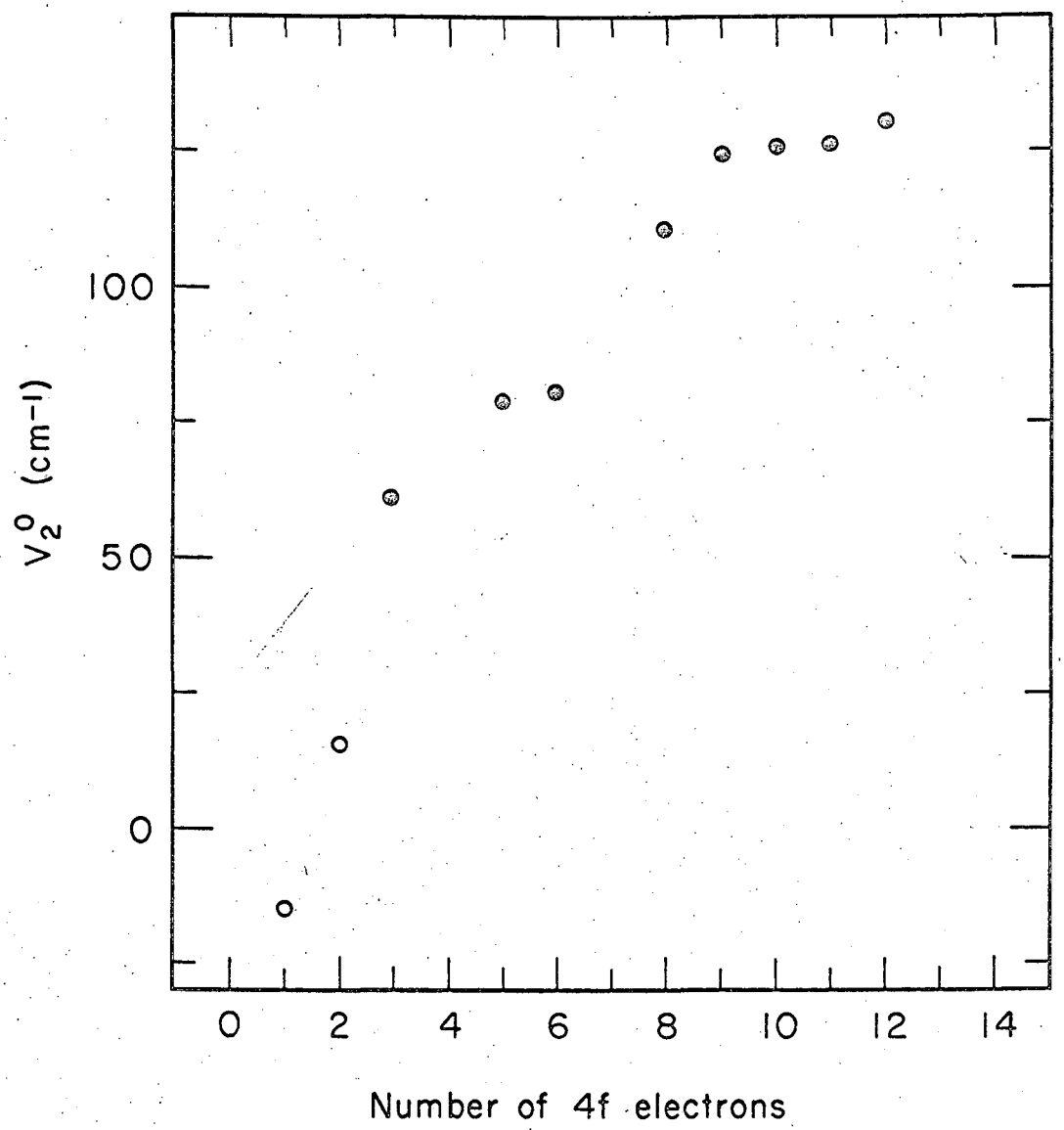

MU-36401

Fig. 3. The crystal field gradient at the 4f electrons of rare earth ions in the ethylsulfate crystal. The solid circles are from Refs. 60-63. The open circles are from Refs. 40 and 41.

Table I. Anisotropies observed for the 1597-keV gamma ray from La^{140} in NES. The error in the last figure is indicated in parentheses. The temperature of the measurements was 0.020(2) ^{o}K.

run	$\frac{3}{2}B_2U_2F_2$
1	+0.0016(16)
2	-0.0008(6)
3	-0.0021(3)
4	-0.0019(5)
weighted average	-0.0018(1.5)

Although the averaged data seem to indicate a negative value for $3/2\ B_2U_2F_2$, there was enough variation from one run to another to make us rather skeptical of the validity of the results. We therefore repeated the experiment later with much improved counting apparatus. We acknowledge the help of Mr. Milton Firth and Mr. Mon Lee in preparing an adequate counting system. We now used the newly developed "Goulding" type amplifier systems to supply both the linear amplifier and the single channel analyzer of the counting system. The gain of the system was kept constant using the digital gain stabilizers developed by Mr. Michiyuki Nakamura and Mr. Richard La Pierre at this laboratory. The gain stabilizers were used in connection with a Packard multichannel analyzer fitted with a routing system so that two spectra could be counted simultaneously. A sketch of the counting system is shown in Fig. 4. The results of this experiment are shown in Table IA and prove quite conclusively that $B_2U_2F_2$ is indeed negative for La^{140}. In fact, making suitable background and solid angle corrections we find $3/2\ B_2U_2F_2 = -0.0045(4)$ at $1/T = 98$. When the older data are corrected to the same temperature they yield $3/2\ B_2U_2F_2 = -0.0040(4)$ in good agreement.

It is impossible to calculate U_2F_2 exactly for the 1597-keV transition since the details of the preceding radiation sequence are not known. We estimate that $U_2 = +0.8$ within about 10%, however, and using $F_2 = -0.598$ we get $B_2 = +0.0063(6)$. Using Eq. 9 this leads to $P = -1.29(11) \times 10^{-5}\ cm^{-1}$. The negative value of P implies a positive value of $\gamma_N A_2^0$ as in all the other rare earths. The negative sign of the field gradient at the La^{+3} ion is therefore due to a change in sign of γ_E.

Comparing our value of P for La^{140} with that of Edmonds for La^{139} we can derive the quadrupole moment for La^{140} since:

$$Q_{140} = Q_{139}\frac{[PI(2I-1)]_{140}}{[PI(2I-1)]_{139}} . \qquad (26)$$

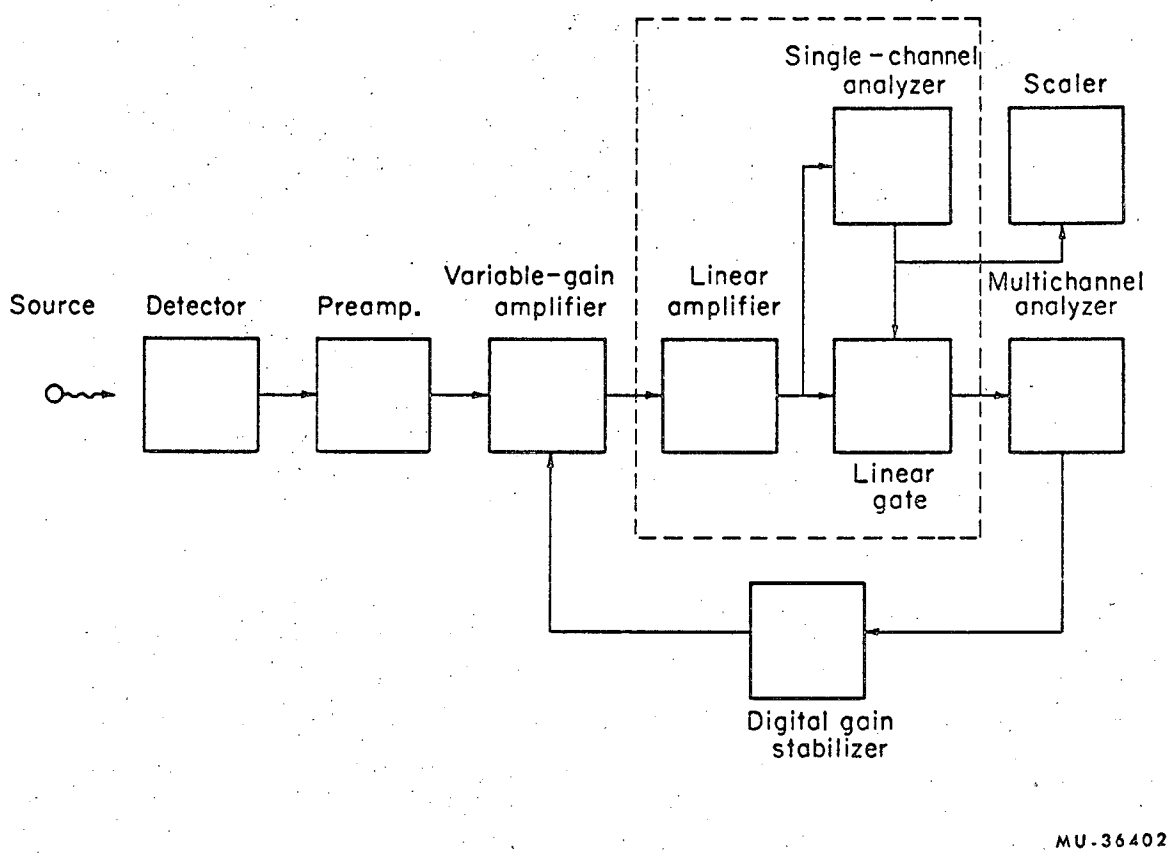

Fig. 4. High speed, ultra stable counting system. The components enclosed by the dashed line are an integral part of the "Goulding" amplifier system.

Table IA. Gamma-ray anisotropy for La^{140} in NES; confirmatory experiment. The counting rate in the 1597-keV peak was about 200,000 per minute in each detector. The temperature of all runs was about 0.01°K.

	uncorrected		corrected for decay	
run	W(0)-1	W(90)-1	W(0)-1	W(90)-1
2	+.0061	+.0074	+.0005	+.0018
3	+.0035	+.0080	-.0021	+.0024
4	+.0032	+.0070	-.0024	+.0014
5	+.0027	+.0052	-.0029	-.0004
6	+.0017	+.0083	-.0039	+.0027
7	+.0008	+.0052	-.0048	-.0004
8	+.0031	+.0078	-.0025	+.0022
9	+.0049	+.0062	-.0007	+.0006

Edmonds finds $P_{139} = 1.7 \times 10^{-5}$ cm^{-1} from nuclear magnetic resonance measurements of the quadrupole shift of the resonance at room temperature. Subsequent measurements over a range of temperature shows an increasing shift for lower temperatures, however, and extrapolating the data to $T = 0^{\circ}$ we find $P_{139} = 1.98 \times 10^{-5}$ cm^{-1} as the appropriate value for the quadrupole coupling constant.[89] Using $Q_{139} = 0.27$ barns, $I_{139} = 7/2$, and $I_{140} = 3$; we find $Q_{140} = +0.127(17)$ barns. At the same time Edmonds data gives $\gamma_N A_2^0 = +1.43(15) \times 10^4$ cm^{-1} a_0^{-2} where the sign is derived from the nuclear orientation data. Extrapolating the V_2^0 data of Fig. 3 to La^{+3} yields $V_2^0 \cong -30$ cm^{-1}. Using $\langle r^2 \rangle = 1.3a_0^2$ we obtain $\gamma_N/\gamma_E = -623(63)$.

2. Eu^{154}

The orientation of Eu^{152} and Eu^{154} in NES has been discussed earlier by other workers.[4,42] We have repeated the alignment of Eu^{154} using NaI(Tl) detectors and concentrating our attention on the 1277-keV gamma ray (see the decay scheme, Fig. 5). The gamma-ray spectrum is shown in Fig. 6. We concentrated our attention on the 1277-keV gamma ray because its resolution is best, its background is lowest, and it has the largest anisotropy. Measuring the anisotropy of the 1277 is thus the simplest check on the accuracy of the previous work. After applying a background correction of $G_2(B) = 0.95$ and a solid angle correction of $G_2(\Omega) = 0.92$ we obtained the temperature dependence of the anisotropy shown in Fig. 7. It is at once apparent that this anisotropy is rather lower than that obtained by Judd, Lovejoy, and Shirley[4] but that it is in excellent agreement with the earlier work of Shirley and Lovejoy.[42] D. A. Shirley has provided the original data books for the work reported in Ref. (4). From these data it can be seen that the unusually high anisotropies reported in Ref. (4) arise from an unrealistically high background correction that these authors applied to the data. We have thus reinterpreted the results of Judd, Lovejoy, and Shirley on this basis.

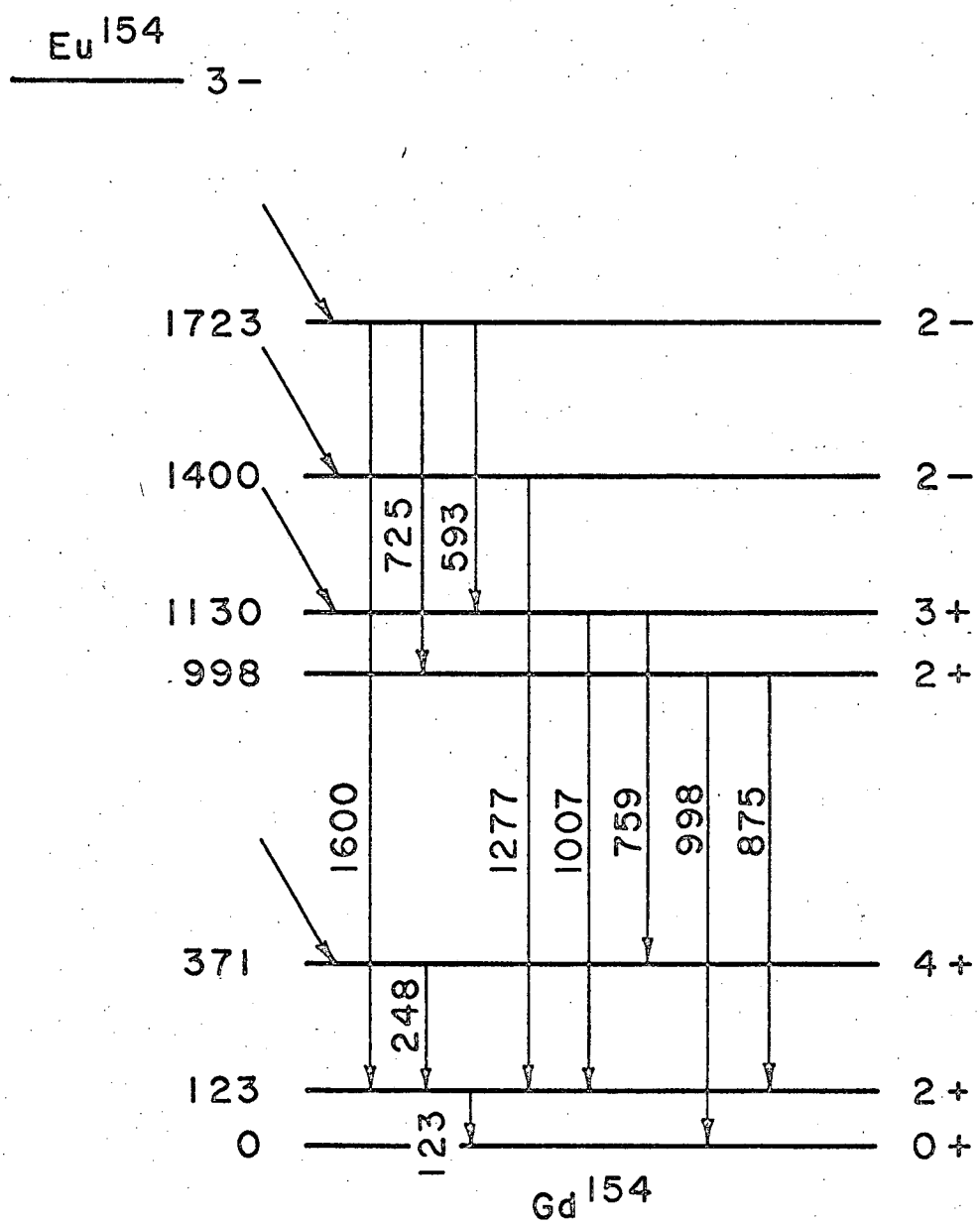

MU-36403

Fig. 5. Partial decay scheme of Eu^{154} from Ref. 4.

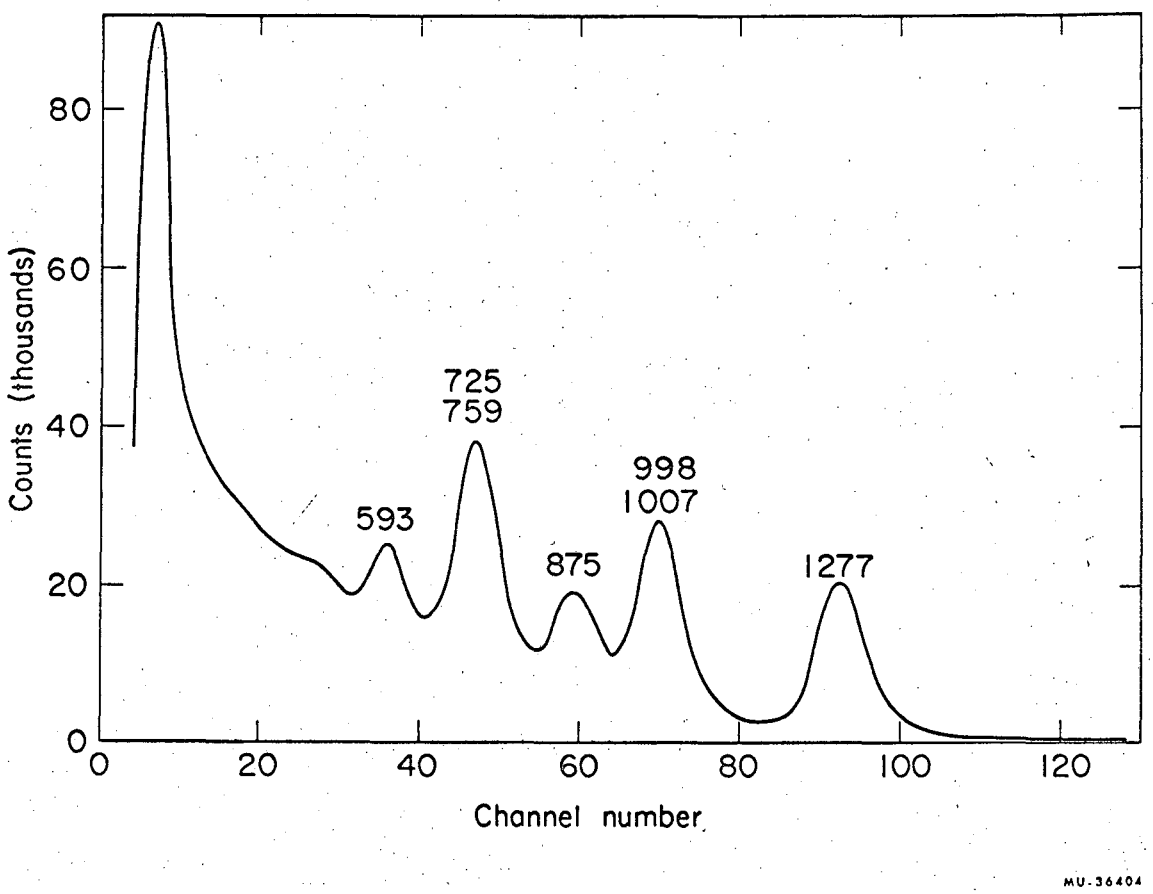

Fig. 6. Gamma-ray spectrum of Eu^{154} observed with a NaI(Tl) detector. Relevant energies are indicated in keV.

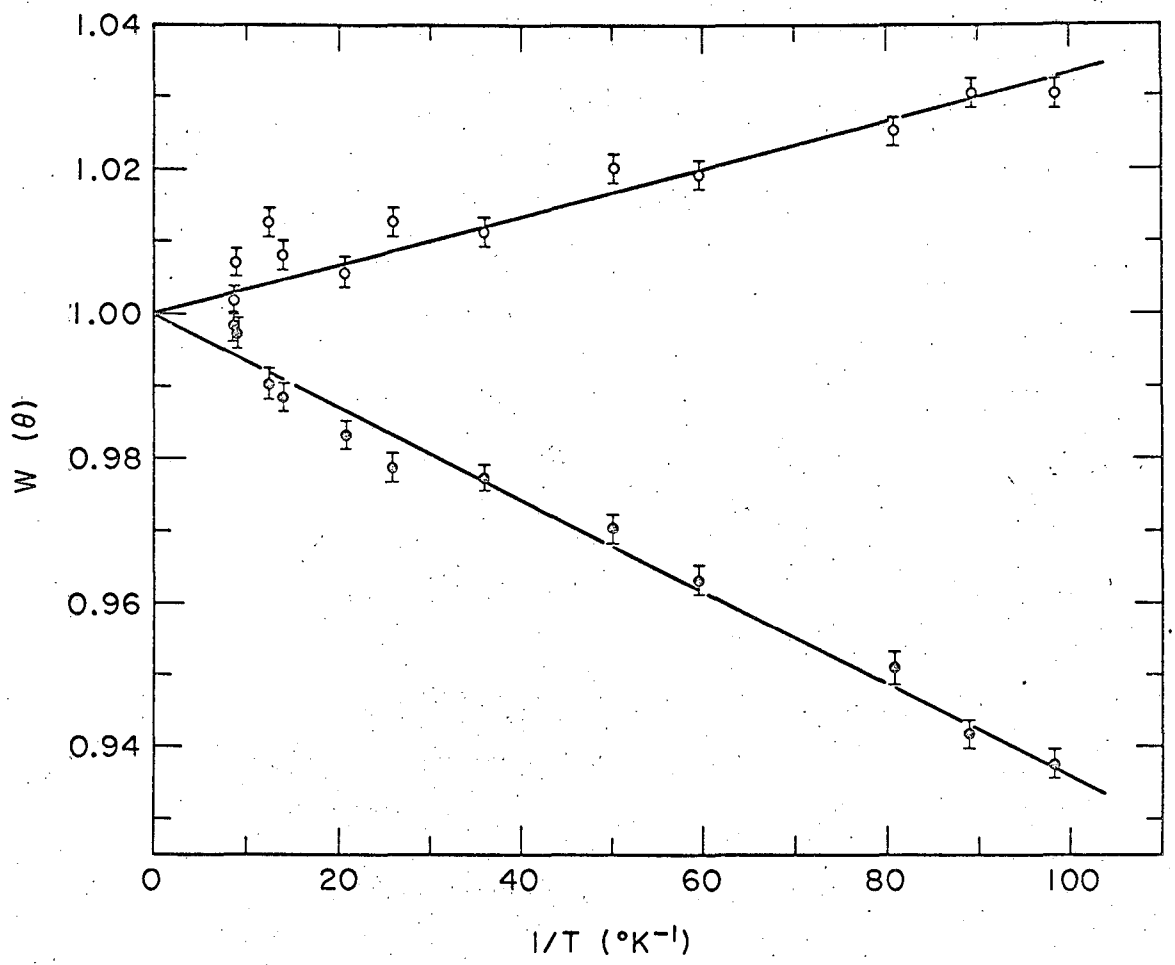

MU-36405

Fig. 7. Anisotropy as a function of reciprocal temperature for the 1277-keV gamma ray from Eu^{154} aligned in NES. Solid circles are for $\theta=0^{\circ}$ and open circles are for $\theta=90^{\circ}$.

We can calculate the quadrupole moment for Eu^{154} from the relationship

$$Q_{154} = Q_{152} \frac{P_{154}}{P_{152}} . \tag{27}$$

Since the relationship between P and B_2 can be written as

$$B_2 = - \frac{P}{3kT} \sqrt{\frac{1}{5} I(I+1)(2I-1)(2I+3)} \tag{9}$$

and since I is the same for both Eu^{152} and Eu^{154}, we can write

$$Q_{154} = Q_{152} \frac{B_2(154)}{B_2(152)} . \tag{28}$$

The derived quadrupole moment is thus independent of the value we assign to the temperature of the anisotropy measurement. Using the quadrupole coupling constants obtained by Shirley and Lovejoy for Eu^{152} and Eu^{154} and the nuclear quadrupole moment of Eu^{152} we obtained $Q_{154}=3.08(17)$ barns from Eq. (27).[43]

The 4f contribution to the quadrupole coupling constant of Eu^{+3} in the ethylsulfate has been calculated by Elliott[29] from the expression

$$P_{4f} = \frac{2e^2 Q A_2^{\,0} \langle r^2 \rangle}{I(2I-1)\Delta_2} \langle r^{-3} \rangle \, |\langle 2 \| \alpha \| 0 \rangle|^2 . \tag{29}$$

Using $I = 5/2$ and $\langle r^{-3} \rangle = 57 \text{Å}^{-3}$ he obtains $P_{4f} = +1.5Q \times 10^{-4}$ cm^{-1}, with Q expressed in barns. This value must be adjusted for the Eu^{154} spin, $I = 3$, and for the more recent value of $\langle r^{-3} \rangle = 49.1 \text{Å}^{-3}$.[44] We then obtain

$$P_{4f} = 1.5Q \times 10^{-4} \left(\frac{49.1}{57}\right) \left(\frac{5/2 \times 4}{3 \times 5}\right) = 0.85Q \times 10^{-4} \text{ cm}^{-1} .$$

The data of Fig. 6 yield $3/2\ B_2U_2F_2 = -.098$ at $1/T = 100$. For the decay sequence of the 1277-keV gamma ray we calculate $U_2F_2 = -.346$. Using Eq. (9) we find for the quadrupole coupling constant $P = -3.79 \times 10^{-4}\ cm^{-1}$. Using the value of the quadrupole moment derived above this becomes $P = -1.23Q \times 10^{-4}\ cm^{-1}$. Subtracting the 4f contribution we arrive at the crystal field contribution to the quadrupole coupling constant; viz,

$$P_{cf} = P - P_{4f} = (-1.23-0.86)Q \times 10^{-4} = -2.09Q \times 10^{-4}\ cm^{-1}.$$

Using Eq. (17a) we readily determine $\gamma_N A_2^0 = 2.9(3) \times 10^4\ cm^{-1}\ a_0^{-2}$. From Fig. 3 we may estimate $V_2^0 = \gamma_E A_2^0 \langle r^2 \rangle = 80\ cm^{-1}$ for europium ethylsulfate and from Freeman and Watson[6] we have $\langle r^2 \rangle = 0.83\ a_0^2$ for Eu^{+3}. Combining these data we can find for the ratio of antishielding to shielding factors.

$$\frac{\gamma_N}{\gamma_E} = \frac{\gamma_N A_2^0 \langle r^2 \rangle}{V_2^0} = \frac{(2.9 \times 10^4)(0.83)}{80} = +300(40).$$

3. Gd^{159}

The gamma-ray spectrum of Gd^{159} obtained with a NaI(Tl) detector is shown in Fig. 8. The temperature dependence of the anisotropy of the prominent 362-keV gamma ray is shown in Fig. 9. Gd^{159} has a rather short half-life of 18.5 hours, thus the experimental data must be corrected for decay as well as for solid angle and background. A solid angle correction of $G_2(\Omega) = 0.98$ was applied to the data. The background correction was trivially small, as one suspects from the spectrum of Fig. 8. The decay correction, $-\Delta N/N_0$, may be calculated from Eq. (25) as

$$-\frac{\Delta N}{N_0} = \frac{\ln 2}{\tau_{1/2}}\Delta t = \frac{\ln 2}{18.5 \times 60}\Delta t = 6.4 \times 10^{-4}\Delta t$$

with Δt expressed in minutes. The elapsed time between the start of the cold count and the start of the warm count was typically 3 1/2 minutes, a two minute counting period being used. The decay correction, $-\Delta N/N_0$, was thus about 0.25%.

From the decay scheme shown in Fig. 10 we note that the 362-keV transition must be purely E1, preceded by a pure Gamow-Teller beta decay. It is therefore a simple matter to calculate $U_2 = 0.749$ and $F_2 = +0.374$.

The Spin Hamiltonian for Gd^{+3} in the ethylsulfate has been given by Bowers and Owen[88] as

$$\mathcal{H} = g\beta\vec{H}\cdot\vec{S} + B_2^0 P_2^0 + B_4^0 P_4^0 + B_6^0 P_6^0 + A\vec{S}\cdot\vec{I} + P[I_z^2 - \tfrac{1}{3}I(I+1)]. \quad (30)$$

The energy splitting obtained with this Hamiltonian is shown in Fig. 11. In the absence of a magnetic field all terms in Eq. (30) are negligibly small compared to B_2^0 which is given by Bowers and Owen as $B_2^0 = 0.0067\ cm^{-1}$. The operator P_2^0 is defined as $3S_z^2 - S(S+1)$. With this Hamiltonian the doublet with $S_z = \pm 1/2$ will be lowest by $0.04\ cm^{-1}$ as shown in Fig. 11. The Nd^{+3} neighbors will set up a dipole-dipole field at the

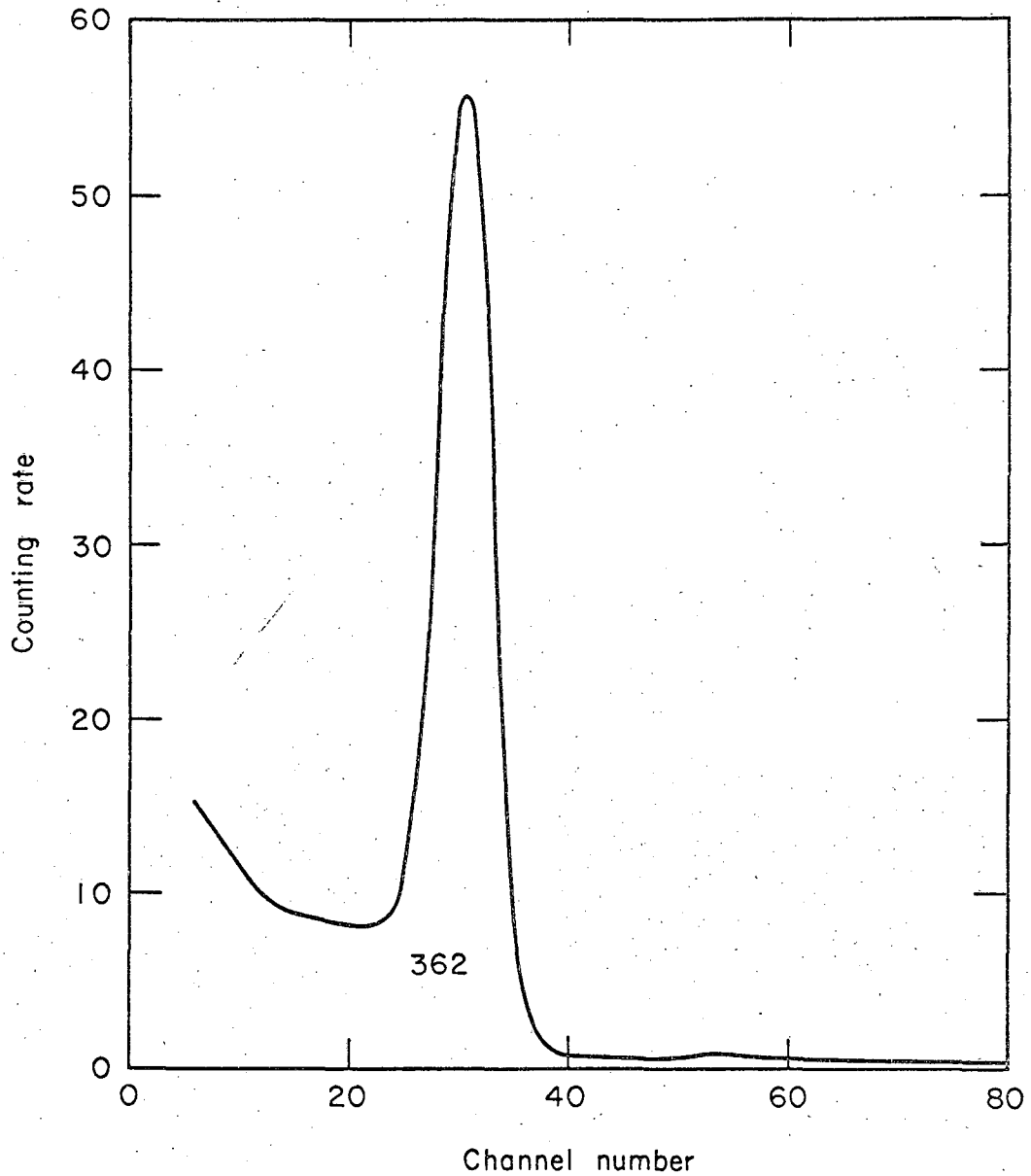

MU-36406

Fig. 8. Gamma-ray spectrum of Gd^{159} observed with a NaI(Tl) detector. Relevant energies are indicated in keV.

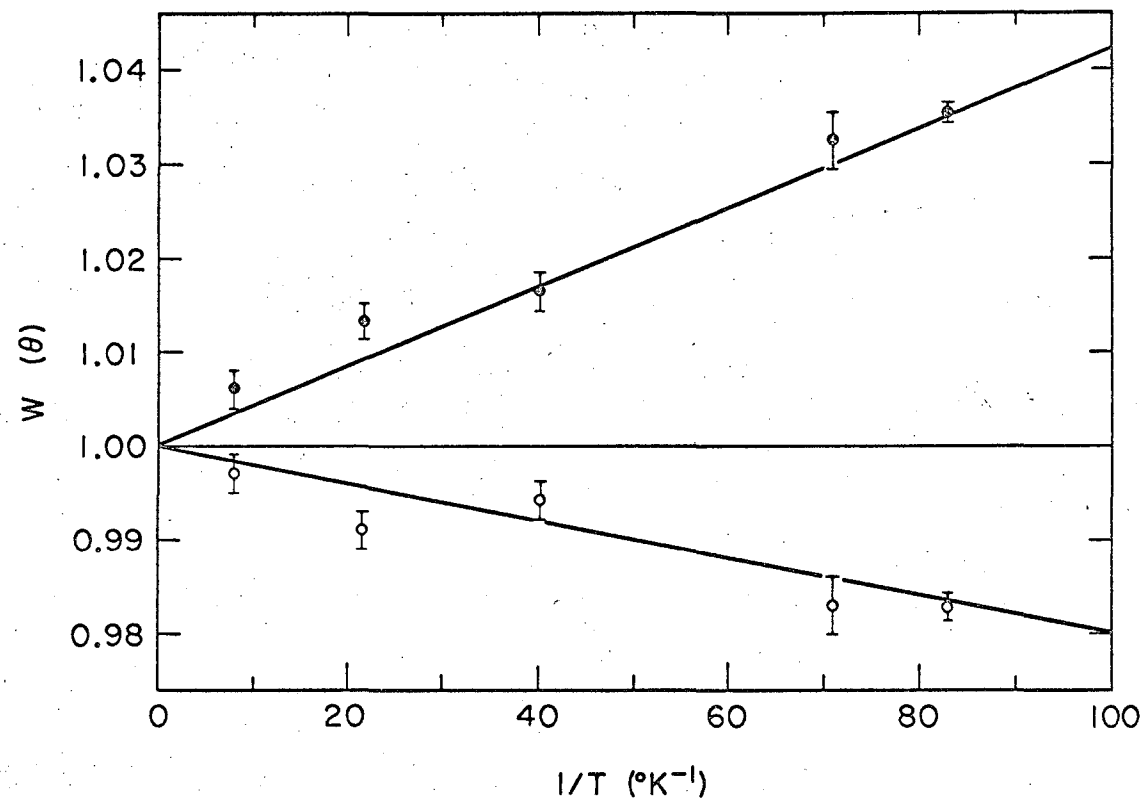

MU-36407

Fig. 9. Anisotropy as a function of reciprocal temperature for the 362-keV gamma ray from Gd^{159} aligned in NES. Solid circles are for $\theta=0^{\circ}$ and open circles are for $\theta=90^{\circ}$.

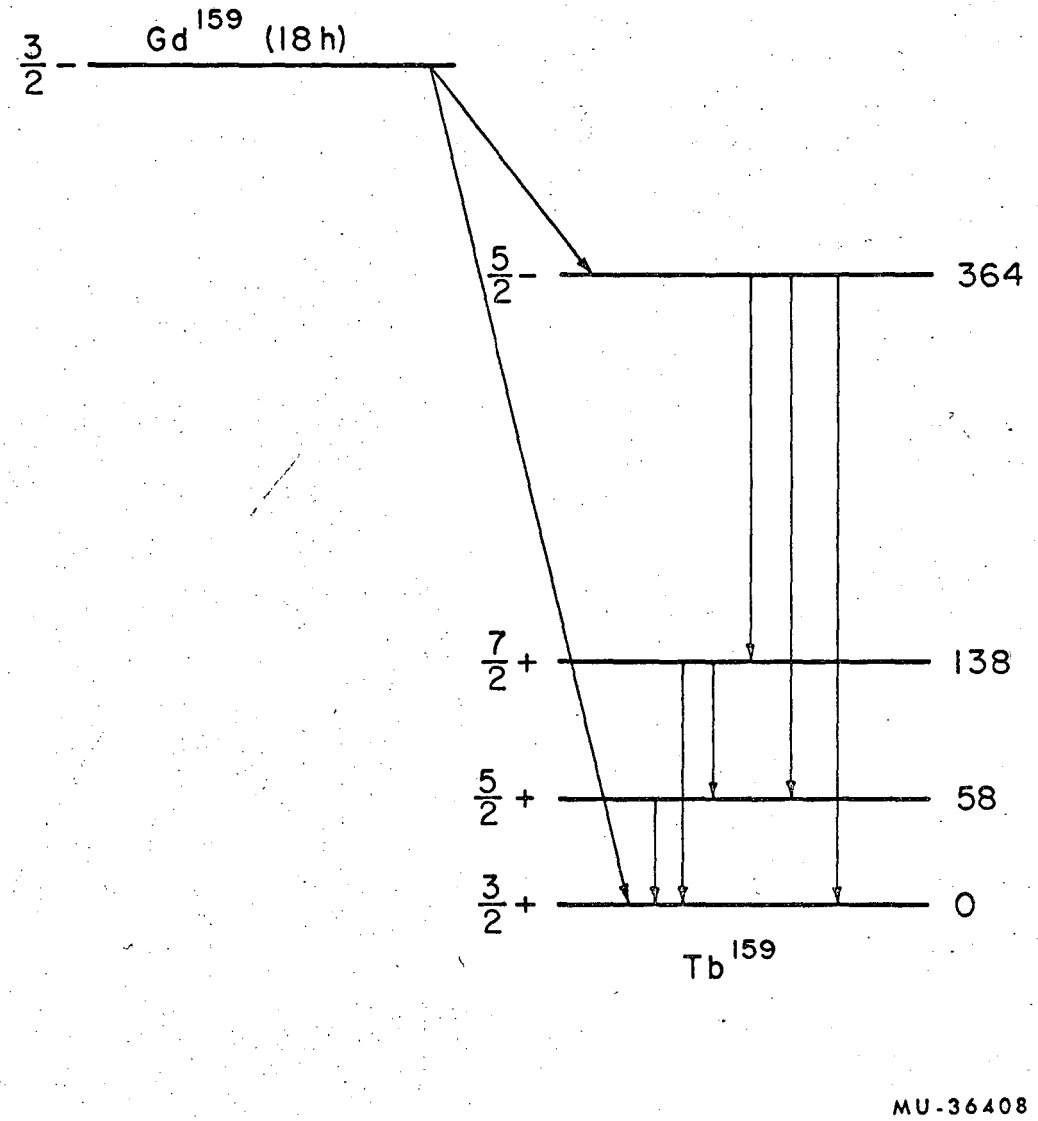

Fig. 10. Decay scheme of Gd^{159} from Ref. 72.

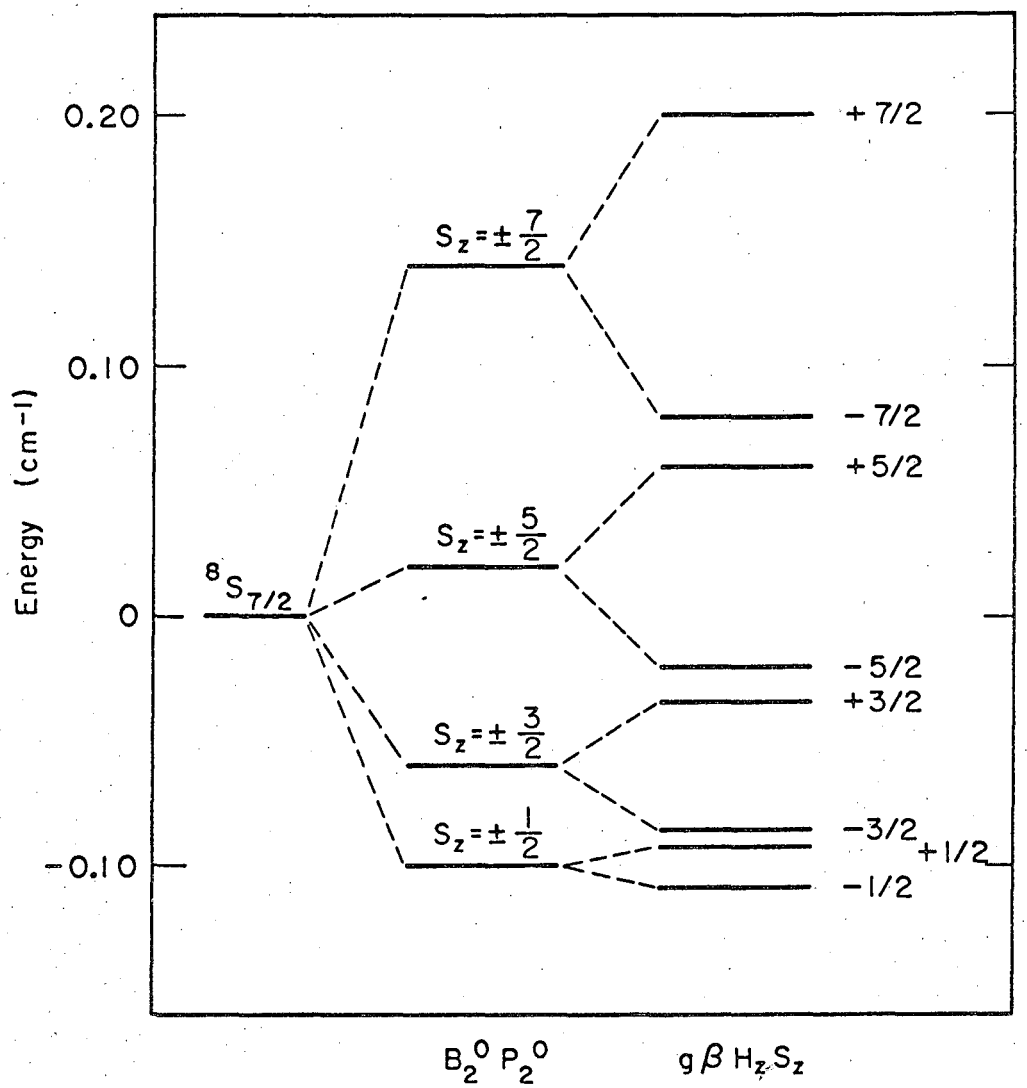

MU-36409

Fig. 11. Crystal field splittings experienced by the $^8S_{7/2}$ ground state of Gd^{+3} in the ethylsulfate. The spin Hamiltonian terms responsible for the splittings are indicated along the abscissa.

Gd^{+3} sites equal to $-2(\mu/r^3)$. We can idealize this field to one originating from two Nd^{+3} ions placed at $+r$ and $-r$ along the z-axis. Statistically, for about half the Gd^{+3} ions the Nd^{+3} neighbors will be antiparallel to each other, resulting in zero net field. For the remaining Gd^{+3} ions the Nd^{+3} neighbors will be parallel and will produce a field of $H = 2(2\mu/r^3)$ along the z-axis. Evaluating this expression for NES yields $H = 184$ gauss. Substituting this field into the first term of Eq. (30) we note that the $S_z = -1/2$, $S_z = +1/2$, and $S_z = -3/2$ levels are all within $0.026\ cm^{-1}$ of each other while the remaining levels are considerably higher. For half the Gd^{+3} ions with $H = 0$ we applied the Hamiltonian,

$$\mathcal{H} = A\vec{I}\cdot\vec{S} + P[I_z^{\ 2} - \tfrac{1}{3}I(I+1)],$$

to the $S_z = \pm 1/2$ doublet and for the remaining ions we applied the Hamiltonian $\mathcal{H} = g\beta HS_z + A\vec{I}\cdot\vec{S} + P[I_z^{\ 2} - 1/3I(I+1)]$ to the three levels $S_z = \pm 1/2, -3/2$ to calculate the temperature dependence of B_2 in terms of P. For both calculations we have used $A = 0.5 \times 10^{-3}\ cm^{-1}$,[91] $g = 1.99$, $S = 7/2$, and $I = 3/2$. The numerical calculations were performed with the computer program "PRIME". A satisfactory fit to the data was obtained for $P = -1.31(4) \times 10^{-3}\ cm^{-1}$.

To determine the field gradient from this value we must first estimate the nuclear quadrupole moment of Gd^{159}. This nucleus is in the strongly-deformed region between the $Z=50$ and the $Z = 82$ proton closed shells and the $N = 82$ and $N = 126$ neutron closed shells. The systematics for deformed nuclei should therefore be quite reliable in predicting the nuclear quadrupole moment. From the systematic variation of the nuclear quadrupole moment with the number of odd nucleons we estimate[45] $Q_0 = 7.8$ barns. Using the relationship[46]

$$Q = Q_0 \frac{I}{I+1} \cdot \frac{2I-1}{2I+3}. \qquad (31)$$

We obtain $Q = 1.56$ barns for the spectroscopic quadrupole moment. This value agrees qualitatively with $Q^{155} = 1.6$ and $Q^{157} = 2$, the spectroscopically determined quadrupole moments for Gd^{155} and Gd^{157}.[80] Using this value of Q and the measured value of P we find $\gamma_N A_2^0 = 2.35(24) \times 10^4\ cm^{-1}\ a_0^{-2}$. From Fig. 3 we may estimate $V_2^0 = \gamma_E A_2^0 \langle r^2 \rangle = 85\ cm^{-1}$ and from Freeman and Watson[6] we get $\langle r^2 \rangle = 0.785\ a_0^2$. We thus find for the ratio of antishielding to shielding factors: $\gamma_N/\gamma_E = +217(22)$.

4. 7-day Lu^{177}

In several respects Lu^{177} occupies a most favorable position for nuclear alignment via the quadrupole interaction. The element is the last of the rare earth series, thus one expects the crystal field gradient to be very large (see Fig. 3). Also, Lu^{177} is in the region of strongly deformed nuclei, thus it is expected to have a large intrinsic quadrupole moment. Finally, the spin of the Lu^{177} ground state is quite large, thus enhancing the orientation and leading to maximum anisotropy of the emitted radiation. These predictions are born out in fact, as seen in Fig. 12. Here we show the anisotropy of the 208-keV gamma ray (see the decay scheme, Fig. 13). The magnitude of the coefficient of P_2, nearly 20% at $\theta = 0^\circ$, makes very evident any irregularities in the temperature dependence, thus these data were primarily responsible for pointing out the error in the existing temperature-susceptibility relationship for NES. This relationship is more fully discussed in Sec. V.

In Fig. 14 we show the gamma-ray spectrum of Lu^{177} observed with a NaI(Tl) detector. Beside the low-energy x-ray peak, the 113-keV and the 208-keV gamma rays are clearly resolved. Since the 208-keV transition is pure E1 while the 113 keV is a mixed M1-E2 transition, we can obtain the dipole-quadrupole mixing ratio, δ, of the 113-keV transition by comparing the anisotropies. Here δ is given by

$$\delta = \frac{T(E2)}{T(M1)} . \qquad (32)$$

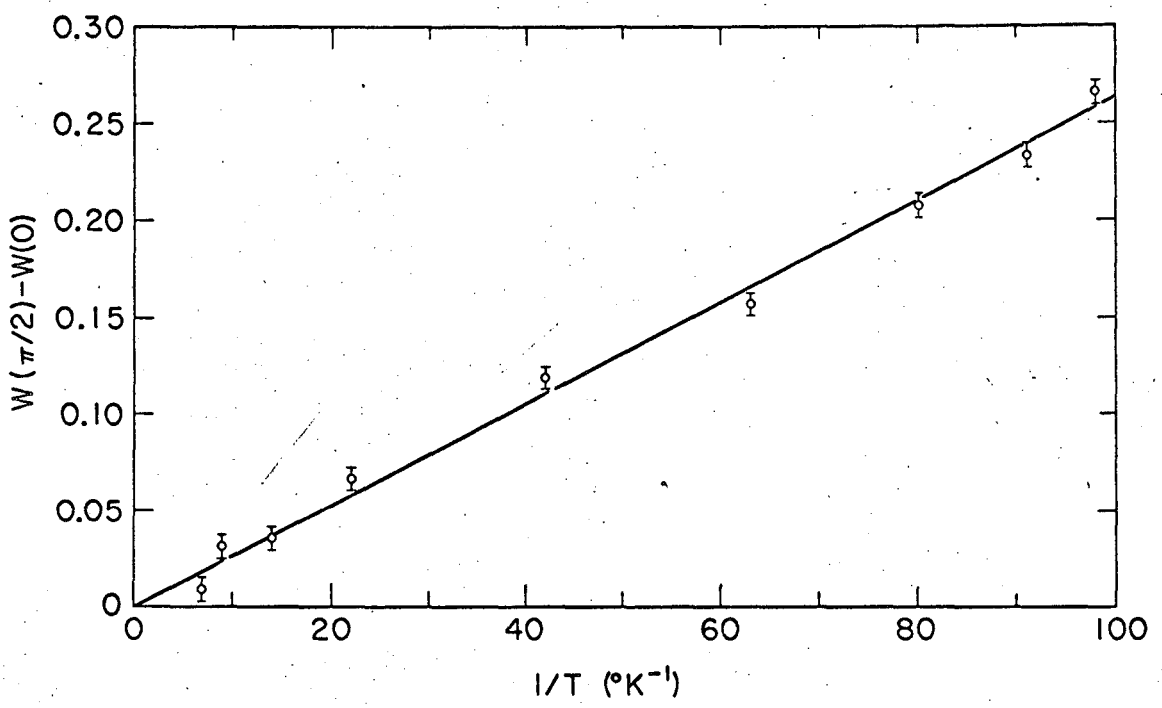

MU-36410

Fig. 12. 3/2 $B_2U_2F_2$ versus reciprocal temperature for the 208-keV gamma ray from 7-day Lu^{177} aligned in NES. The temperature was calculated from the T-T* correlation derived in Sec. V. The straight line is a theoretical curve for pure quadrupole alignment.

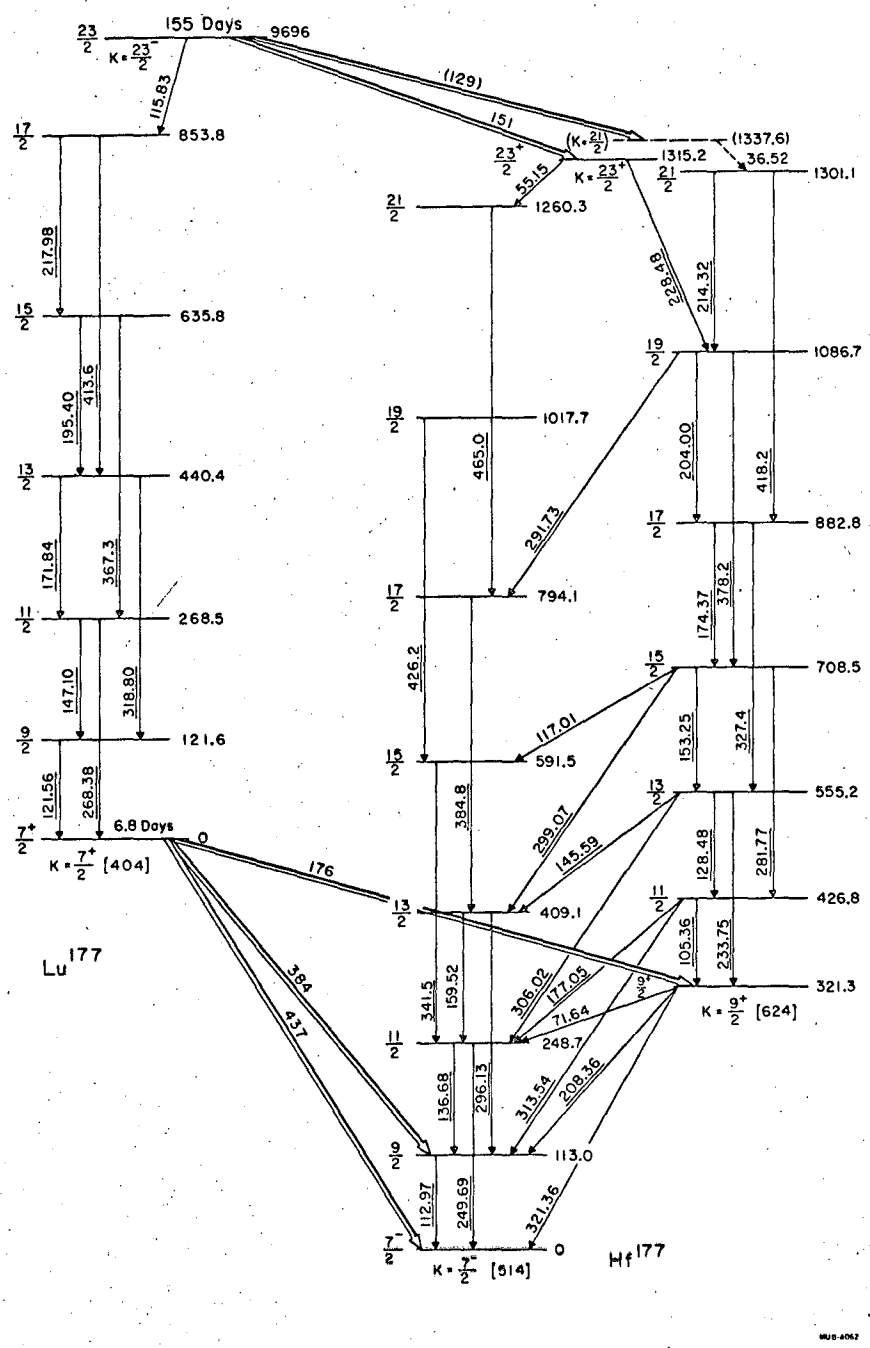

Fig. 13. Decay scheme of Lu^{177} taken from Ref. 11. We have added the I=19/2 level of the $K=7/2^{+}[514]$ band and its associated gamma ray. Energies of gamma rays above 318 keV are ours. We could observe only those gamma rays which are underlined.

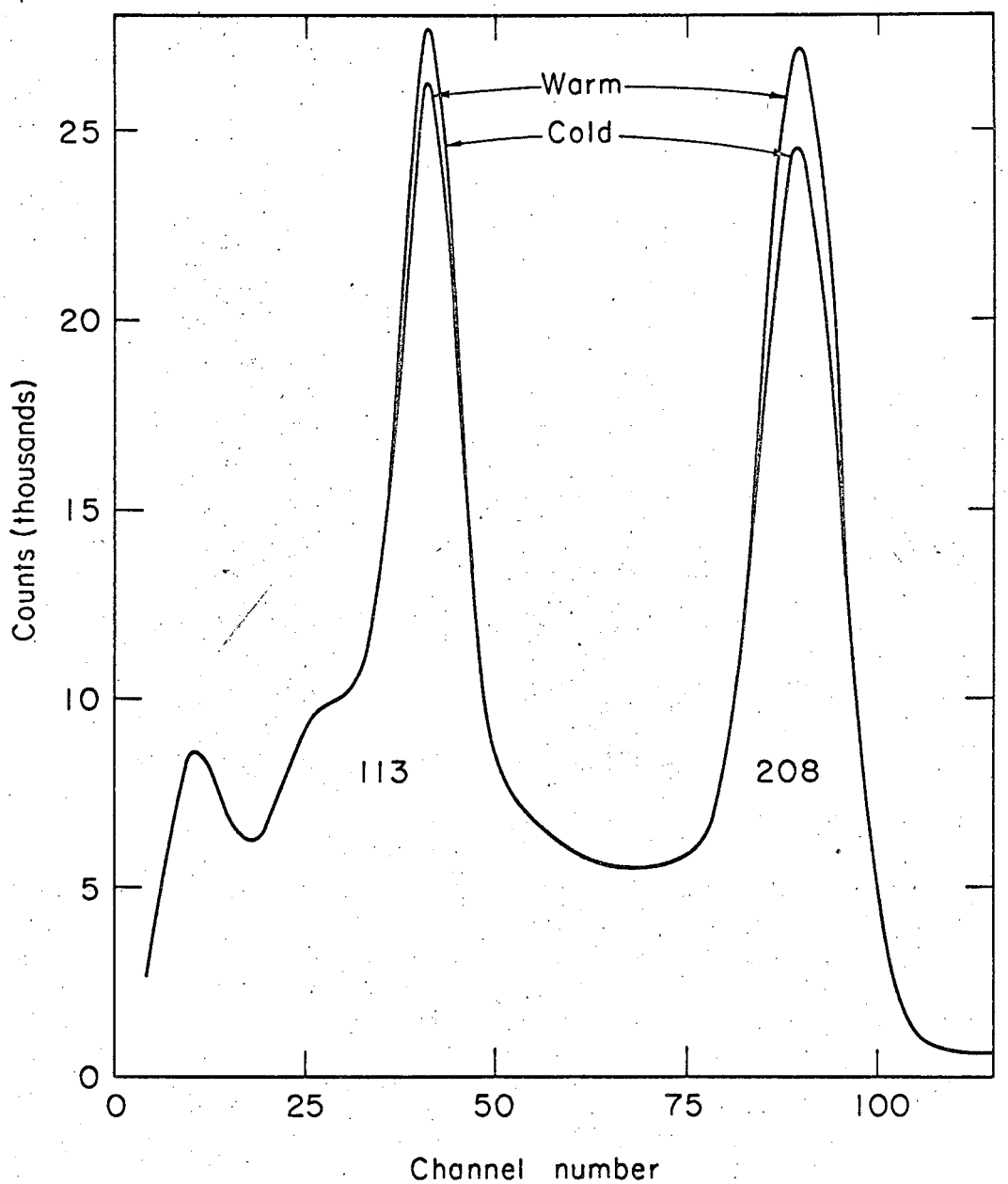

MU-36411

Fig. 14. Gamma-ray spectrum of 7-day Lu^{177} in NES observed with a NaI(Tl) detector. Relevant energies are indicated in keV.

Where T(M1) and T(E2) are the M1 and E2 transition probabilities, respectively. The temperature dependences of the anisotropy of the 208 keV, $9/2^+ \rightarrow 9/2^-$ transition and of the 113 keV, $9/2^- \rightarrow 7/2^-$ transition are shown in Fig. 12 and Fig. 15. The data have been corrected for the finite detector solid angle and for the isotropic background under the photopeaks. For the 208-keV gamma ray we have $G_2(B) = 0.87$ and $G_2(\Omega) = 0.98$, while for the 113-keV gamma ray we have $G_2(B) = 0.72$ and $G_2(\Omega) = 0.92$. From the 208-keV data we have $3/2\ B_2U_2F_2 = -0.263(10)$ at $1/T = 100$. We readily calculate $U_2 = +0.925$ and $F_2 = -0.440$ giving $B_2 = +0.431(16)$. For the 113-keV gamma ray we have $3/2\ B_2U_2F_2 = +0.93(15)$ at $1/T = 100$. To calculate U_2 for this gamma ray we have used roughly equal intensities for the allowed $7/2^+ \rightarrow 9/2^+$ beta decay and for the first forbidden $7/2^+ \rightarrow 9/2^-$ beta decay.[11] We have further assumed that the first forbidden decay is largely $L = 1$. We then calculate $U_2 = +0.870$ for the 113-keV gamma ray. Since B_2 must be the same for all gamma rays following the decay of 7-day Lu^{177} we calculate $F_2^{(113)} = +0.343(34)$. In Fig. 16 we have plotted F_2 as a function of the mixing ratio, δ, for this transition. Acceptable values of δ are in the regions where the theoretical curve overlaps the experimentally determined F_2. Transitions in the $7/2^-$ rotational band of Hf^{177} are characterized by a large degree of E2 character;[48] thus only the larger value of δ in Fig. 16 has physical significance. Using this value of $\delta = -4.7^{-.8}_{+.4}$ and the expression[11]

$$\frac{1}{\delta^2} = \frac{(g_k - g_R)^2}{Q_0^{\,2}} \frac{(2I + 2)(2I - 2)}{E_\gamma^{\,2}} (2.87 \times 10^5) \qquad (33)$$

we may calculate the g-factors, $(g_K - g_R)$, for the $7/2^-[514]$ rotational band of Hf^{177}. Using $Q_0 = 6.74$ from Ref. 47 we calculate $(g_K - g_R)^2 = 0.0012(2)$. Since the signs of $(g_K - g_R)$ and δ are the same[49] we find $(g_K - g_R) = -0.034(1)$. From the experimental ground state magnetic moment and M1 transition probabilities Bernstein and DeBoer[49] calculate $g_R = +0.215(14)$ in agreement with similar odd-N nuclides. This value,

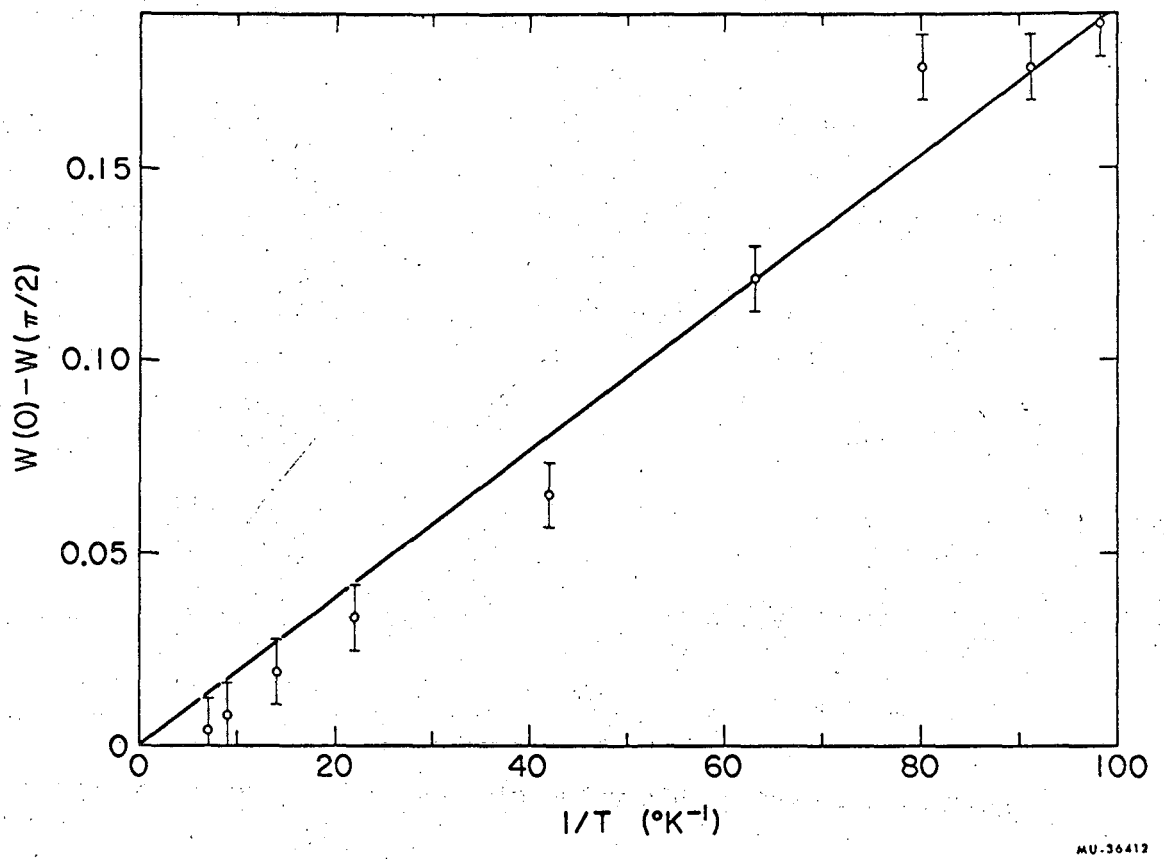

Fig. 15. 3/2 $B_2U_2F_2$ as a function of reciprocal temperature for the 113-keV gamma ray from Lu^{177} aligned in NES.

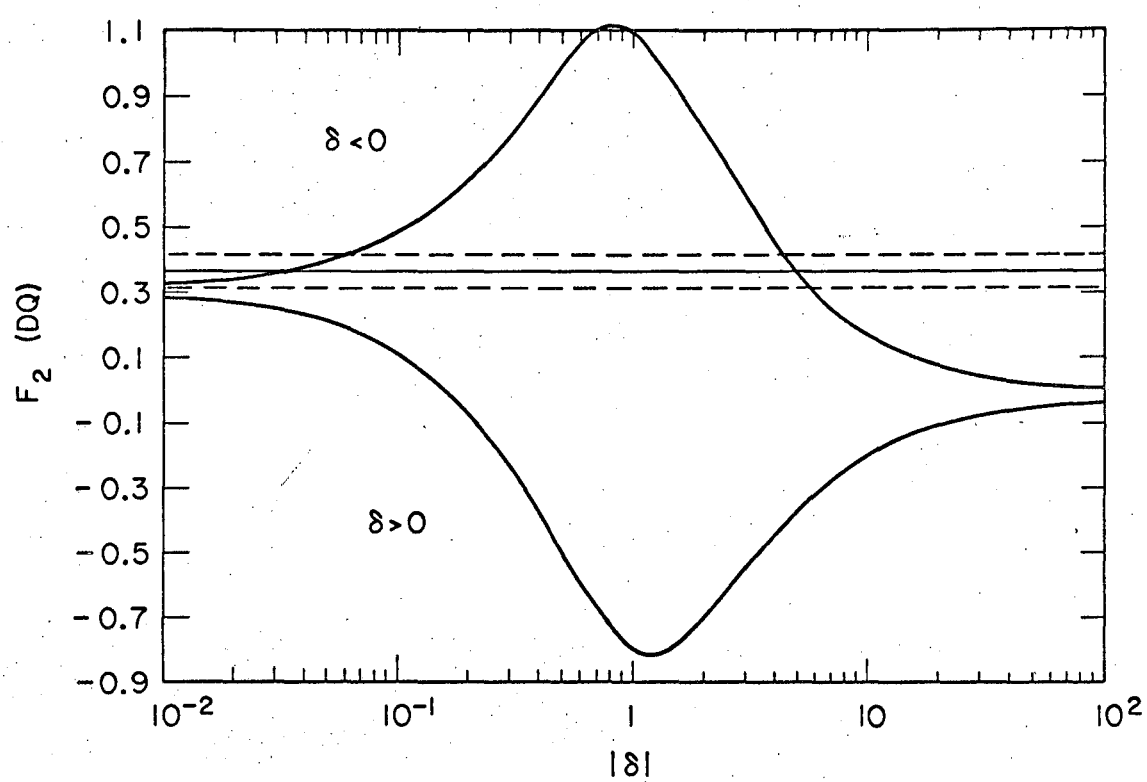

MU-36413

Fig. 16. Theoretical F_2 as a function of δ for the 113-keV transition in Hf^{177}. The spin sequence is 9/2(DQ)7/2 and the relationship between F_2 and δ is calculated from the expression:

$$F_2(DQ) = \frac{F_2(11I_fI_i) + 2\delta F_2(12I_fI_i) + \delta^2 F_2(22I_fI_i)}{1 + \delta^2}$$

using the notation and F_2 values from Ferentz and Rosenzweig.[20] The experimental value is designated by the horizontal line and the dashed lines represent the error limits. Acceptable values of δ are those regions in which the theoretical curve overlaps the experiment.

combined with our experimental $(g_K - g_R)$, yields $g_K = +0.18(2)$ in good agreement with Bernstein and de Boer's value of $+0.162(10)$. The theoretical value for the $7/2^-[514]$ state based on the Nilsson model[76] is $g_K = +0.41$. Such discrepancies between the experimental and theoretical intrinsic g-factor have been attributed by Rasmussen and Chiao to a quenching of the spin g-factor, g_s, of the unpaired nucleon.[77] These authors note that when a quenched g-factor, $g_s = -1.5$, is used for the unpaired neutron in the theoretical calculation instead of the free neutron value of $g_s = -3.826$, one obtains $g_K = +0.16$, in agreement with the experimental value.

For Lu^{177} in NES, the relationship $P/kT \ll 1$ is not a good approximation. Thus Eq. (9) cannot be used to calculate P from the measured B_2 and we must perform a rigorous calculation. Using the computer program "PRIME" to calculate B_2 we find good agreement with the 208-keV data when we choose $P = -6.1(2) \times 10^{-4}$ cm^{-1}. To derive the field gradient we must again estimate the nuclear quadrupole moment. Townes[45] gives $Q_0 = 7.8$ for the intrinsic quadrupole moment, from which we may calculate $Q = 3.6$ for the spectroscopic quadrupole moment. Using this value, we obtain

$$\gamma_N A_2^0 = 3.32(11) \times 10^4 \text{ cm}^{-1} a_0^{-2}.$$

From Fig. 3 we again estimate $V_{2_2}^0 \equiv \gamma_E A_2^0 \langle r^2 \rangle \cong 130$ cm^{-1} and from Freeman and Watson[6] $\langle r^2 \rangle = 0.588\ a_0^2$. We thus obtain for the ratio of antishielding to shielding factors $\gamma_N/\gamma_E = +150(10)$.

E. Experiments in CMN

The crystal field gradient existing at the rare earth site in the double nitrate has been measured via optical spectroscopy.[7] Since only the rare earths from lanthanum to gadolinium will form double nitrate crystals from solution, the data necessarily stop at this point. The experimental data indicate that the shielded CFG, V_2^0, varies rather smoothly from -86 at La^{+3} to about zero at Gd^{+3}, as shown in Fig. 17. Extrapolating the data beyond this point is rather inconclusive since the field gradients could either cross the abcissa to become large and positive or they could approach zero asymptotically to Lu^{+3}.

1. La^{140}

We prepared La^{140} by neutron bombardment of La^{139} as the oxide. It was readily grown into a CMN crystal which was then mounted in the cryostat in the usual way. From the complex decay scheme for La^{140} shown in Fig. 18, four gamma rays stand out sharply in a NaI(Tl) spectrum. These are the 329-keV $3^+ \rightarrow 4^+$; the 490-keV $4^+ \rightarrow 2^+$; the 815-keV $3^+ \rightarrow 2^+$; and the 1597-keV $2^+ \rightarrow 0^+$ transitions. The spectrum is shown in Fig. 19. In Table II we show the anisotropy for three of these gamma rays at $1/T = 500$, the lowest temperature reached with CMN cooling. The 329-keV peak shows a quite small anisotropy and rides on a large, anisotropic background. Its anisotropy could therefore not be measured with any degree of certainty. The short half life of La^{140} requires that a decay correction be made to the data. We obtain for 10 min from the start of the cold to the start of the warm count,

$$\frac{\Delta N}{N_0} = \frac{\ln 2}{40 \times 50}(10) \cong 0.30\%.$$

A solid angle correction of $G_2(\Omega) = 0.95$ was applied to the data. From Fig. 19 we note that the lower energy gamma rays ride on an appreciable background; the background corrections are thus quite large. The background

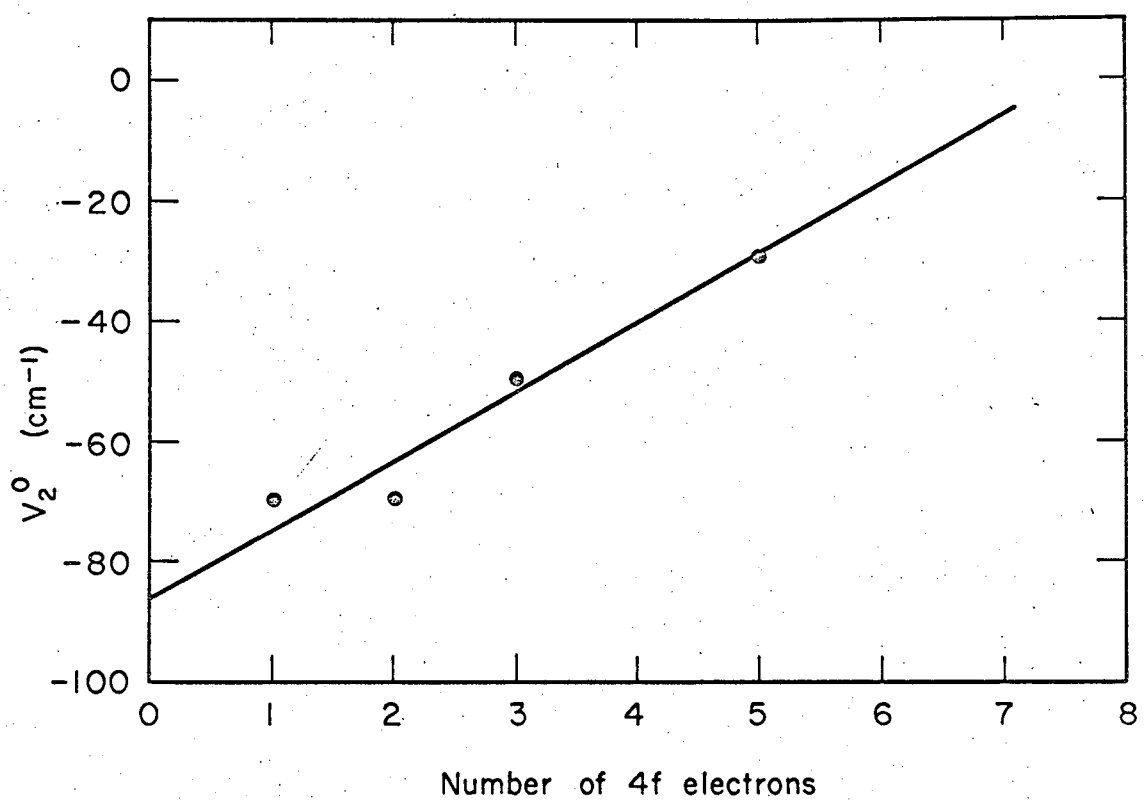

MU-36421

Fig. 17. The crystal field gradient at the 4f electrons of rare earth ions in the double nitrate crystal. The experimental points are from Judd.[7]

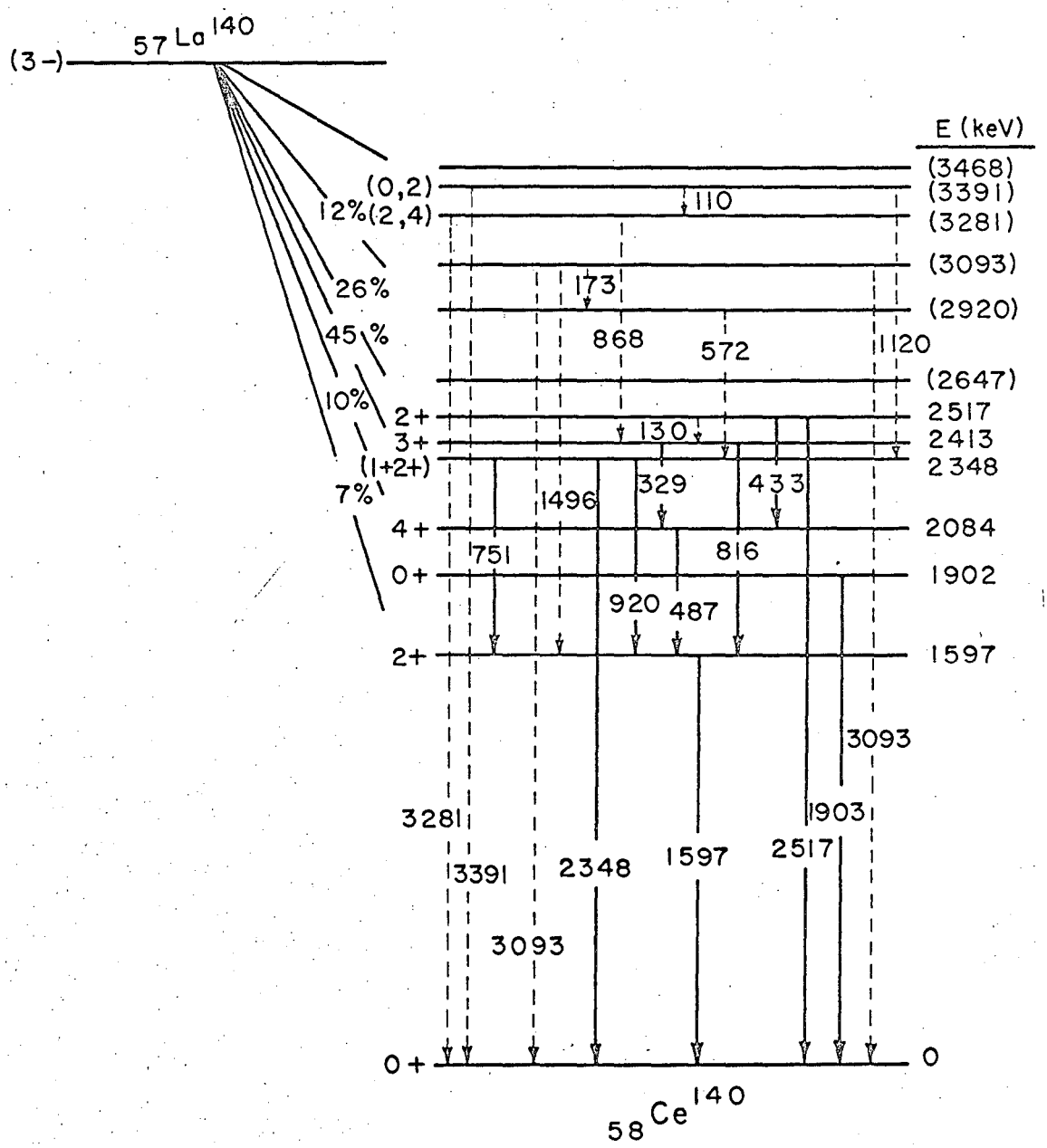

MU-34780

Fig. 18. Decay scheme of La^{140} from Ref. 50.

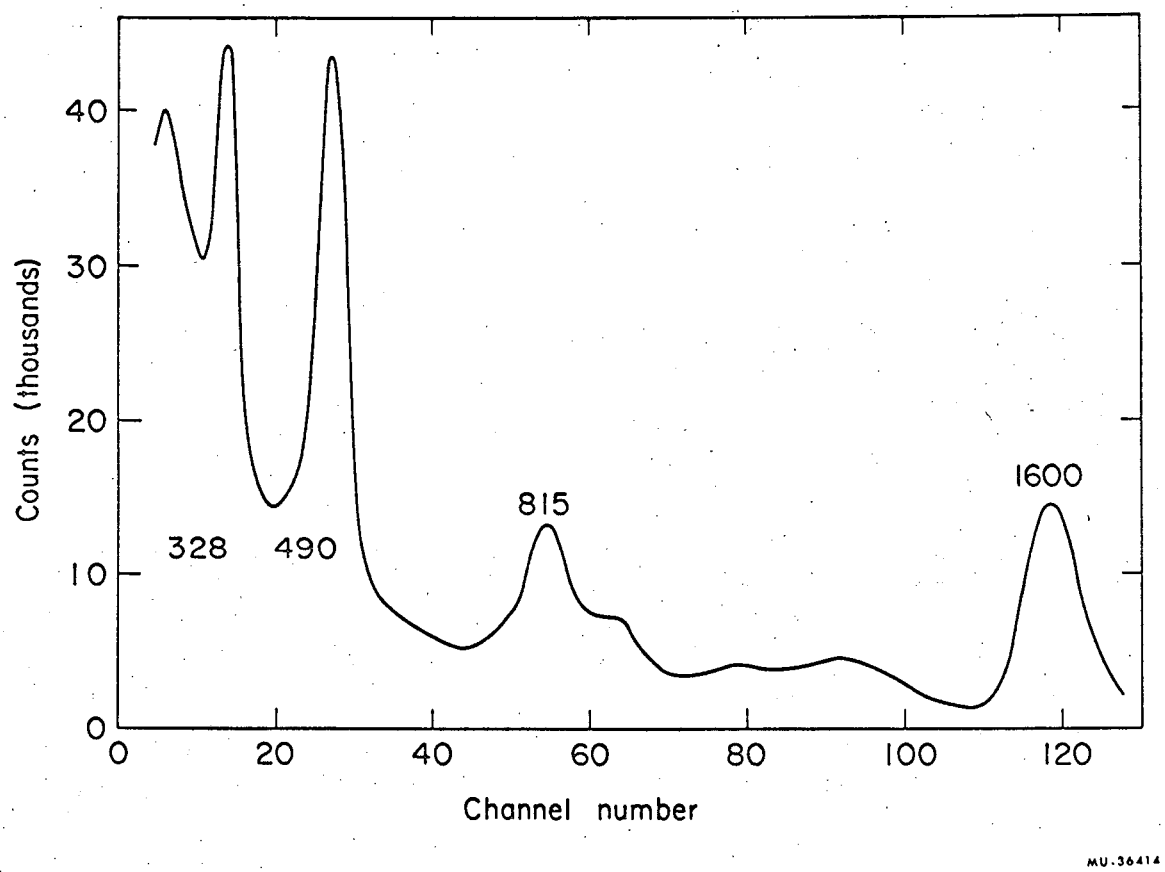

Fig. 19. Gamma-ray spectrum of La^{140} observed with a NaI(Tl) detector. Relevant energies are indicated in keV.

Table II. Gamma-ray anisotropies observed in the decay of La^{140} in CMN at 1/T = 500. The data are corrected for background, finite solid angle, and the short half life of the source.

gamma energy (keV)	$3/2\ B_2U_2F_2$
490	+0.0100(27)
815	-0.0180(26)
1597	+0.0194(10)

under the 490 and the 815-keV peaks is essentially isotropic. From Eq. (22) we thus calculate $G_2(B) = 0.67$ for the 490-keV peak and $G_2(B) = 0.64$ for the 815-keV peak. The 1597-keV peak and the background on which it rides have roughly equal anisotropies. From Eq. (23) we note that in this case the background factor is unity and independent of the peak-to-background ratio.

From the decay scheme we may infer that the 490 and the 1597-keV transitions are of pure E2 character while the 815-keV transition is mixed M1 and E2. From a comparison of the anisotropies we can arrive at the mixing ratio, δ, for the mixed transition. We can calculate B_2 from either the 490 or the 1597-keV transition and since the anisotropy of the 1597 keV has been measured more precisely we have used this gamma ray in the calculation. Since the details of the preceding decay are not well established we have estimated $U_2 = +0.8$ for all transitions. The actual values will probably be within about 15% of this estimate and the ratio of U_2 for different gamma rays will probably deviate even less. Using $F_2 = -0.598$ and $3/2\ B_2U_2F_2 = 0.0194(10)$ from Table II we calculate $B_2 = -0.0270(14)$ at $1/T = 500$. The error in U_2 has not been included. The F_2 value for the 815-keV transition then becomes $F_2^{815} = +0.56(8)$. The lower half of Fig. 20 shows the variation of F_2 with δ for this transition. The horizontal line is our measured F_2 and the dashed lines represent the error limits in our measurement. The uncertainty in U_2 has not been included in these errors. The regions in which the theoretical curve overlaps the experiment define acceptable values of the mixing ratio. To decide between the two ranges of δ we compared our results with those obtained from the angular correlation between the 815 and the 1597-keV transitions.[78] The corresponding curve is shown in the upper half of Fig. 20. Various authors have measured the 815-1597 correlation. A compilation of their results is shown in Table III.

It is important to note that in the angular correlation experiment, the 815-keV transition is the first member of the cascade where as in the nuclear alignment experiment the 815 keV is the last member of the cascade.

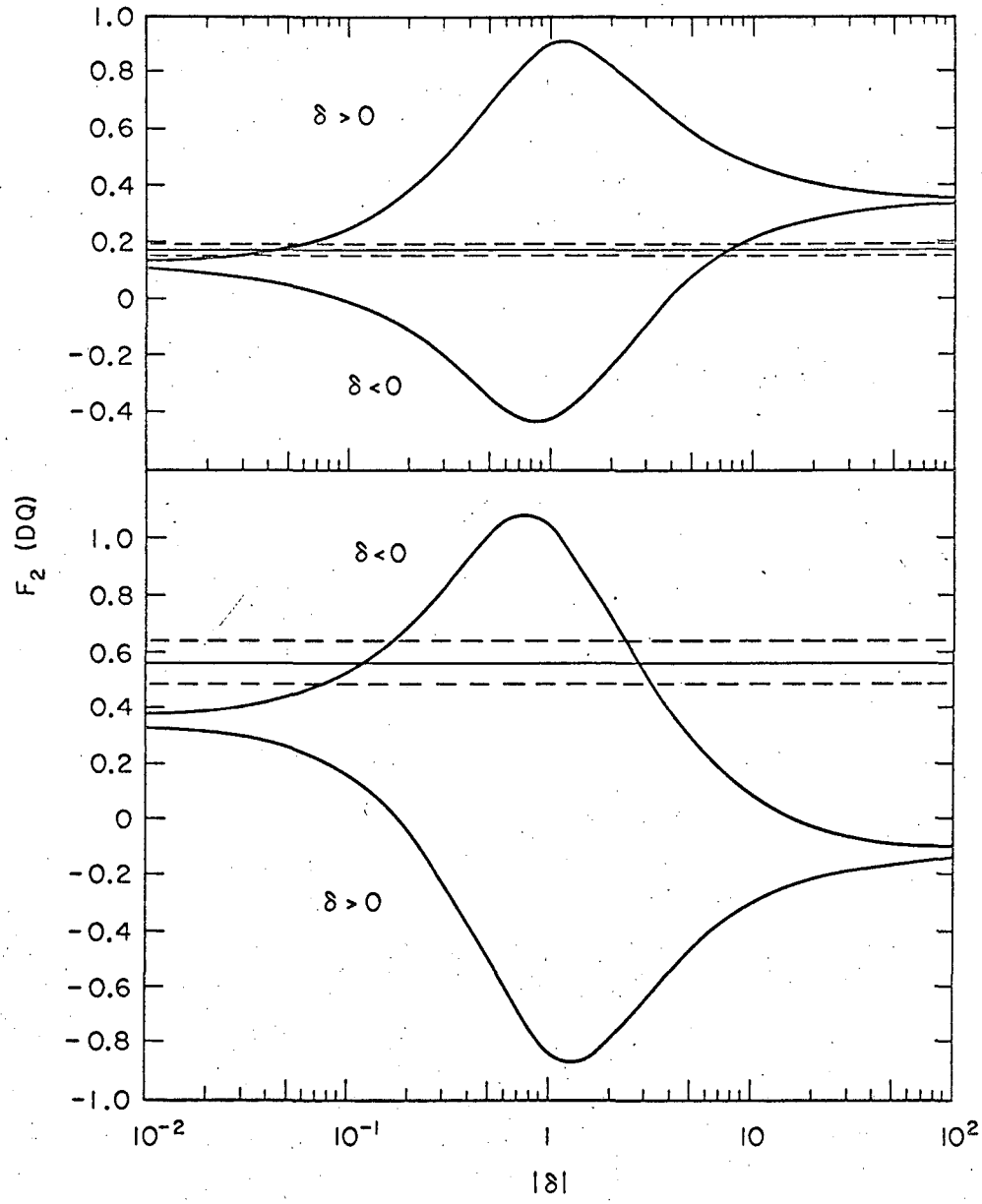

MU-36415

Fig. 20. Experimental F_2 and theoretical F_2 as a function of δ for angular correlation (upper figure) and nuclear alignment (lower figure) data for the 329-keV transition in Ce^{140}. The spin sequence for angular correlation is 3(DQ)4(Q)2 and for nuclear alignment the spin sequence is 3(DQ)4.

Table III. Mixing ratio for the 815-keV transition in Ce^{140} measured by angular correlation techniques.

Reference	F_2	Acceptable values of δ	Agreement with nuclear alignment?
78	+0.166(15)	Shown in Fig. 20	yes
83	+0.016(15)	-0.09 ; -4	no
84	-0.006(9)	-. 09 ; -4	no
85	+0.125(32)	$\|\delta\|<0.02$; -6	no
86	+0.186	+0.06 ; -9	yes

The two measurements are thus governed by different F_2 values and different δ values.[97] The difference in F_2 is reflected in the different shape of the curves in the upper and lower halves of Fig. 20. The two δ values differ in sign only so that agreement between the nuclear alignment experiment and the angular correlation experiment is obtained when δ agrees in magnitude but differs in sign. With these facts in mind we note that good agreement is obtained between the upper and lower portion of Fig. 20 for δ between 0.05 and 0.10. For the angular correlation data of Ref. 83, 84, and 85 shown in Table III there is no value of δ for which agreement is obtained with the nuclear alignment results. These angular correlation data must therefore be discarded on the basis of the nuclear alignment results.

Using Eq. (9) and our measured B_2 we calculate the quadrupole coupling constant $P = 0.110(16) \times 10^{-4}$ cm^{-1}. Edmonds found $P = 0.156 \times 10^{-4}$ for La^{139} in the double nitrate at room temperature.[3] This value must be corrected to $T = 0^{\circ}K$ as described above for the ethylsulfate experiment.[89] We obtain $P = 0.186 \times 10^{-4}$ cm^{-1}. Substituting into Eq. (26) with $Q_{139} = 0.27$ barns we find

$$Q_{140} = 0.27 \times \frac{0.110}{0.186} \times \frac{3 \times 5}{(7/2) \times 6}$$

$$= 0.114(17) \text{ barns}$$

in reasonably good agreement with the quadrupole moment derived above from the NES results. Averaging these two determinations gives $Q_{140} = 0.121(12)$ barns as the best value.

At the same time Edmonds' data gives $\gamma_N A_2^0 = -1.35(13) \times 10^4$ cm^{-1} a_0^{-2} where the sign is derived from the nuclear orientation data. This leads to a value of $\gamma_N/\gamma_E = +205(29)$.

2. Eu^{154}

In a manner analogous to the NES experiment we aligned Eu^{154} in CMN. Again we concentrated on the 1277-keV gamma ray since the largest anisotropy is to be expected here. The anisotropy was too small to obtain a temperature dependence curve, hence only the value at the lowest temperature, $1/T = 500$, was obtained. The measured anisotropy is $3/2\, B_2 U_2 F_2 = +0.019(1)$ from which we obtain $B_2 = -0.037(2)$, or $P = +.15(1) \times 10^{-4}\ cm^{-1}$. We can calculate the 4f contribution to P by comparison with the NES calculation, noting that

$$P_{4f}(CMN) = P_{4f}(NES)\frac{[\gamma_E A_2{}^0\langle r^2\rangle]_{CMN}}{[\gamma_E A_2{}^0\langle r^2\rangle]_{NES}} \tag{34}$$

where $\gamma_E A_2{}^0\langle r^2\rangle \equiv V_2{}^0$ is the crystal field gradient measured via optical spectroscopy. Using the measured values of $V_2{}^0$ from Figs. 3 and 17, $V_2{}^0(CMN) = -18.5$ and $V_2{}^0(NES) = +80$ we get for CMN:

$$P_{4f} = (0.85Q \times 10^{-4})\left(\frac{-18.5}{+80}\right) = -0.20Q \times 10^{-4}\ cm^{-1}.$$

The crystal field contribution can now be written as

$$P_{cf} = P - P_{4f}\ . \tag{35}$$

Using $Q = 3.08$ barns, as derived from the NES experiments, Eq. (35) becomes

$$P_{cf} = \left[\frac{+0.15}{3.08} - (-0.20)\right] Q \times 10^{-4} = 0.249Q \times 10^{-4}\ cm^{-1}.$$

From P_{cf} and Eq. (17a) we can calculate the antishielded field gradient at the nucleus in a straightforward manner, getting $\gamma_N A_2{}^0 = -0.348(85) \times 10^4\ cm^{-1}\ a_0{}^{-2}$. Since $\gamma_E A_2{}^0\ \langle r^2\rangle = -18.5\ cm^{-1}$ and $\langle r^2\rangle = 0.83\ a_0{}^2$, we find for the ratio of antishielding to shielding factors: $\gamma_N/\gamma_E = +176(47)$.

3. Gd^{159}

The gamma rays of the decay of Gd^{159} showed no observable anisotropy upon alignment in CMN. This result was not wholly unexpected since from Fig. 17 we see that the crystal field gradient in the double nitrates tends to zero at gadolinium. The statistical uncertainty of the measurements places an upper limit of $B_2U_2F_2 < .004$ on the anisotropy of the 362-keV gamma ray at $0.003^{\circ}K$. From this value we can derive an upper limit for the field gradient at the nucleus of $\gamma_N A_2^0 < 0.035 \times 10^4$ $cm^{-1}\ a_0^{-2}$.

Of course, we have assumed here that the Gd^{+3} ion grows substitutionally into the CMN lattice. Since the heavier rare earths do not form the double nitrate crystal, there is a possibility that the activity is merely incorporated in "brine holes" in the crystal interior rather than being an integral part of the lattice. In such a case the ions would not feel the crystal field and of course no anisotropy would be expected. The same reasoning may be applied to the Lu^{+3} work described below.

4. 7-day Lu^{177}

For Lu^{177} aligned in CMN, neither the 208-keV nor the 113-keV gamma ray showed any measurable anisotropy. An upper limit placed on the 208-keV anisotropy is $B_2U_2F_2 < 0.003$ at $0.003^{\circ}K$. This value leads to a field gradient at the nucleus of $\gamma_N A_2^0 < 0.012 \times 10^4\ cm^{-1}\ a_0^{-2}$. Still assuming that the ratio γ_N/γ_E varies rather slowly throughout the rare earths and provided that the Lu^{+3} grows into the lattice substitutionally this result implies that the crystal field gradient at the 4f site approaches zero for the heavier members of the rare earths in the double nitrate, as we proposed above.

F. Discussion

The antishielding factor, γ_N, has recently been calculated quite accurately for several rare earth ions. The work of various authors is compiled in Fig. 21. With the single exception of Ray's Pr^{+3} point there is good agreement among these values. In particular, the recent values by Freeman and Watson and of Sternheimer are probably quite reliable. On the basis of these points we find that γ_N is essentially constant at $\gamma_N = 75$ throughout the rare earths as indicated by the dashed line in Fig. 21.

In Table IV we have summarized the crystal field terms, $\gamma_N A_2^0$, derived from our experiments. We note that for the ethylsulfate these terms are roughly constant throughout the rare earths. Since the antishielding factor, γ_N, is also nearly constant, we find that the crystal field parameter, A_2^0, is constant for all rare earth impurities in neodymium ethylsulfate. This is not an unreasonable observation since A_2^0 originates with the crystal lattice which is NES in each case. For the double nitrate, however, $\gamma_N A_2^0$ is seen to vary apprecially from La^{+3} to Lu^{+3}. The term A_2^0 is thus a strong function of the impurity ion in this lattice. This datum correlates well with the fact that the heavier rare earths from the double nitrate crystal less and less readily, thus there must be considerable distortion of the lattice when these ions are grown as impurities into CMN. The crystal field set up at the impurity site thus arises from the distorted lattice so that one expects it to depend on the degree of distortion and hence on the nature of the impurity ion.

In Table IVa we give the ratio γ_N/γ_E for rare earths in the ethylsulfate. It is interesting to compare our work with that of other authors. We find fair agreement with $\gamma_N/\gamma_E = 250$ obtained by Barnes, et al., from the temperature dependence of the Mössbauer effect in thulium ethylsulfate.[53] Excellent agreement is obtained with Wickman who reports $\gamma_N/\gamma_E = 234$ from Mössbauer effect studies with dysprosium ethylsulfate.[90]

We note that γ_N may be calculated quite accurately using rather simple minded wave functions since the nucleus is far removed from the electrons responsible for the antishielding, primarily the 5s and 5p

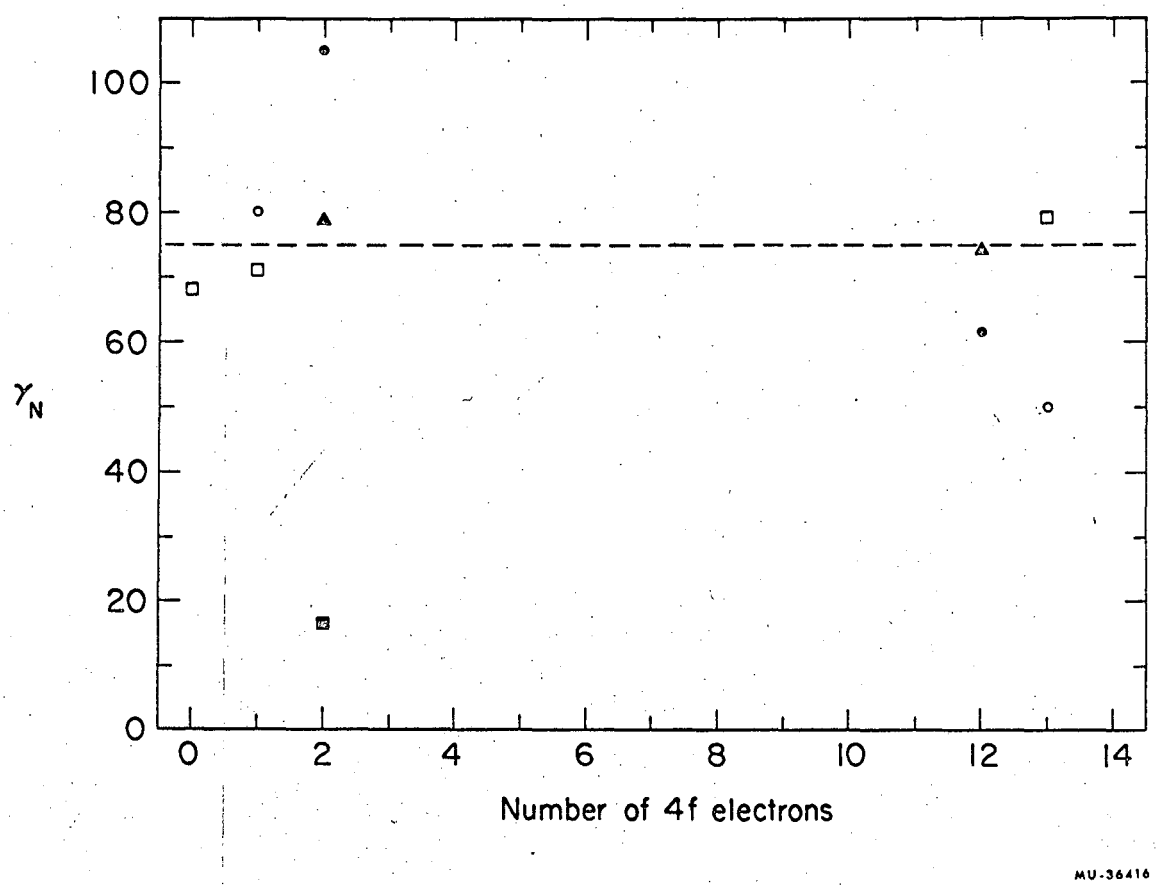

Fig. 21. Calculated antishielding factors for rare earth ions. Solid circles are from Ref. 25; open circles are estimated in Ref. 25 taking exchange effects into account. Triangles are from Ref. 58, open squares are from Ref. 59, and the solid square is from Ref. 55.

Table IV. The hyperfine structure constants, $\gamma_N A_2^0$, in (10^4 cm^{-1} a_0^{-2}).

Rare Earth ion	Double Nitrate	Ethylsulfate
La^{+3}	-1.35(13)	+1.43(15)
Eu^{+3}	-0.348(85)	-2.91(30)
Gd^{+3}	$\lvert\gamma_N A_2^0\rvert<0.035$	+2.35(24)
Lu^{+3}	$\lvert\gamma_N A_2^0\rvert$ 0.012	+3.32(11)

Table IVa. Shielding-antishielding ratios and electronic shielding factors for rare earth ions.

Ion	Lattice	γ_N/γ_E	γ_E
La^{+3}	DN[a]	+205(29)	+0.37(5)
Eu^{+3}	DN	+176(47)	+0.43(11)
La^{+3}	ES[b]	-623(63)	-0.12(1)
Eu^{+3}	ES	+300(40)	+0.25(3)
Gd^{+3}	ES	+217(22)	+0.35(4)
Lu^{+3}	ES	+150(10)	+0.50(3)

[a]DN means double nitrate lattice.

[b]ES means ethylsulfate lattice.

electrons. The factor γ_E, on the contrary, represents the shielding of the crystal field from the 4f electrons by the other electrons, primarily those of the 5s and 5p shells. The calculated value of γ_E thus depends very strongly on the electronic wave functions, and to date the theoretical predictions have only qualitative significance. Lenander and Wong[54] calculate $\gamma_E = 0.59$ for Pr^{+3} in the trichloride; Ray[55] calculates $\gamma_E = 0.48$ for the same ion and lattice; and Watson and Freeman[56] conclude that for Ce^{+3} the shielding factor, γ_E, is also appreciable. Burns[57] on the other hand, finds that γ_E should be no smaller than about 0.9 for rare earth ions. Sternheimer[87] has recently calculated $\gamma_E = +0.32$ for Pr^{+3} and $\gamma_E = +0.50$ for Tm^{+3}.

In Table IVa and in Fig. 22 we have calculated γ_E from our experimental values. It is evident that γ_E depends strongly on the nature of the ion. That this should be the case becomes apparent when we review the origin of this term. To define γ_E one first assumes that all ions in the lattice are localized point charges, completely neglecting electron overlap. The extent to which the crystalline electric field is shielded from the 4f electrons by the "outer electrons," mainly the 5s and 5p electrons, is defined as γ_E. In a real crystal, of course, there is appreciable overlap of the electron cloud of the ion with those of its neighbors. The "discrete point charge" picture of the lattice therefore becomes completely invalid, especially for the large ions such as La^{+3}. The 4f electrons still feel an electric field, however, and we can still define an empirical γ_E which relates the true field gradient to the A_2^0 calculated from our mathematical model. This γ_E will now be a strong function of the degree of electron overlap and the type of chemical bonding. It will thus depend strongly on the type of ion in question, as borne out by the experimental results of Table IVa. It is interesting that γ_E changes smoothly from a large positive value at Lu^{+3} to a negative value at La^{+3}. This indicates that the leading term of the field gradient changes sign in going through the rare earths.

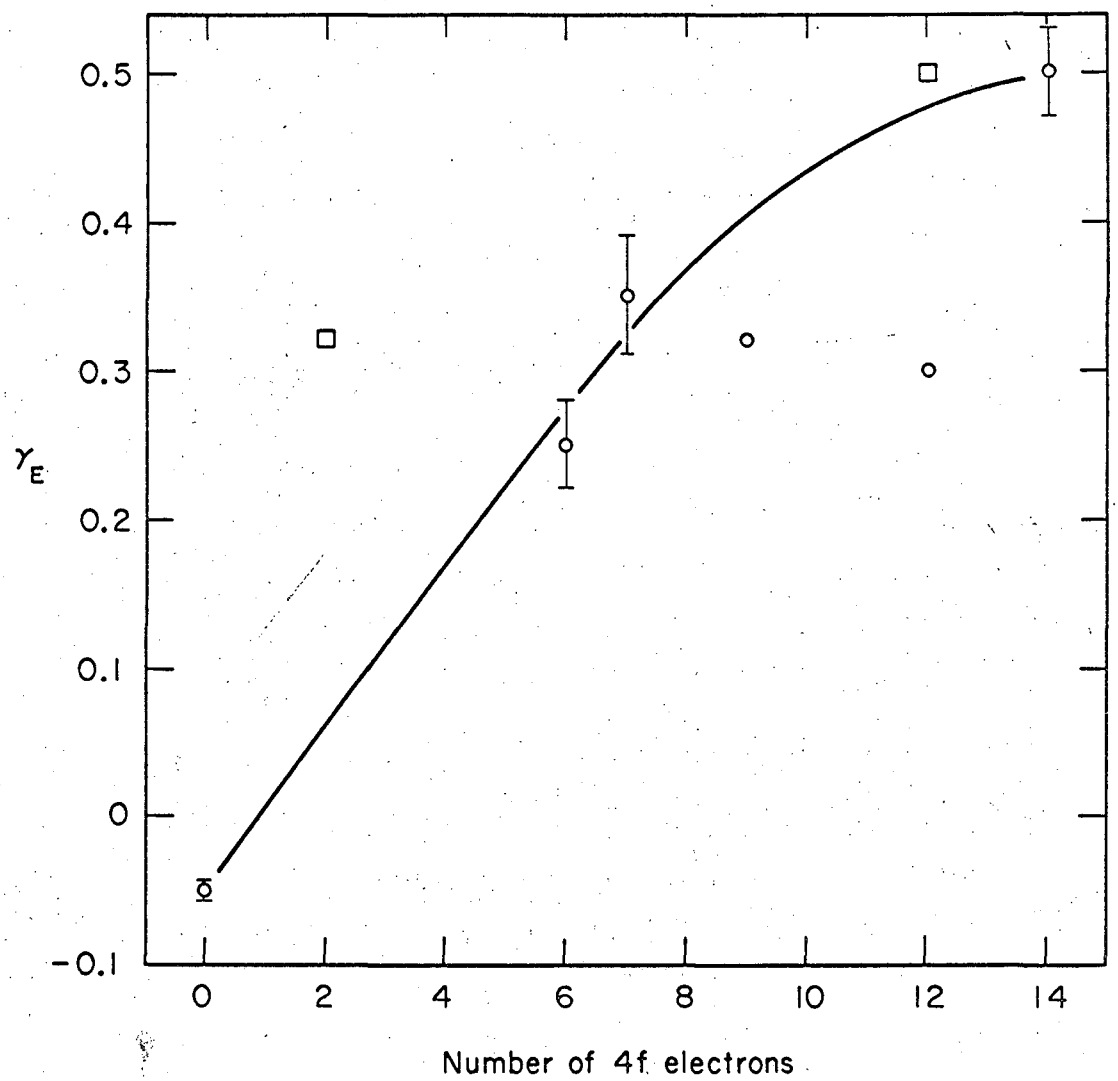

MU-36417

Fig. 22. The shielding factor γ_E for rare earths in the ethylsulfate. The circles for Tm^{+3} (n=12) and Dy^{+3} (n=9) are calculated from the γ_N/γ_E ratios given in Refs. 53 and 90 using the value γ_E=75. The squares for Pr^{+3} and Tm^{+3} have been calculated by Sternheimer.[87]

V. THERMODYNAMIC TEMPERATURE SCALE OF NEODYMIUM ETHYLSULFATE BELOW $1^{\circ}K$

A. Introduction

Neodymium ethylsulfate (NES), analogous to the other rare earth ethylsulfates, crystallizes readily from aqueous solution in hexagonal prisms with a trigonal axis of symmetry and having the chemical composition, $Nd(C_2H_5SO_4)_3 \cdot 9H_2O$. Its crystal structure, together with that of several other rare earth ethylsulfates, has been determined by Ketelaar.[30] The thermodynamic and magnetic properties of NES were extensively studied by Meyer[32] and this crystal has therefore long been a favorite host material for nuclear orientation experiments. The results obtained from the alignment of 7-day Lu^{177} in this lattice (see Sec. IV), as well as from similar experiments involving Ce^{137m} and Tb^{160}, have cast doubt upon the quantitative validity of Meyer's thermodynamic temperature scale.[33,34] In each case the experimental anisotropy would follow the theoretical expectations much better if a lower coldest temperature was assumed (Fig. 23). For this reason it was decided to redetermine the absolute temperature scale for NES at low temperatures.

B. The T-T* Relationship for NES

At temperature moderately lower than $1^{\circ}K$ the magnetic temperature, T^*, is a useful thermometric parameter. The extrapolation of Curie's law to low temperatures defines T^* in terms of the magnetic susceptibility, viz:

$$\chi = \frac{C}{T^*} \tag{36}$$

where C is the Curie constant. Since the susceptibility, χ, depends on the shape of the crystal as well as on its orientation in the measuring field, we must define these parameters carefully. The mechanical arrangement of the 20-kG iron core magnet and the mutual inductance coils is such that the demagnetizing field and the susceptibility-measuring field are

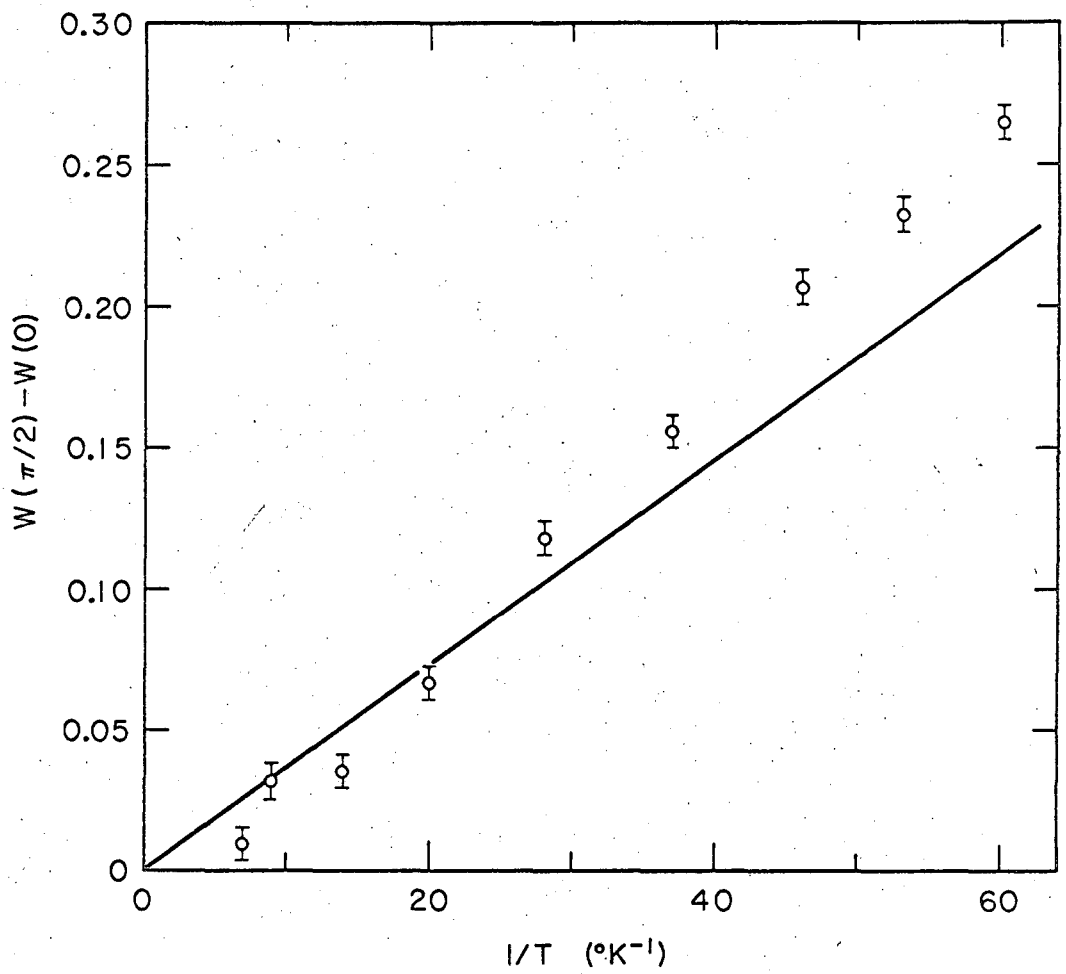

MU-36418

Fig. 23. 3/2 $B_2U_2F_2$ versus reciprocal temperature for the 208-keV gamma ray observed in the decay of 7-day Lu^{177} aligned in NES. The T-T* correlation of Ref. 32 was used in this figure. The solid line represents the behavior expected for pure quadrupole alignment.

at all times perpendicular to each other. Since we normally magnetize parallel to the crystalline c-axis to achieve maximum cooling from a given field, it follows that we measure the susceptibility perpendicular to the c-axis. The macroscopic shape of the crystal is also of considerable importance. We can write Curie's law as $I/H_\ell = C/T$, where I is the magnetic moment per unit volume and H_ℓ is the local field acting on the magnetic dipoles. Using the well-known Lorentz reasoning for calculating the magnetic interaction between the elementary dipoles, one finds that[15]

$$H_\ell = H_{ext} + (\frac{4\pi}{3} - N)I$$

where N is the demagnetization factor of the specimen, depending on its shape. The measured susceptibility, denoted by $\chi_m = I/H_{ext}$, is then written as

$$\chi_m = \frac{C}{T - (\frac{4\pi}{3} - N)C} . \tag{37}$$

For a spherical specimen, $N = 4\pi/3$ and thus

$$\chi_m = C/T; \tag{38}$$

that is, the local field felt by the elementary dipoles is equal to the external field and Curie's law should be strictly obeyed. For this reason one either uses a spherical sample or else corrects the experimental data to a spherical shape.

1. Description of the Method

After cooling the cryostat to the temperature of liquid helium, the relationship between the mutual inductance bridge units and the magnetic temperature is obtained in the usual way (see Sec. IV). A series of demagnetizations from a range of values of H/T gives the relationship between T^* and the entropy, S/R, since we can obtain S/R from H/T using the tabulated values of Hull and Hull.[64] The magnetic heat capacity, C^*, is then determined in the usual way,[65] using gamma radiation from Co^{60} as the heating source. From these data we can determine the absolute temperature since from the second law of thermodynamics:

$$TdS = dQ \tag{39}$$

or

$$T\frac{dS}{dT^*} = \frac{dQ}{dT^*} \equiv C^* \tag{40}$$

from which

$$T = \frac{C^*/R}{d(\frac{S}{R})/dT^*} . \tag{41}$$

Since C^* is only measured in arbitrary units in this experiment, the temperature obtained from Eq. (41) is only proportional to the absolute temperature. The proportionality factor is obtained by matching the measured temperature to T^* in the high temperature region, since here Curie's law is obeyed and $T = T^*$.

2. Experimental Procedure

As pointed out above, it is advantageous to perform susceptibility measurements of this type on a spherical single crystal. We found that with due care, we could make a sphere by growing the crystal slowly from saturated aqueous solution in a spherical bulb attached to the bottom of a standard 50-ml pyrex beaker. Growth of the crystal is started by placing a small seed crystal in the bottom of the bulb. It was necessary to change the growing solution frequently and to remove the small seeds which tended to form in the bulb and beaker. In this way a translucent single crystal of 24-mm diameter was grown in about six weeks. The crystalline c-axis could be readily located by examining the crystal when placed between crossed polaroids.

The crystal was supported by a glass holder and mounted in the cryostat in the usual way. Extra care was taken in winding and positioning the susceptibility measuring coils so that the crystal would be in a uniform field which was at all points accurately perpendicular to the crystalline c-axis. A computer calculation using the program "COILS"[66] showed that at all points containing the crystal, the radial component of the field set up by the coils was less than 1/2% of the axial field. The uniformity of the axial field was also within 1/2% throughout this region. The effect of the chrome alum and manganous ammonium sulfate guard salts was less than 1/2% in either coil, and since the effects of the sample coil and the dummy coil tend to cancel, the total effect of the guard salts was certainly negligible.

After filling the cryostat with liquid helium, calibrating the susceptibility coils to the He^4 temperature scale,[38] and pumping the bath down to $0.95^{\circ}K$, the relationship between entropy and magnetic temperature was obtained from a series of demagnatizations as described in Sec. V. C.

To obtain each point the magnetic field is applied for about 5 min with exchange gas in the cryostat to ensure thermal equilibrium with the helium bath. The field is then measured with a rotating-coil gaussmeter and the bath temperature is found from the vapor pressure

measured with a McLeod gauge. The exchange gas is then pumped out, the field turned off, and the magnet rolled away. Several T^* points are obtained over a period of several minutes as the crystal warms slightly due to stray heating. Extrapolation to zero time gives T^* at the instant of demagnetization. For the initial value of H/T we can obtain S_{ideal}/R for an ideal paramagnetic spin system using the tables of Hull and Hull.[64] For assorted values of spin quantum number S, these tables report S_{ideal}/R as a function of x, where $x = g\beta H/kT$. For NES, $S = 1/2$ and $g = 3.54$ since we magnetize parallel to the crystalline c-axis. Table V gives T^* and S_{ideal}/R for each demagnetization. The data are also plotted in Fig. 24. It is important to notice that we have taken into account only the spin entropy of the crystal. The total entropy is somewhat higher due to contributions of the lattice as well as dipole and hyperfine interactions. Meyer[32] has identified all contributions and has written the total entropy of the crystal as:

$$\frac{S}{R} = \frac{S_{ideal}}{R} + \frac{FT^3}{3} + D - \frac{G}{2T^2} + \phi\left(\frac{H}{T}\right) \tag{42}$$

where F, D, and G are constant. We see that all terms in Eq. (42), except S_{ideal}/R and $\phi(H/T)$, are independent of H. The term $\phi(H/T)$, which accounts for the additional magnetic field in the crystal created by the magnetic dipoles, has been calculated by Meyer and shown to be negligibly small for NES. Thus, since all demagnetizations were carried out from the same initial temperature, we observe that

$$\frac{dS}{dT^*} = \frac{dS_{ideal}}{dT^*} . \tag{43}$$

Thus Fig. 24 can be graphically differentiated to provide the denominator of Eq. (41).

Table V. Entropy and magnetic temperature for a spherical crystal of NES.

S_{ideal}/R	T*	S_{ideal}/R	T*
.0380	.0246	.4748	.0380
.0390	.0251	.5025	.0416
.0628	.0247	.5280	.0469
.0935	.0247	.5520	.0511
.1370	.0248	.5695	.0568
.1784	.0256	.5900	.0630
.2150	.0264	.6077	.0716
.2560	.0271	.6266	.0885
.2850	.0281	.6455	.1033
.3134	.0287	.6570	.1164
.3484	.0301	.6616	.1285
.3934	.0322	.6680	.1421
.4310	.0344	.6728	.1600

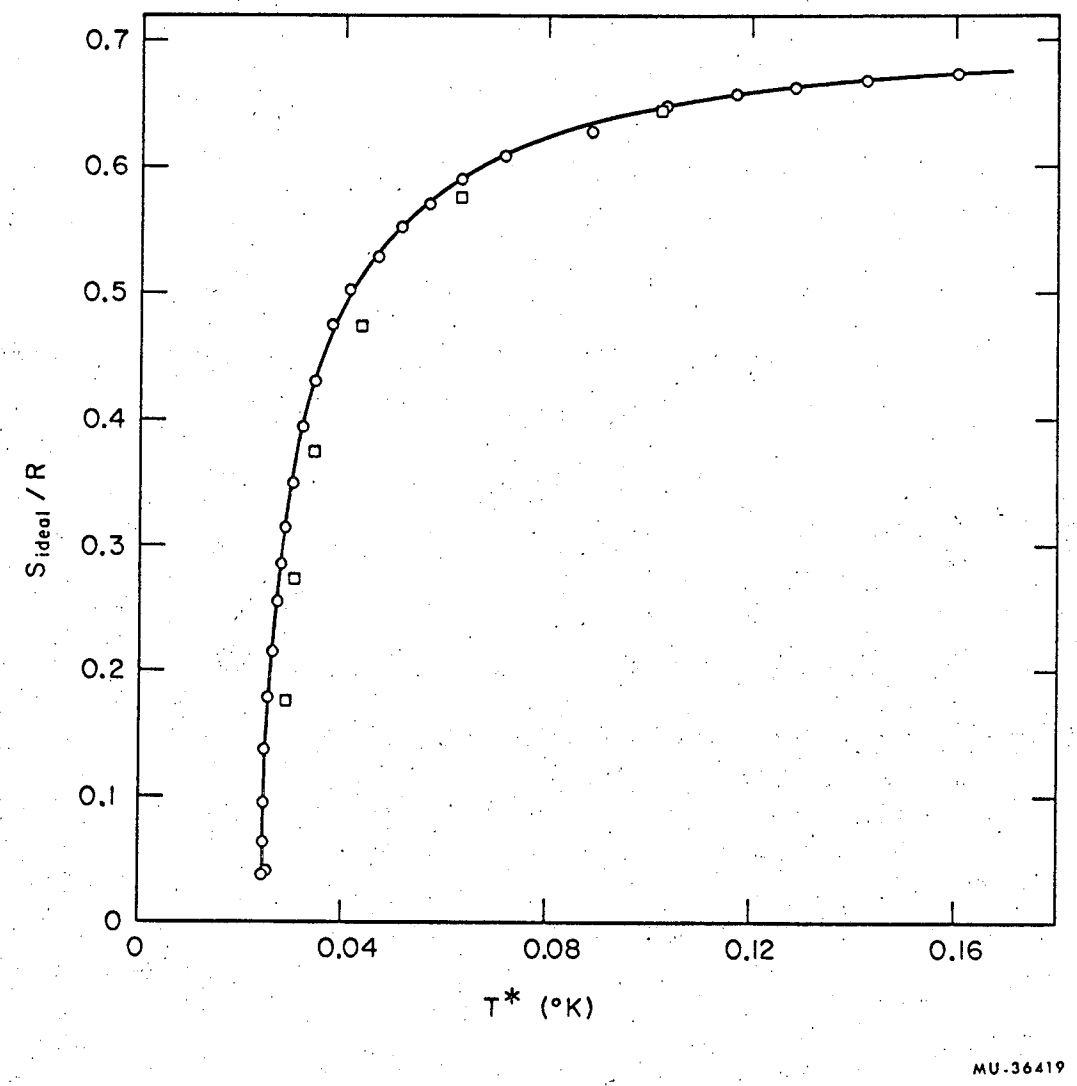

Fig. 24. Spin entropy as a function of magnetic temperature for a spherical crystal of NES. The circles were found in this work and the squares were obtained by H. Meyer.

The magnetic heat capacity, C^*, was obtained in the following manner. After demagnetization from a given initial H/T, a table containing two lead pigs with 100-millicurie Co^{60} sources inside was placed around the cryostat. The pigs were placed opposite each other with the movable lead doors facing the crystal. Since the table moved on the same tracks as the magnet, the accurate positioning of the sources for subsequent demagnetizations was an easy matter. When the sources were in place, with the doors closed, the magnetic temperature was measured for a few minutes. The lead doors were then opened for an accurately measured time interval (usually about 1 to 3 min), closed and the magnetic temperature followed again for a few minutes. The warming curves before and after heating were extrapolated to a time in the middle of the heating period, where the displacement of the curves represented ΔT^*. A typical warming curve is shown in Fig. 25. The time of heating represented ΔQ, and thus $C^* = \Delta Q/\Delta T^*$ gave the magnetic heat capacity in arbitrary units. The data obtained in this way are presented in Table VI. In Fig. 26 we have plotted C^* versus T^* on a logarithmic scale. The degree of nonlinearity of this curve tests the deviation from ideal behavior since for an ideal spin system CT^2 is constant.

The quantity derived from dividing C^* by $d(S/R)/dT^*$ which we can call T' is only <u>proportional</u> to the absolute temperature since C^* is measured only in arbitrary units. To derive the proportionality factor we plotted T'/T^* as a function of T^* in Fig. 27. Since at high temperatures T and T^* are identical, we find the proportionality factor from

$$\lim_{T^* \to \infty} \left(\frac{T'}{T^*}\right) = \frac{T'}{T} . \tag{44}$$

From smoothed values of $d(S/R)/dT^*$ and C^* we obtained the T-T^* relationship shown in Table VII and in Fig. 28. Both the slope of the S/R versus T^* curve and the value of C^* become very uncertain at temperatures below about $1/T^* = 35$ as may be seen from Figs. 24

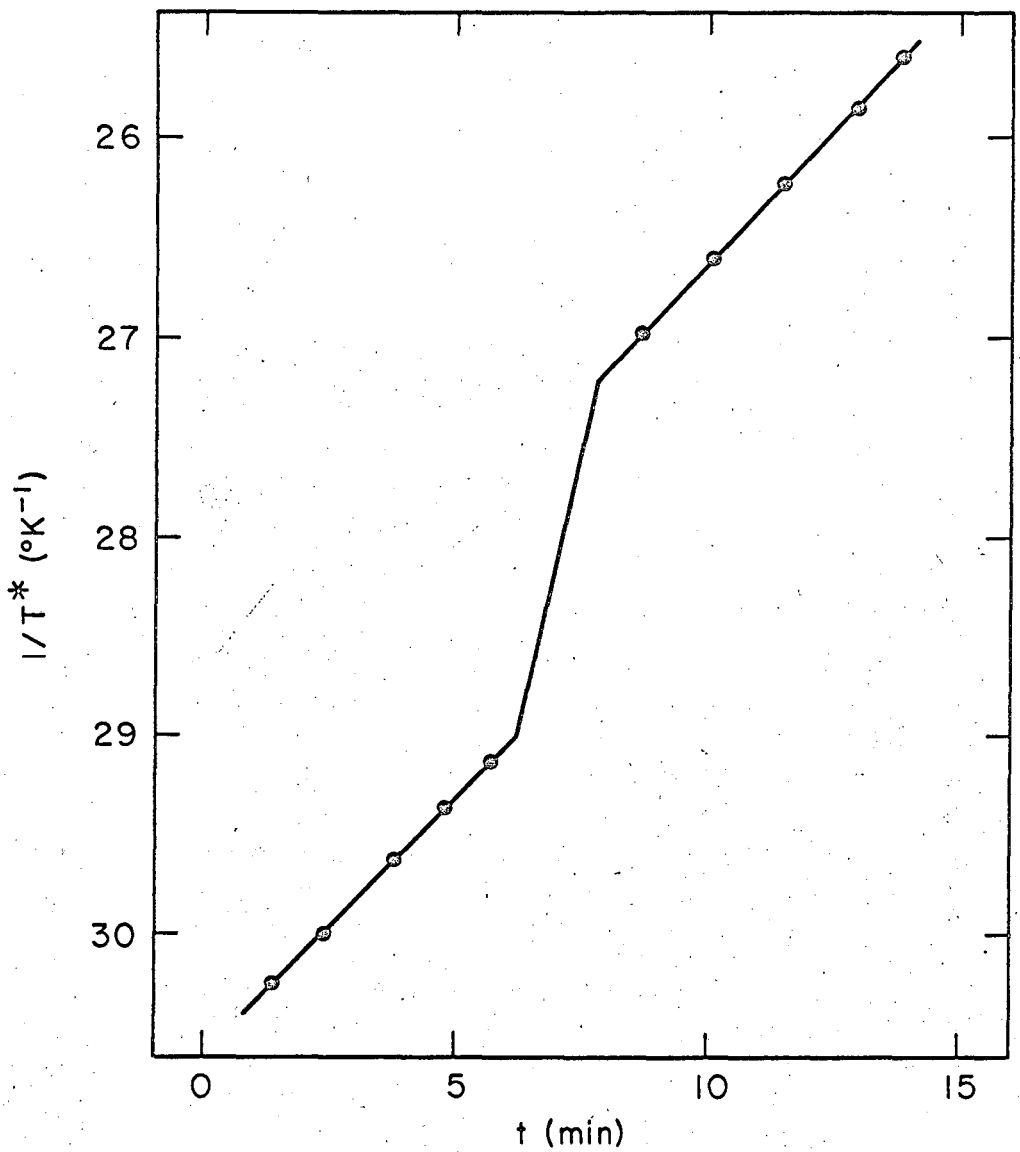

MU-36420

Fig. 25. Typical warming curve for NES heated with Co^{60} gamma rays. The steep part of the curve corresponds to the heating period.

Table VI. Magnetic heat capacity and magnetic temperature for a spherical crystal of NES.

C*	T*	C*	T*
.5852	.0246	.1084	.0320
.4318	.0242	.1043	.0331
.4024	.0254	.0880	.0356
.3770	.0237	.0835	.0369
.3024	.0257	.0732	.0398
.2998	.0238	.0707	.0416
.2575	.0258	.0625	.0452
.2505	.0256	.0574	.0467
.2424	.0245	.0554	.0499
.2060	.0241	.0546	.0507
.1938	.0252	.0511	.0517
.1916	.0259	.0465	.0574
.1908	.0257	.0422	.0660
.1860	.0256	.0356	.0743
.1833	.0270	.0358	.0753
.1632	.0283	.0364	.0755
.1545	.0265	.0310	.0842
.1384	.0280	.0334	.0903
.1304	.0296	.0298	.0915
.1285	.0295	.0250	.0947
.1200	.0308		

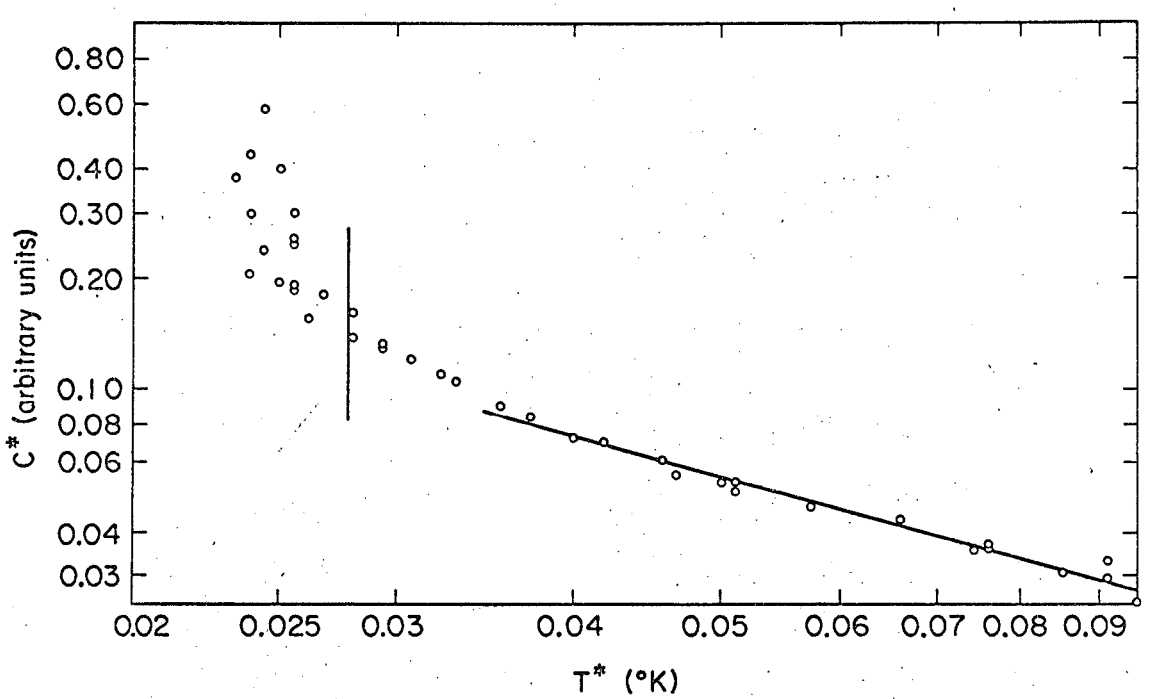

MU-36422

Fig. 26. Magnetic heat capacity as a function of magnetic temperature for a spherical crystal of NES. Only data at temperatures above the vertical line are considered reliable.

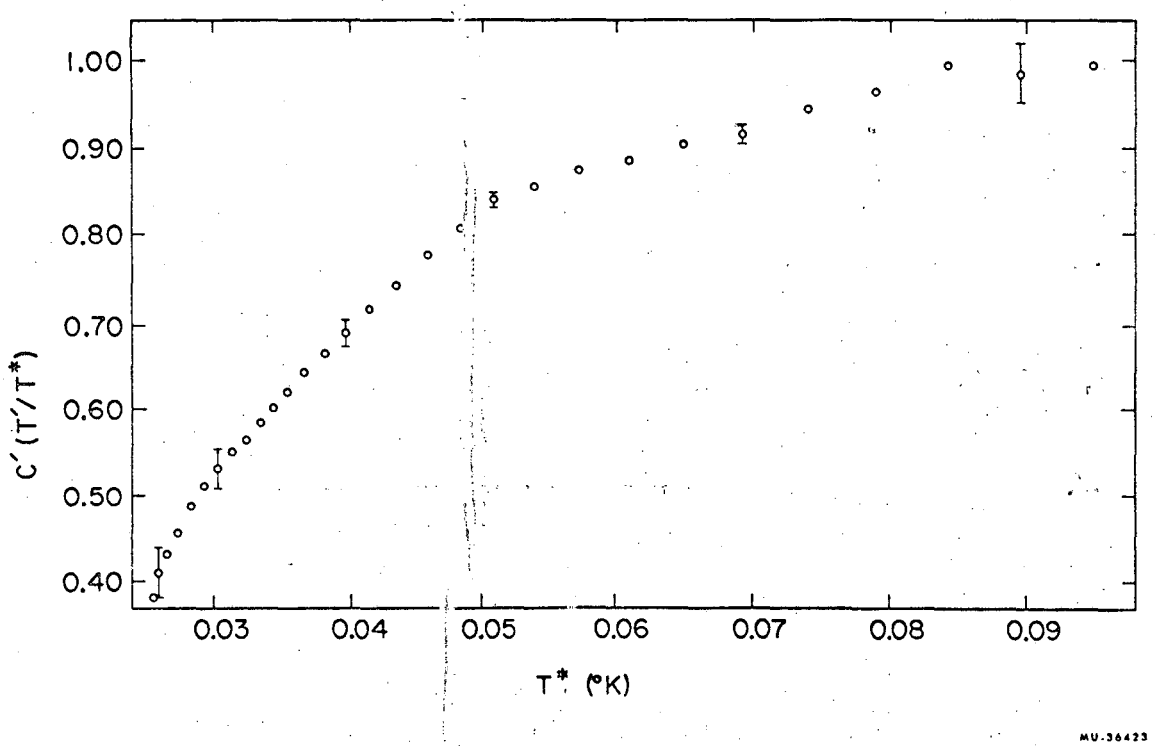

Fig. 27. The ratio T'/T* versus T* for a spherical crystal of NES. The normalizing constant C' equals 3.08.

Table VII. Relationship between the magnetic and thermodynamic temperature for NES.

1/T*	1/T	1/T*	1/T
10.50	10.4	23.00	30.5
11.13	11.4	24.10	33.3
11.87	11.8	25.15	36.1
12.65	13.0	26.15	38.9
13.51	14.1	27.2	42.0
14.43	15.6	28.2	45.0
15.38	16.8	29.0	47.5
16.39	18.3	29.8	50.5
17.47	19.7	30.8	53.6
18.52	21.4	31.8	56.9
19.60	23.1	32.8	60.8
20.70	25.2	33.9	65.4
21.85	27.8	35.1	71.2

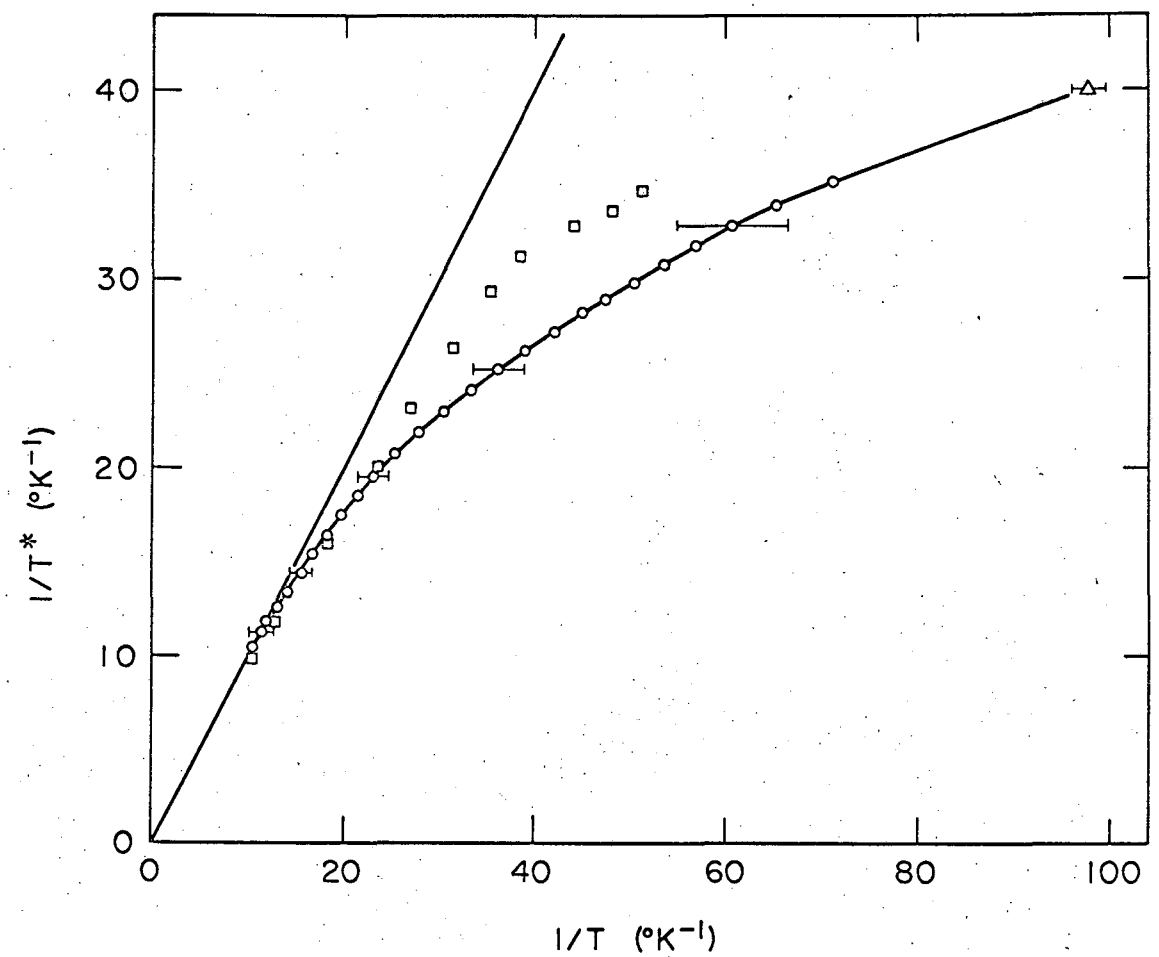

MU-36424

Fig. 28. Relationship between magnetic and thermodynamic temperature for NES. Meyer's data (squares) are shown for comparison with our determination using gamma-ray heating (circles) and using the gamma-ray anisotropy of Ce^{137m} (triangle). The curve would follow the straight line if Curie's law were strictly obeyed.

and 26. Thus the curve of Fig. 28 is derived from Eq. (43) only for $1/T^* < 35$. The extremely-low temperature portion of the curve was derived from gamma-ray anisotropy measurements of Ce^{137m} to be described below. H. Meyer's data is also shown in Fig. 28 for comparison. A large part of the discrepancy can be traced to the S/R versus T* measurement shown in Fig. 24. We note that at the lowest temperatures our T* is rather lower than that of Meyer. Since in this region the slope, dS/dT^*, is varying very rapidly, large errors in T can arise from rather small errors in T*. We believe that our measurement of T* is more precise than that of Meyer since we used a spherical crystal for which no demagnetization correction had to be calculated.

C. The Thermodynamic Temperature Scale of NES at Extremely Low Temperatures

We note from Figs. 24 and 26 that dS/dT^* and C* both approach infinity for values of $1/T^*$ above about 35. Beyond this point T* is thus no longer a useful thermometric parameter and Eq. (41) can no longer be used to find the absolute temperature. At these low temperatures the thermodynamic temperature scale was therefore determined from the gamma-ray anisotropy of the 255-keV isomeric transition in Ce^{137m}.

The nuclear alignment of Ce^{137m} in NES has been discussed by Frankel, et al.[81] The decay scheme is rather complex but for our purposes only the intense 255-keV isomeric transition is of importance. This is an M4 transition from the $11/2^-$ metastable state to the $3/2^+$ ground state of Ce^{137}. This gamma ray shows an anisotropy in excess of 80% and is still increasing at the lowest temperatures obtained, thus it provides a very sensitive measure of temperature. The alignment of tripositive Ce^{137m} in NES is described by the following Spin Hamiltonian:[81]

$$\mathcal{H} = AS_zI_z + B(S_xI_x + S_yI_y) \qquad (45)$$

with $A = 0.074\ \mu_N/I\ cm^{-1}$; $B = 0.002\ \mu_N/I\ cm^{-1}$; and $I = 11/2$. From this Spin Hamiltonian the theoretical temperature dependence of the anisotropy can be calculated as a function of the nuclear magnetic moment, μ_N. In Fig. 29 we have fit the theoretical curve to Frankel's experimental anisotropies for $1/T < 25$. In this range the T-T* relationship is very well-known; in fact Horst Meyer's curve here even agrees with ours as shown in Fig. 28. In Fig. 29 we have used our T-T* curve throughout and we note that the experimental points follow the theoretical curve very well even for $1/T > 25$. No such agreement is obtained when using the T-T* data of Horst Meyer, as pointed out by Frankel, et al. The magnetic moment derived from Fig. 29 is also in good agreement with that found from a similar experiment in CMN, whereas there was sharp disagreement when Horst Meyer's temperature scale was used.[67]

Ce^{137m} was prepared from natural La_2O_3 by the reaction La^{139} (p,3n) Ce^{137m} using 30 MeV protons in the Berkeley 88-inch cyclotron. The Ce activity was separated from the La_2O_3 by solvent extraction of Ce^{+4},[33] and the resulting tripositive Ce^{137m} was grown into a single crystal of NES. The crystal was mounted in the demagnetization cryostat in the usual way. Several 15 sec counts were taken with NaI(Tl) detectors at 0° and at 90° to the crystal axis. The anisotropy was calculated from

$$\epsilon = 1 - \frac{W(0^\circ)}{W(90^\circ)} \tag{46}$$

for each run and extrapolated to the instant of demagnetization. The temperature reached on demagnetization could then be read from Fig. 29. The experiment is summarized in Table VIII.

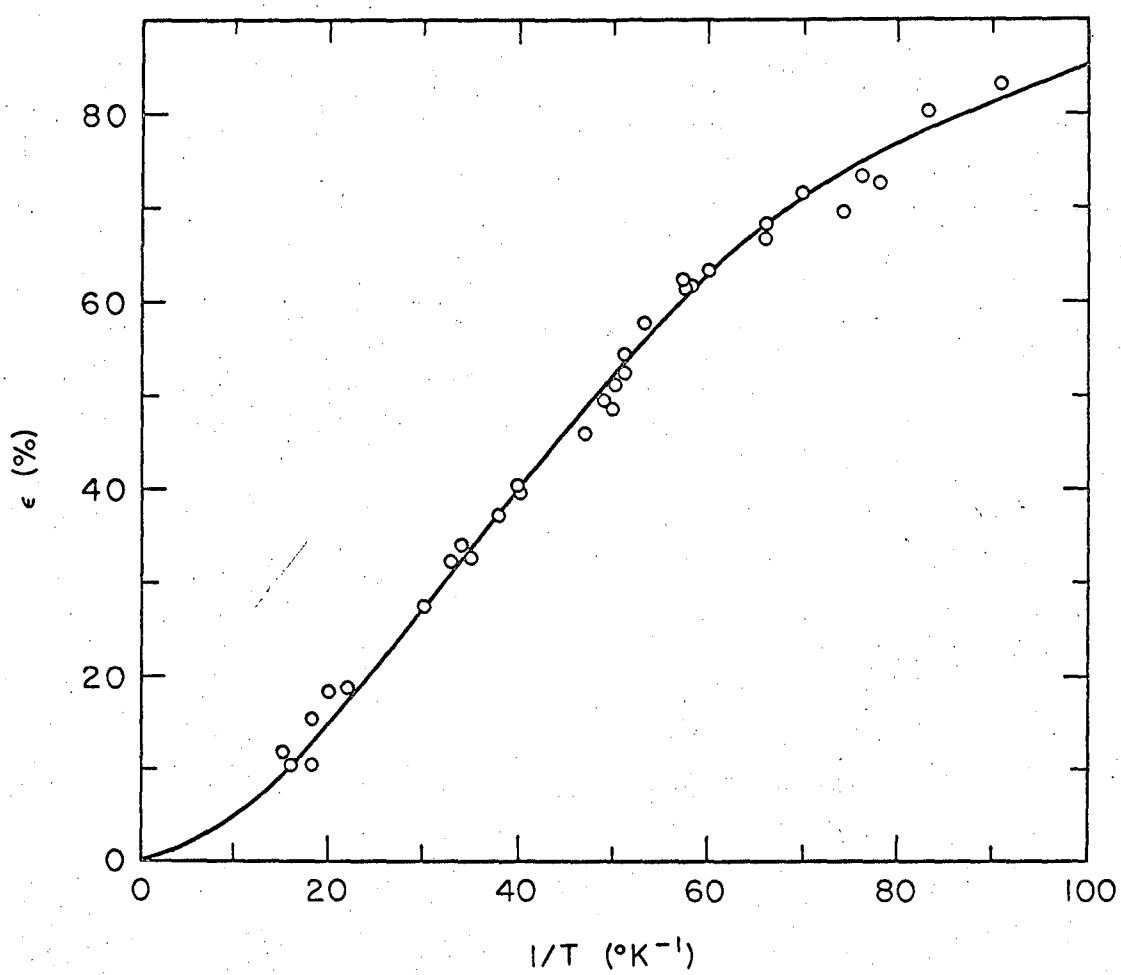

MU-36425

Fig. 29. Anisotropy versus temperature for the 255-keV gamma ray of Ce^{137m}. The temperatures were calculated from Fig. 27.

Table VIII. Summary of nuclear alignment of Ce^{137m} in NES.

Run	$G_2(\Omega)$	$G_2(B)$	W(0)	$W(\pi/2)$	$\epsilon\%$	$1/T(^{o}K^{-1})$	$H/T(G/^{o}K)$
1	1.05	1.05	.243	1.462	83.4	97	19800
2	1.05	1.05	.241	1.482	83.8	98	19800
3	1.05	1.05	.242	1.484	83.7	98	19800
4	1.06	1.05	.255	1.409	81.9	94	15600
5	1.06	1.05	.237	1.470	83.9	98	18300
6	1.06	1.05	.423	1.317	67.9	66	9650
7	1.06	1.05	.298	1.409	78.9	86	13200
8	1.06	1.05	.634	1.199	47.1	46	7300
9	1.06	1.05	.282	1.418	80.1	89	14000
10	1.06	1.05	.349	1.363	74.4	76	11600
11	1.23	1.05	.294	1.441	79.6	88	13650
12	1.23	1.05	.394	1.331	70.4	69.5	10400

D. Discussion

In Table IX and in Fig. 30 we show the relationship between H/T and the temperature reached upon demagnetization. It is satisfying to note that the results obtained from the T-T* experiment agree very well with the results obtained from the Ce^{137m} anisotropy experiment. The results of Horst Meyer are also shown in Fig. 30 and the very poor agreement is evident. We note that our lowest temperature corresponds to 1/T = 98(2). We have placed this point on Fig. 28 to complete the curve of T versus T*. We have checked the validity of the new temperature scale with several independent experiments. The good agreement between the nuclear magnetic moments of Ce^{137m} calculated from the NES experiment and from the CMN experiment has already been pointed out. The Lu^{177} nuclear alignment data are shown in Fig. 12 in terms of the new temperature scale. Comparison with Fig. 23 shows that the linearity of the data is greatly improved with the new temperature scale. We can therefore conclude that the present temperature scale is a decided improvement over that which was previously available.

Table IX. The relationship between magnetizing field and temperature reached on demagnetization for NES.

From T-T* measurement		From Ce^{137m} gamma-ray anisotropy	
H/T (gauss/°K)	1/T	H/T (gauss/°K)	1/T
1690	6	7300	46
1890	7	9650	66
2140	8	10400	70
2300	9	11600	76
2670	10	13200	86
3190	12	13650	88
3640	15	14000	89
4050	17	15600	94
4480	20	18300	98
4840	23	19800	98
5310	27		
5800	34		
6320	39		
7140	48		
7850	54		
8740	62		
9480	69		

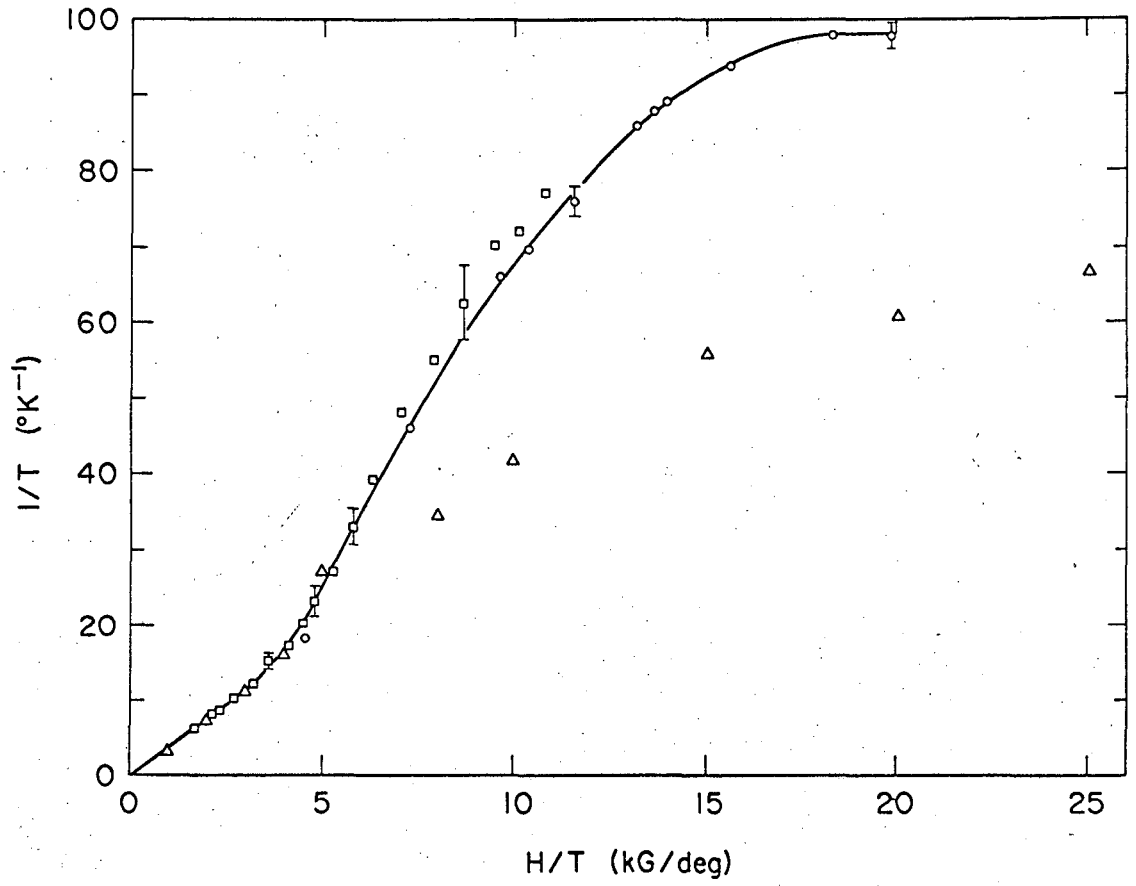

MU-36426

Fig. 30. Final temperature reached upon demagnetization of NES from H/T. Squares are determined from gamma-ray heating and circles from the gamma-ray anisotropy of Ce^{137m}. Horst Meyer's data (triangles) are shown for comparison.

VI. 155-DAY Lu^{177}

A. Introduction

Quite thorough studies have been made of the decay scheme of 155-day Lu^{177m}.[10,11] This isomer has an unusually high spin which can be accounted for only by postulating a three quasiparticle state of an uncoupled neutron pair added to the odd proton of Lu^{177}. In particular, we see from a study of the intrinsic nuclear level diagram[68] that the configuration obtained by coupling the $[624]9/2^+$ neutron, the $[514]7/2^-$ neutron, and the $[404]7/2^+$ proton to a state of spin $23/2^-$ is most likely to explain the observed Lu^{177} isomer. The isomer decays partly by isomeric transition to high-lying levels of the $K= 7/2^+[404]$ rotational band of Lu^{177} and partly by β^- decay to corresponding three quasiparticle states in Hf^{177}, which then further decay to high-lying members of the $K = 7/2^-[514]$ and $K = 9/2^+[624]$ rotational bands. The decay scheme is shown in Fig. 13.

This decay is particularly important from a theoretical point of view; its many levels in clearly defined rotational bands providing an excellent test of nuclear structure theory. It was thus worthwhile to confirm the proposed level scheme independently by definitive coincidence measurements and high sensitivity gamma-ray spectroscopy using the newly developed lithium-drifted germanium [Ge(Li)] gamma-ray detectors.

Since their introduction at Chalk River, Ontario,[69] the staff of the Lawrence Radiation Laboratory has perfected the manufacture of Ge(Li) detectors and their associated electronics[14] so that 3-mm thick detectors with excellent resolution are routinely available.

B. The Decay Scheme

The decay scheme of Lu^{177m} was carefully examined with Ge(Li) detectors with the aim of filling in the missing 19/2 level in the $K = 7/2^-[514]$ rotational band and verifying the remainder of the proposed decay scheme. Further, we measured with improved precision and accuracy the energies and relative intensities of many of the gamma rays observed in the decay. These data make Lu^{177m} one of the few energy and efficiency standards suitable for use with the high resolution Ge(Li) detectors.

1. Source Preparation

Lu^{177} was prepared by irradiating a sample of natural lutetium metal in a neutron flux of 5×10^{14} for one 41-day cycle of the ETR reactor at Arco, Idaho. The very intense 7-day isomer was allowed to decay for several months, whereupon the remaining material was dissolved to separate it from the remaining activities of all other elements by means of an ion exchange procedure. The solution was adsorbed on a column of Dowex 50W-X8 (100-200 mesh size) cation exchange resin and eluted with a solution of α-hydroxy isobuteric acid. The central portion of the eluted lutetium fraction was free of all activity other than that attributed to Lu^{177m}. After removing the activity from the organic material, it was redissolved in water and evaporated onto aluminum counting plates. Some activity was also incorporated into a NES crystal for nuclear orientation studies.

2. Coincidence Experiments

In Fig. 31 we show a gamma-ray spectrum of Lu^{177m} obtained with a Ge(Li) detector. The detector had a sensitive area measuring about 1 cm by 2 cm and a depth of about 3 mm. The spectrum shown was obtained in about two days with a source of less than one millicurie placed about 10 cm from the detector surface. In general the position of the peaks tended to agree with the spectrum obtained with a bent-crystal spectrometer at Caltech.[11] A careful look at the 400-keV region, however, shows a definite peak at 426 keV (see Fig. 32) which fits energetically as the transition from the missing 19/2 level to the 15/2 level in the $K = 7/2^-[514]$ rotational band. To establish that this gamma ray actually was the 19/2 to 15/2 transition, we used two Ge(Li) detectors with the coincidence circuitry of the amplifiers to obtain the spectrum in coincidence with this peak. This experiment was performed only with considerable difficulty. The very low counting rate of the 426-keV peak made it extremely difficult to set the coincidence gate accurately, so an appreciable portion of the gate pulses were due to the background of the 418-keV transition. Furthermore, since the gate counting rate was so low, the coincidence rate was so extremely low that the true-to-chance ratio could not be made very high. These difficulties are reflected in the coincidence spectra of Fig. 33. About five days were required for each of the spectra of Fig. 33. Although the total number of coincidences is rather small, there are still sufficient counts to determine that the 426-keV peak is definitely in coincidence with the 113, 136, 249, and 341-keV peaks, and definitely not in coincidence with the other prominent peaks of the spectrum. This is exactly as expected from the decay scheme and so the location of the $I = 19/2$ level, as well as the 426-keV transition is definitely confirmed to be in the position shown in Fig. 13. The remainder of the decay scheme was further confirmed through similar coincidence measurements with the 105, 413, and 418-keV transitions. Since these gamma rays are much more intense, the coincidence spectra could be obtained with much less difficulty. The results, in agreement with the decay scheme, are tabulated in Table X.

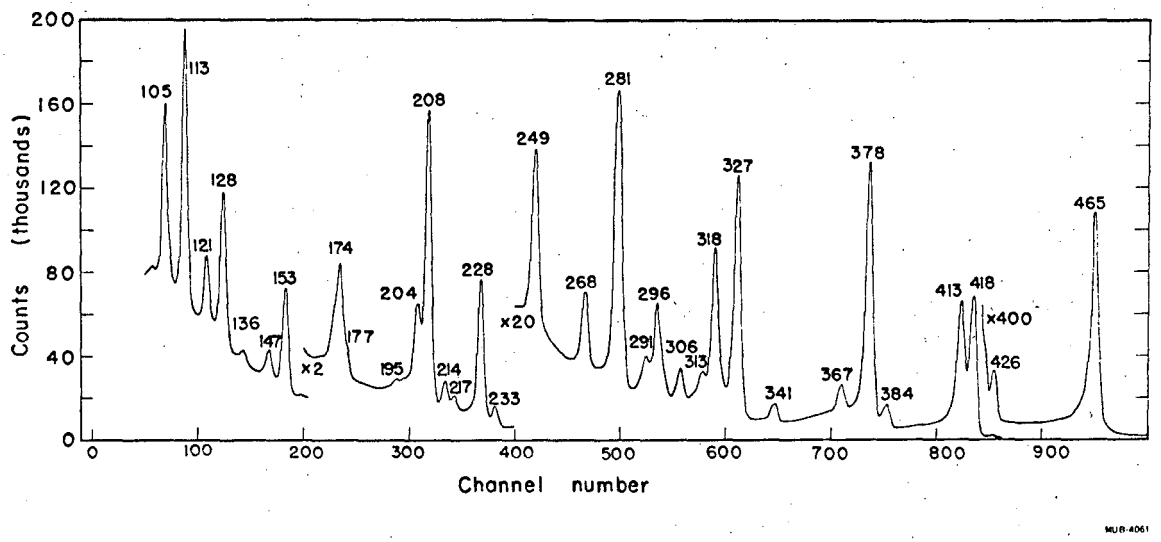

Fig. 31. Gamma-ray spectrum of Lu^{177m} obtained with a Ge(Li) detector. The peaks are identified by their energies in KeV.

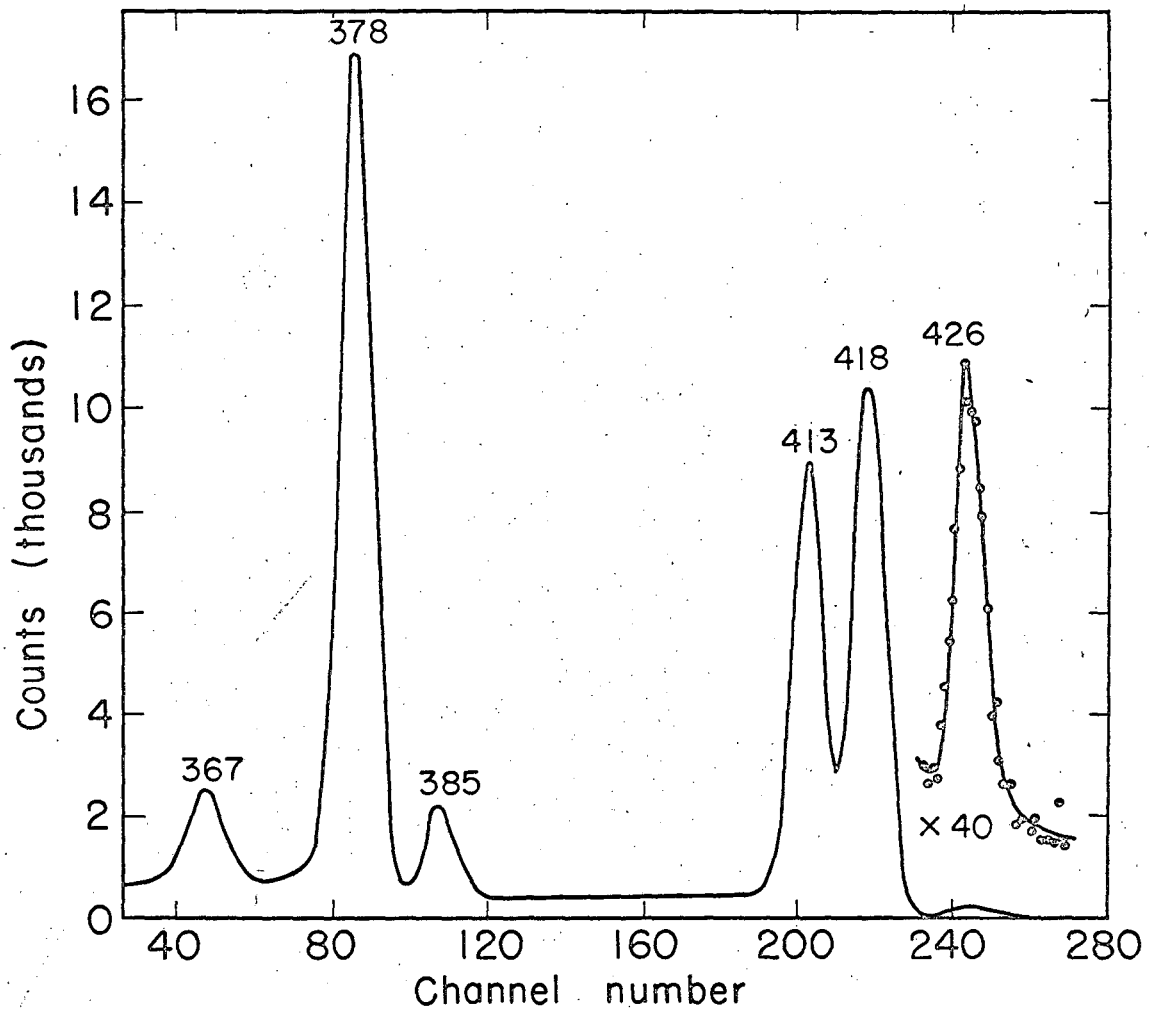

MUB-4333

Fig. 32. Detail of the Lu^{177m} spectrum showing the 426-keV transition. The filled circles designate experimental points.

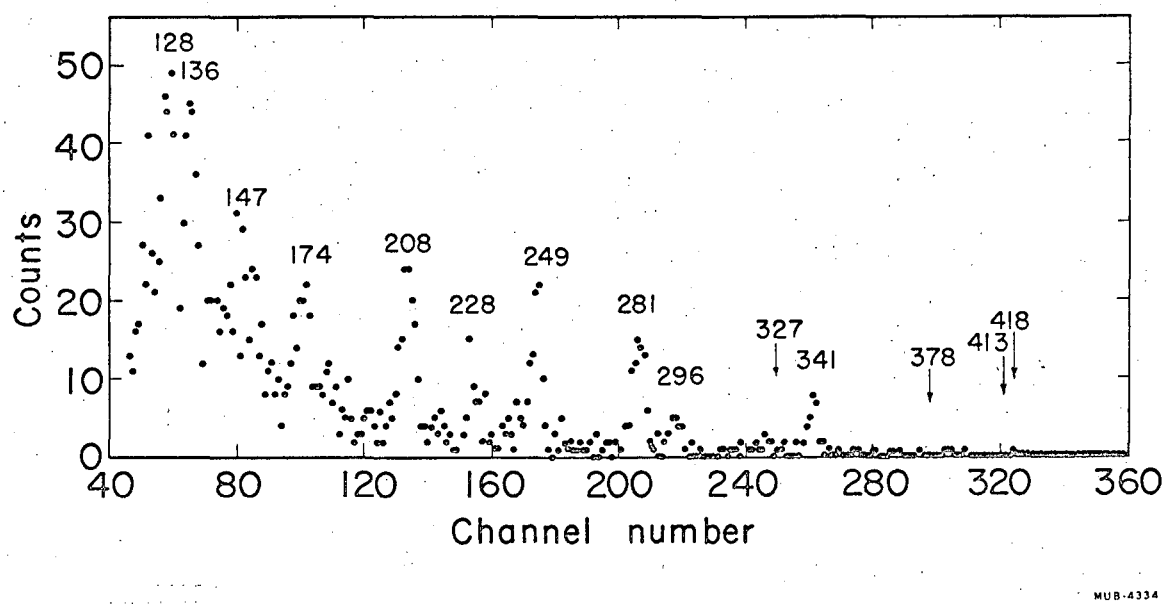

Fig. 33. Gamma-ray spectrum of Lu^{177m} in coincidence with the 426-keV transition. Coincidence with the 136, 249, and 341-keV transitions is clearly indicated. A separate run determined the coincidence between the 426 and the 113-keV transitions.

Table X. Coincidence measurements on Lu^{177m} gamma rays. Gamma rays in the coincident spectrum are identified by their energies in keV. Those gamma rays which are neither listed "in coincidence" nor "not in coincidence" were too weak to determine.

Gate = 105 keV		Gate = 413 keV		Gate = 418 keV	
in coincidence	not in coincidence	in coincidence	not in coincidence	in coincidence	not in coincidence
153	171	147	228	105	121
174	268	171	378	113	136
208	291	174	413	128	147
228	296	177	418	153	204
249	318	318		174	228
281	367	268		208	318
327	384			233	387
378	413			249	413
418				281	418
				296	
				327	

3. Gamma-Ray Energies and Relative Intensities

Comparison of the Ge(Li) spectrum of Fig. 31 with the bent-crystal data[11] points to the superiority of Ge(Li) in three important respects. First we note that, although not as good at low energies, the resolution of the Ge(Li) counter excells that of the bent-crystal spectrometer for energies above about 300 keV. Secondly, the efficiency of Ge(Li) is far higher; and finally, the signal-to-noise ratio is very high for Ge(Li) counters since there is little background due to incoherent scattering. Thus we could improve on the energies of the high energy peaks of the spectrum and also get more accurate relative intensities for the entire spectrum.

The energy calibration was performed using as energy standards the low energy Lu^{177} gamma-ray energies obtained with the bent-crystal spectrometer and the 511-keV positron annihilation radiation from Na^{22}. The energies obtained are given in column 1 of Table XI. Those energies above 318 keV were obtained in this experiment; the others are taken directly from Ref. 11 and included in Table XI for convenience.

The relative intensities of the gamma rays were obtained by fitting the peaks with Gaussian curves after subtracting the background for each channel. An alternate procedure consisted of simply summing the counts under the entire peak, again subtracting off the appropriate background. Consistent results were obtained with both techniques. The area under the Gaussian is proportional to the product of the height and the full width at half maximum (FWHM) of the curve. The error in the measurement is thus determined by the accuracy with which these quantities can be determined. The display of a peak on a multichannel analyzer is, of course, not a true Gaussian but only a histogram which approximates a Gaussian when a sufficiently large number of channels are available. Thus the FWHM measurement is subject to considerable error when the photopeak is displayed in only a few channels; as it must be for Lu^{177m} where a large energy range must be displayed in at most 1000 channels. In fact a large fraction of the uncertainty in our relative intensity measurements arises from this source.

The intensities thus obtained were corrected for the energy dependence of the counter efficiency using an empirical energy-efficiency calibration obtained from the gamma-ray spectrum of Hf^{180m}. The features of this decay pertaining to this work are summarized in the appendix. The relative intensities obtained for the Lu^{177m} gamma rays are given in column 2 of Table XI.

C. Nuclear Orientation of Lu^{177m}

1. Alignment in NES

We have aligned the long-lived isomer of Lu^{177} in NES, using Ge(Li) detectors to measure the anisotropy of many of the gamma rays in the spectrum. In Table XII we show the anisotropies obtained by counting with one Ge(Li) detector at 0° to the crystalline c-axis. For the gamma rays below about 200 keV quite large background corrections were applied to the data since these gamma rays ride on a high Compton background. Correction factors were typically $G_2(B) = 0.5$ to $G_2(B) = 0.25$. Beta-gamma coincidence measurements have shown that the three-quasiparticle states in Hf^{177} have lifetimes $\tau_{1/2} > 10^{-2}$ sec. In fact, a technique involving rapid chemical separation from Lu^{177m} has shown a half life for the Hf daughter of $\tau_{1/2} = 1.06(5)$ sec.[70] One therefore expects any off-diagonal matrix elements of the orientation Hamiltonian to produce reorientation of these intermediate states, leading to a strongly attenuated anisotropy for the succeeding gamma rays.[71] Comparing the anisotropies of corresponding gamma rays from Lu^{177} and Hf^{177} rotational bands, particularly the 318-327 doublet and the 413-418 doublet, we find no evidence for any attenuation. This implies a purely diagonal Hamiltonian for the Hf^{+4} ion. This is not surprising since Hf^{+4} is isoelectronic with Lu^{+3}, the nuclei thus seeing essentially the same type of surroundings.

Table XI. Energies and relative intensities of gamma rays observed in the decay of Lu^{177m}. Figures in parentheses indicate the error in the last figure.

gamma energy (keV)	relative intensity this work	relative intensity Ref. 11	rotational band location
106.36(2)	100*	100*	9/2+
112.97(2)	174(14)	251(13)	7/2-
121.56(3)	58(5)	62(3)	7/2+
128.48(2)	131(11)	125(6)	9/2+
136.68(2)	18(2)	17(3)	7/2-
145.59(6)	38(4)	11(2)	9/2+ → 7/2-
147.10(6)		27(3)	7/2+
153.25(4)	134(12)	134(7)	9/2+
159.92(8)	7(1)	5(1)	7/2-
171.84(8)	41(4)	41(4)	7/2+
174.37(6)	105(9)	110(6)	9/2+
177.05(8)	25(3)	34(3)	9/2+ → 7/2-
195.4(1)	19(2)	9(2)	7/2+
204.00(8)	137(12)	130(13)	9/2+
208.36(6)	510(43)	610(31)	9/2+ → 7/2-
214.3(1)	64(61)	79(8)	9/2+
218.0(1)	30(3)	37(6)	7/2+
228.48(8)	314(26)	340(17)	9/2+ → 7/2-
233.8(1)	40(4)	43(4)	9/2+
249.7(1)	56(5)	62(6)	7/2-
268.4(1)	30(3)	32(5)	7/2+
281.8(1)	133(12)	121(6)	9/2+
291.7(3)	21(2)	20(4)	9/2+ → 7/2-
296.1(2)	58(6)	65(7)	7/2-
299.1(3)	13(2)	10(2)	9/2+ → 7/2-

*Normalized to 100.

Table XI. Continued.

gamma energy (keV)	relative intensity this work	relative intensity Ref. 11	rotational band location
306.0(3)	23(2)	13(3)	9/2+ → 7/2-
313.5(3)	19(2)	12(2)	9/2+ → 7/2-
318.8(2)	104(9)	86(4)	7/2+
327.4(2)	168(15)	141(15)	9/2+
341.5(3)	16(2)	14(4)	7/2-
367.3(3)	31(3)	25(5)	7/2+
378.2(2)	286(25)	223(22)	9/2+
384.8(3)	32(3)	37(7)	7/2-
413.6(2)	192(18)	163(16)	7/2+
418.2(2)	234(22)	185(19)	9/2+
426.2(5)	6.8(9)	———	7/2-
465.0(5)	26(2)	23(7)	7/2-

Table XII. Gamma-ray anisotropies for Lu^{177m} in NES. The average temperature of the measurements was 1/T = 90. The error in the last figure is indicated in parentheses.

Hf^{177} gamma rays			Lu^{177} gamma rays		
Gamma energy (keV)	$B_2U_2F_2$ uncorrected	$B_2U_2F_2$ Background corrected	Gamma energy (keV)	$B_2U_2F_2$ uncorrected	$B_2U_2F_2$ Background corrected
105.4	+.091(5)	+.372(28)	121.6	-.055(6)	-.239(36)
113.0	+.016(5)	+.048(20)	268.4	-.175(20)	-.175(20)
128.5	+.154(6)	+.462(24)	318.8	-.197(18)	-.197(18)
153.3	+.210(6)	+.478(18)	413.6	-.230(21)	-.230(21)
174.4	+.121(7)	+.274(20)			
208.4	-.090(5)	-.090(5)			
228.5	-.220(8)	-.220(8)			
249.7	-.138(11)	-.138(11)			
281.8	-.216(11)	-.216(11)			
296.1	-.138(43)	-.138(43)			
327.4	-.210(16)	-.210(16)			
378.2	-.303(13)	-.303(13)			
418.2	-.223(18)	-.223(18)			
465.0	-.216(64)	-.216(64)			

From the anisotropy of the 413-keV gamma ray we have calculated the ratio of the nuclear quadrupole moments of Lu^{177m} and of the 7-day ground state, Lu^{177g}. In Sec. IV. D. 4 we obtained $P = -6.1(2)\times10^{-4}\,cm^{-1}$ for Lu^{177g}. For the 413-keV gamma ray of Lu^{177m} we have $B_2U_2F_2 = -0.230(21)$ at $1/T = 90$. We calculate $F_2 = -0.378$ for the $17/2^+ \rightarrow 13/2^+$, E2 transition and $U_2 = +0.937$ for the preceding $23/2^- \rightarrow 17/2^+$, E3 transition. From these data and Eq. (9) we find $P = -1.18(11) \times 10^{-4}\,cm^{-1}$. We then obtain

$$\frac{Q^m}{Q^g} = \frac{[P(I(2I-1))]_m}{[P(I(2I-1))]_g} \tag{47}$$

$$= \frac{-1.18}{-6.1} \times \frac{\frac{23}{2} \times 22}{\frac{7}{2} \times 6} = 2.33(25).$$

Using $Q_0{}^g = 7.8$ estimated from Townes,[45] and Eq. (30) we find $Q^g = 3.6$. On this basis the quadrupole moment of the 23/2 level becomes

$$Q^m = 2.33 \times 3.6 = 8.4(10) \text{ barns}$$

from which

$$Q_0{}^m = 10.8(13) \text{ barns.}$$

The error in the ground state quadrupole moment is not reflected in these figures. A comparison of the anisotropies of the $I \rightarrow I-2$ and $I \rightarrow I-1$ transitions originating from the same state will yield the M1-E2 mixing ratio, δ, for the $I \rightarrow I-1$ transition. For the pure E2 crossover transition we can calculate F_2 exactly. Since B_2 and U_2 are the same for both the crossover and cascade transitions, we note that the ratio of the F_2's equals the ratio of the anisotropies. We can thus calculate F_2 for the mixed transition and hence from

$$F_2 = \frac{F_2(M1) + 2\delta F_2(M1,E2) + \delta^2 F_2(E2)}{1 + \delta^2}$$

we obtain δ. From Eq. (33) we can then calculate both the magnitude and sign of $(g_K - g_R)$.

Although in principle one can calculate δ and $(g_K - g_R)$ for each pair of transitions in each of the three rotational bands populated in the decay of Lu^{177m}, in fact a glance at the spectrum shows that only the 153-281 pair and the 174-327 pair have both members sufficiently well resolved to measure the anisotropy with any degree of reliability. For the 153 keV, $15/2 \rightarrow 13/2$ gamma ray we find

$$F_2(153) = \frac{+.478}{-.216} F_2(281) = \frac{+.478}{-.216} (-.3856) = +.853(54).$$

In Fig. 34 we show the ranges of δ satisfied by this value of F_2. Since the transition is expected to be largely M1 from a comparison with the analogous state in Hf^{179},[49] only the smaller value of δ has physical significance. We thus obtain $\delta = -0.39(4)$. From Eq. (33) we calculate $(g_K - g_R)/Q_0 = -0.049(5)$. Using $Q_0 = 6.85$ obtained from Ref. 47 for the analogous state in Hf^{179} we find $(g_K - g_R) = -0.335(34)$. Taking $g_R = +0.203(34)$ from Ref. 49 for the similar state in Hf^{179} we find $g_K = -0.13(5)$. The theoretical value based on the Nilsson model is $g_K = -.35$. Theory and experiment can be brought into agreement if we choose an effective spin g-factor which is 50% of the free-neutron value of $g_S = -3.826$.

For the 174 keV, $17/2 \rightarrow 15/2$ transition we obtain in analogous fashion

$$F_2(174) = \frac{+.274}{-.210} \times F_2(327) = \frac{+.274}{-.210}(-.3776) = +0.493(52).$$

Fig. 35 shows the ranges of δ satisfied by this value of F_2. Again using only the smaller value of δ we have $\delta = -0.13(3)$ from which

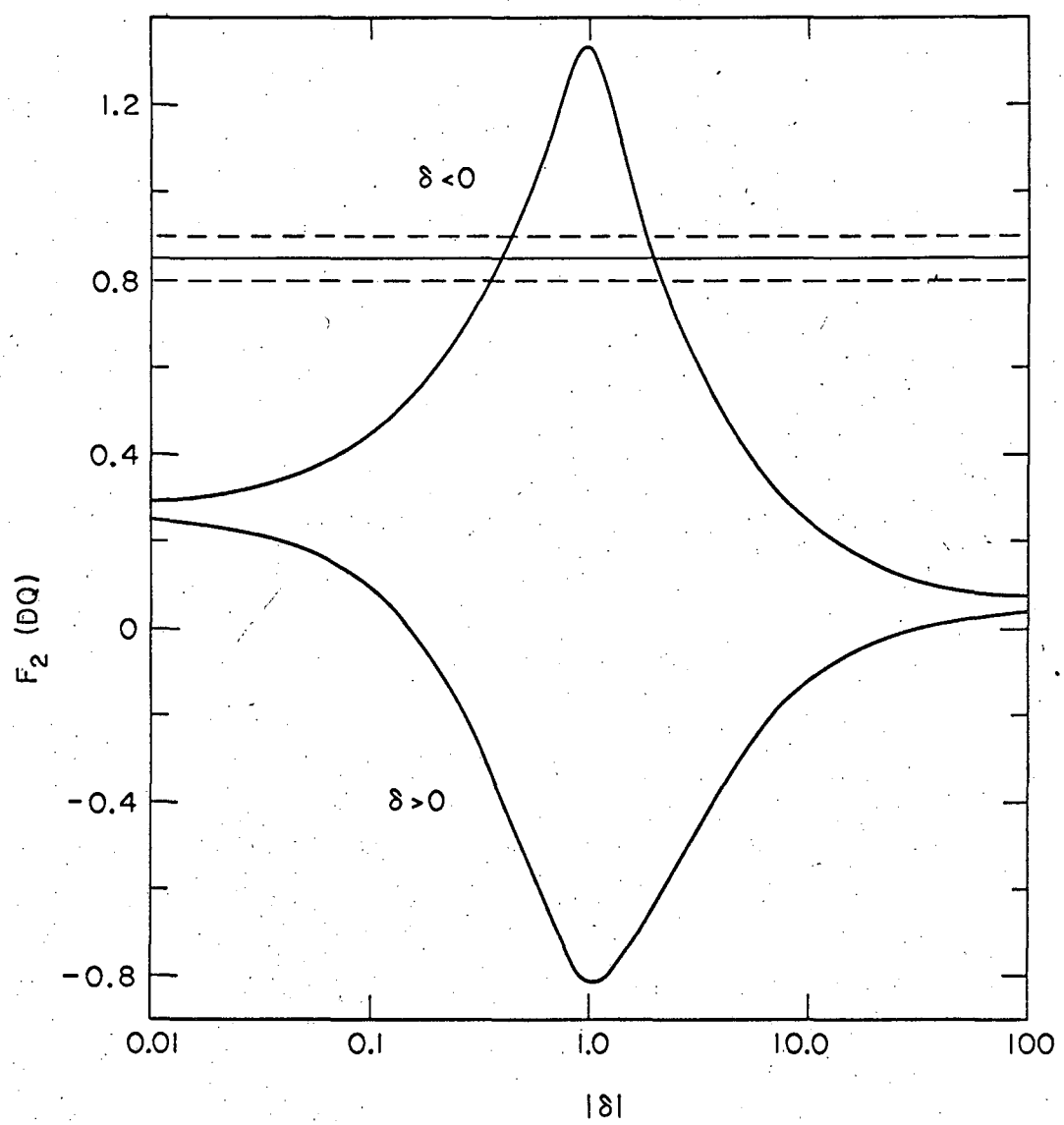

MU-36427

Fig. 34. Experimental F_2 and theoretical F_2 as a function of δ for the 153-keV transition in Hf^{177}. The maximum and minimum of the F_2 curve have been drawn incorrectly in this figure. The fit with the experimental F_2 is unchanged, however.

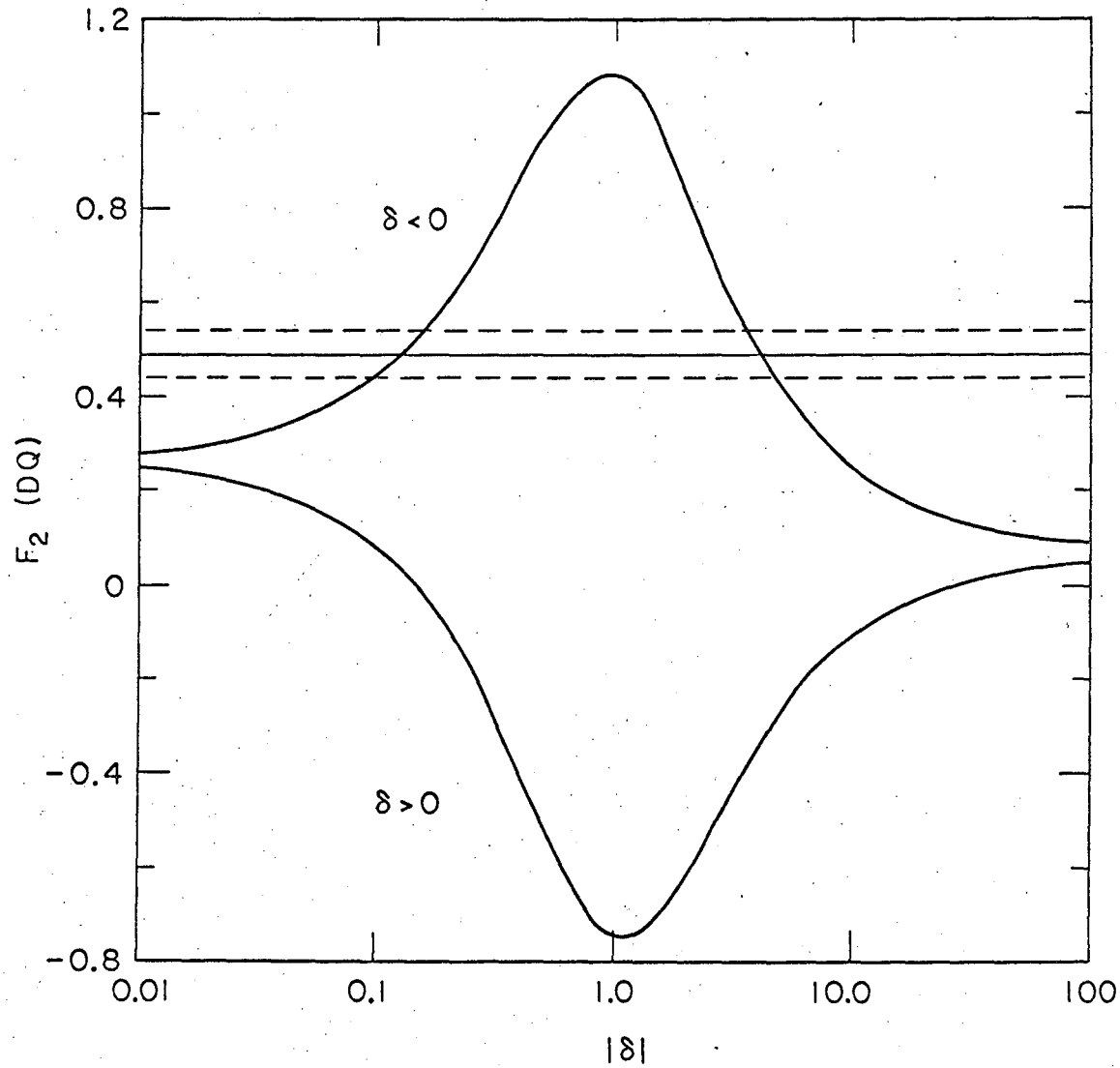

MU-36428

Fig. 35. Experimental F_2 and theoretical F_2 as a function of δ for the 174-keV transition in Hf^{177}.

$(g_K - g_R)/Q_0 = -0.047(11)$. Again using $Q_0 = 6.85$ we obtain $(g_K - g_R) = -0.322(75)$ and using $g_R = +0.203(34)$ as above we find $g_K = -0.12(8)$.

All members of a rotational band should have the same value of g_K. For the two cases calculated above we find that this is indeed the case for the $9/2^+[624]$ rotational band in Hf^{177}.

2. Relaxation Effects in Lu^{177m} Alignment

We have aligned Lu^{177m} in NES and in lanthanum ethylsulfate (LES) and studied the gamma-ray anisotropy in the presence and absence of an external magnetic field. A field of about 80 gauss was produced in the primary of the mutual inductance coils around the sample when the audio oscillator of the circuit was turned to its maximum amplitude. A field of up to 240 gauss could be produced by a coil wrapped around the outer dewar and connected to a bank of eight 6-volt storage batteries in series.

Lanthanum ethylsulfate is not a paramagnetic substance and consequently will not cool via adiabatic demagnetization techniques. Cooling was therefore achieved through thermal contact with magnetically cooled NES. We used a composite LES-NES crystal constructed as follows. Around a crystal of pure NES we grew a mixed layer about 1/4 mm thick varying from pure NES initially to pure LES at the surface. A further layer of pure LES about 1/4 mm thick was then added. A 1-mm layer was then grown from an LES solution containing some Lu^{177m} as impurity. Another 1/4 mm layer of pure LES was added and then another mixed layer which this time varied from pure LES initially to pure NES at the surface. The crystal was finished off with a 1-mm layer of pure NES. A small amount of Ce^{141} activity was grown into this outer NES layer so that the anisotropy of its 142-keV gamma ray could be used to monitor the temperature of at least the NES portion of the composite crystal.

The results of the experiments are shown in Table XIII. All gamma rays with $E_\gamma \geq 228$ keV in the decay of Lu^{177m} have about the same anisotropy. The anisotropies reported in Table XIII for Lu^{177m} represent an average over all prominent peaks in the spectrum with $E_\gamma \geq 228$ keV.

Table XIII. Gamma-ray anisotropy in NES and LES with and without an external magnetic field. The Lu^{177m} anisotropy is an average of the 208, 228, 281, 318, 327, 378, 413, and 418-keV gamma rays.

Lattice	External Magnetic Field* (gauss)	W(0) Lu^{177m}	W(0) Ce^{141}
Pure NES	0	0.789(6)	———
" "	240 DC	0.833(6)	———
Composite crystal	0	0.789(6)	1.150(3)
" "	80 AC	0.923(6)	1.112(3)
" "	150 DC	1.000(6)	———

*The DC field was provided by an external solenoid powered by a bank of storage batteries; the AC field was provided by the mutual inductance coils powered by the 20-cps audio oscillator.

For alignment in pure NES we observe that the gamma-ray anisotropy decreases slightly in the presence of a magnetic field. This is to be expected since the magnetic field warms the crystal somewhat. For alignment in the layered crystal, on the other hand, we note that in the presence of a magnetic field the Lu^{177m} anisotropy is almost completely destroyed while that of the Ce^{141} (which is in an NES layer) is decreased only slightly, evidencing a slight rise in temperature due to the magnetic field.

The following has been proposed as a possible explanation of these results.[82] The LES crystal is cooled by the transfer of heat from the LES to the NES layer. This heat transfer occurs mainly through interactions between magnetic impurity ions in the LES lattice. An equilibrium temperature is reached where the rate at which heat is transferred from the LES layer to the NES is equal to the rate at which heat is introduced to the LES layer from radioactive decay of the Lu^{177m}. When a magnetic field is applied, the above means of heat exchange is disrupted. The LES layer thus warms up from radioactive decay and consequently the anisotropy of the gamma rays disappears.

Further work on this problem would be very interesting. A quantitative interpretation of the methods of heat exchange through the ionic crystal will be especially useful.

ACKNOWLEDGEMENTS

Many others have contributed to this work, both directly and indirectly. In particular, I would like to thank Dr. D. A. Shirley who introduced me to these problems and who guided the work through to its conclusion.

Special thanks are also due Mr. George Killian and his staff, Mr. Gardiner G. Young, and his shop, Mrs. Wini Heppler, and Mrs. Gertrude Bolz for excellent technical assistance.

Also, my appreciation to Dr. Nicholas Stone, Dr. Eckart Matthias, and my fellow graduate students in the "Low Temperature" group for many pleasant and often beneficial discussions.

Finally, my thanks to my wife, Lorraine, for constant encouragement and typing of the manuscript.

This work was done under the auspices of the U. S. Atomic Energy Commission.

APPENDIX

The Decay of 5 1/2-hour Hf^{180}

The 5 1/2-hour isomeric state of Hf^{180} de-excites to the rotational band based on the 0^+ ground state.[72] The decay scheme is shown in Fig. 36. The relative intensity of each of the transitions in this simple decay is thus well-known. To obtain the relative gamma-ray intensities, however, we must correct the transition intensities for the internal conversion process. From the internal conversion tables of Rose,[73] the actual relative gamma-ray intensity of each transition was easily determined. These intensities are tabulated in Table XIV.

A source of Hf^{180m} was made by neutron bombardment of hafnium metal enriched in the isotope Hf^{179}. The irradiated source was readily dissolved in hydrofluoric acid, whereupon it was evaporated onto an aluminum counting plate. When the sample was counted care was taken not only to use the same Ge(Li) counter as was used for the Lu^{177m} count, but also to use essentially the same counter geometry and source strength. The spectrum thus obtained is shown in Fig. 37. The peaks were fitted with Gaussian curves after making suitable background corrections. From the intensities thus obtained and using the expected relative intensities of Table XIV, we obtained the counter efficiency curve shown in Fig. 38. The expected photoabsorption efficiency is also shown for reference. The discrepancy between the two curves is due to the possibility of reabsorption of some of the Compton-scattered photons in thick counters. These then appear as counts in the photopeak, thus increasing the counter efficiency for high-energy photons. This effect has been carefully studied in a recent paper by Ewan and Tavendale.[74]

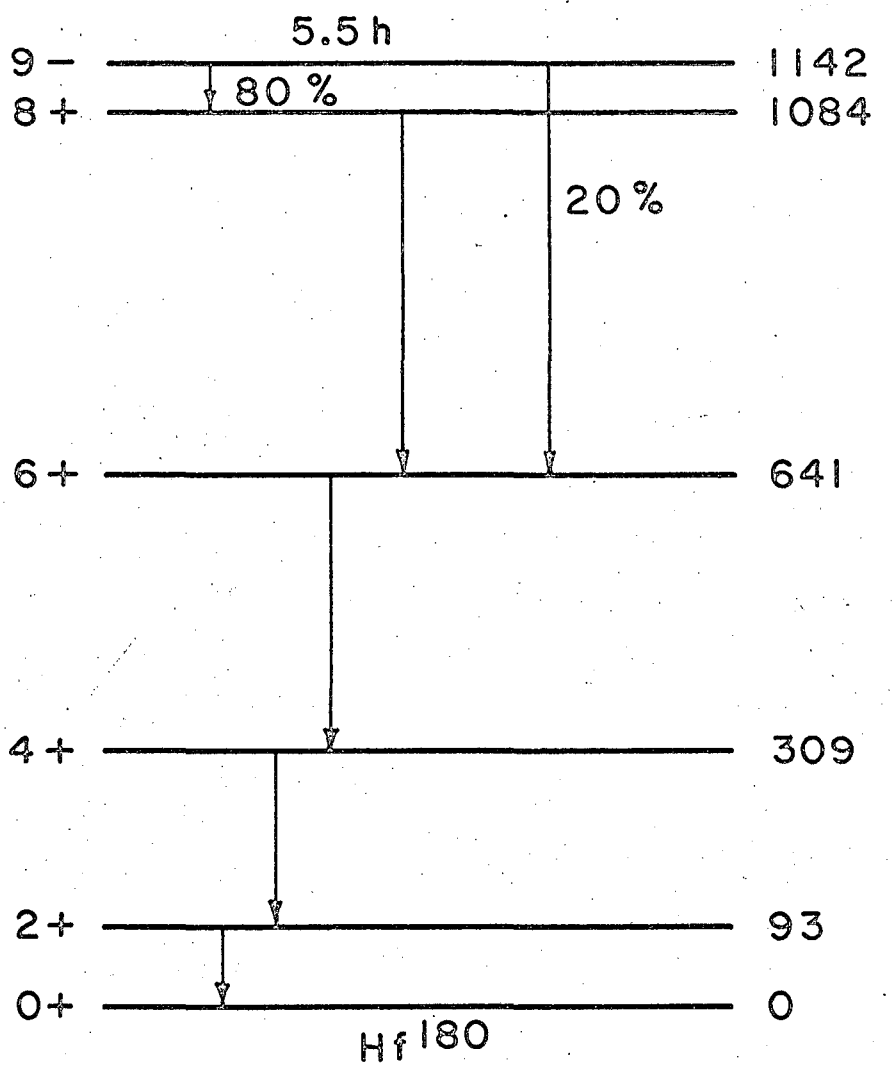

MU-36429

Fig. 36. The decay scheme of Hf^{180m}.

Table XIV. Gamma-ray relative intensities from the decay of Hf^{180m}.

Gamma Energy (keV)	Relative Intensity
94	1.00*
216	4.82
333	5.58
443	4.61
502	1.28

*Normalized to 1.00.

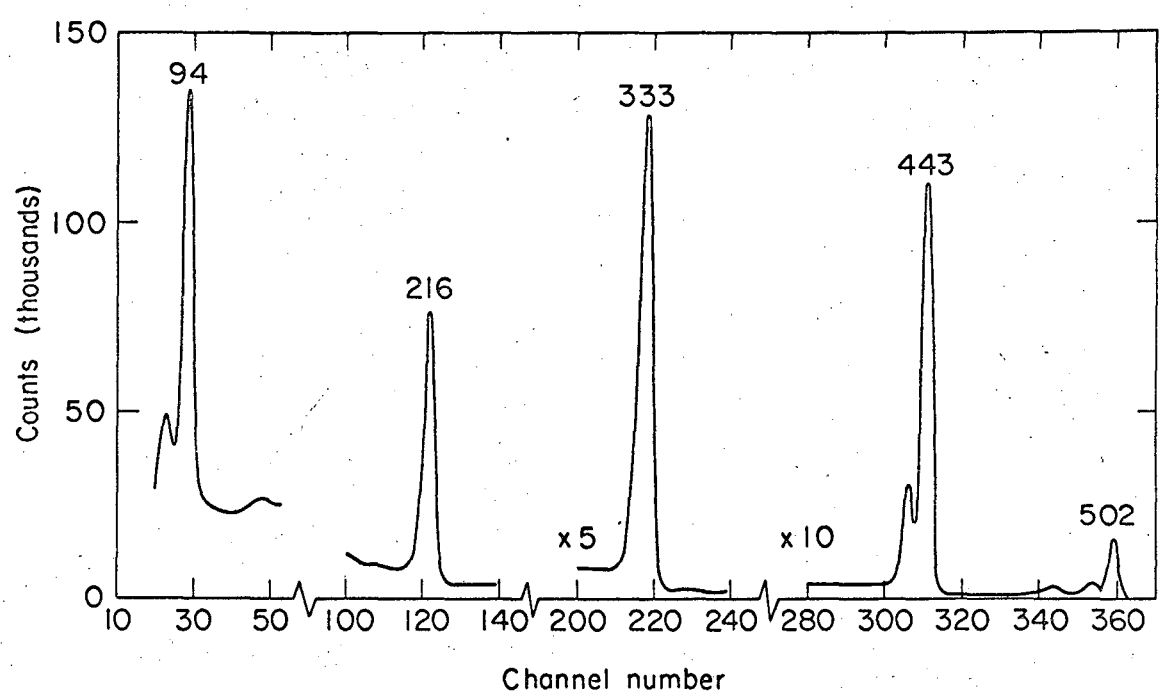

MU-36430

Fig. 37. Gamma-ray spectrum of Hf^{180m} obtained with a Ge(Li) detector. The peaks are identified by their energies in keV.

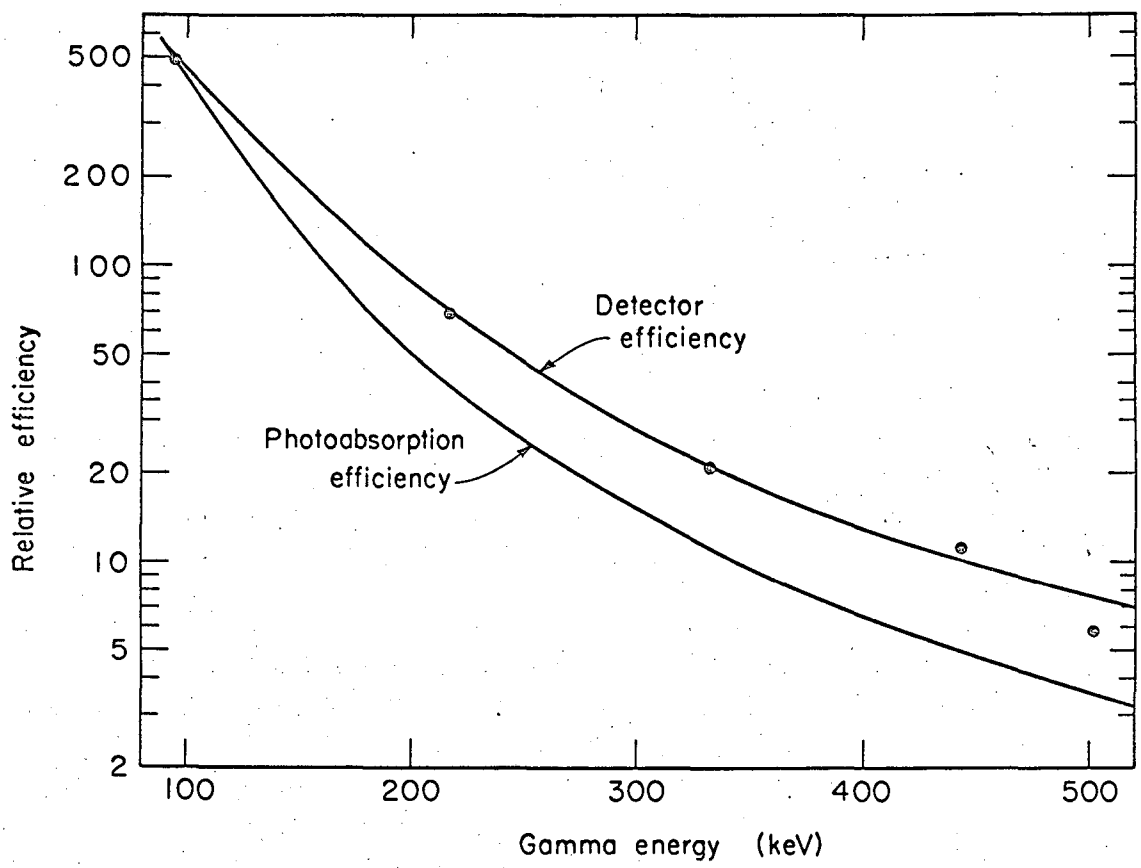

Fig. 38. Relative efficiency of the Ge(Li) detector used in Sec. VI.B. The discrepancy between this curve and the photoabsorption efficiency curve is explained in the text.

REFERENCES

1. R. M. Sternheimer, Phys. Rev. 80, 102 (1950).
   R. M. Sternheimer, Phys. Rev. 105, 158 (1957).
   R. M. Sternheimer, Phys. Rev. 84, 244 (1951).
   R. M. Sternheimer, Phys. Rev. 95, 737 (1954).
   R. M. Sternheimer and H. M. Foley, Phys. Rev. 102, 731 (1956).
   H. M. Foley, R. M. Sternheimer, and D. Tyko, Phys. Rev. 93, 734 (1954).
2. A. J. Freeman and R. E. Watson, Phys. Rev. 132, 706 (1963).
3. D. T. Edmonds, Phys. Rev. Letters 10, 129 (1963).
4. B. R. Judd, C. A. Lovejoy, and D. A. Shirley, Phys. Rev. 128, 1733 (1962).
5. A. Abragam and M. H. L. Pryce, Proc. Roy. Soc. (Lond.) A205, 135 (1951).
6. A. J. Freeman and R. E. Watson, Phys. Rev. 127, 2058 (1962).
7. B. R. Judd, Proc. Roy. Soc. (Lond.) A232, 458 (1955).
8. R. J. Blin-Stoyle and M. A. Grace, in Handbuch der Physik, edited by S. Flugge (Springer-Verlag Berlin, 1957) vol. 42, p. 555.
9. M. Jorgensen, O. B. Nielsen, and G. Sidenius, Phys. Letters 1, 321 (1962).
10. L. Kristensen, M. Jorgensen, O. B. Nielsen, and G. Sidenius, Phys. Letters 8, 57 (1964).
11. P. Alexander, F. Boehm, and E. Kankeleit, Phys. Rev. 133, B284 (1964).
12. J. Blok and D. A. Shirley, Phys. Letters 13, 232 (1964).
13. A. J. Tavendale, in Proc. Int. Symp. Nuclear Electronics, p. 235, Paris (1963).
14. F. S. Goulding, Nucleonics 22, 54 (1964).
15. N. Kurti, Il Nuovo Cimento Suppl. 6, 1101 (1957).
16. M. J. Steenland and H. A. Tolhoek, Orientation of Atomic Nuclei at Low Temperatures, in Progress in Low Temperature Physics, vol. II, edited by C. J. Gorter (North Holland Publishing Co., Amsterdam, 1957) p. 292.
17. C. J. Gorter, Physica 14, 504 (1948).
18. M. E. Rose, Phys. Rev. 75, 213 (1949).

19. B. Bleaney, Proc. Phys. Soc. (Lond.) A64, 315 (1951).
20. M. Ferentz and N. Rosenzweig, Argonne National Laboratory Report ANL-5324 (1955).
21. T. P. Gray and G. R. Satchler, Proc. Phys. Soc. (Lond.) A68, 349 (1955).
22. E. C. Ridley, Proc. Cambridge Phil. Soc. 56, 41 (1960).
23. K. Raynak, J. Chem. Phys. 37, 2440 (1962).
24. R. A. Erickson, L. D. Roberts, and J. W. T. Dabbs, Rev. Sci. Inst. 25, 1178 (1954).
25. E. G. Wikner and G. Burns, Phys. Letters 2, 225 (1962).
26. M. T. Hutchings and D. K. Ray, Proc. Phys. Soc. (Lond.) 81, 663 (1963).
27. R. E. Watson and A. J. Freeman, Phys. Rev. 135, A1209 (1964).
28. R. Behrsohn, J. Chem. Phys. 29, 326 (1958).
29. R. J. Elliott, Proc. Phys. Soc. (Lond.) 70B, 119 (1957).
30. J. A. A. Ketelaar, Physica 4, 619 (1937).
31. B. Bleaney, H. E. D. Scovil, and R. S. Trenam, Proc. Roy. Soc. (Lond.) A223, 15 (1954).
32. H. Meyer, Phil. Mag. 2, 521 (1957).
33. R. B. Frankel, Ph.D. Thesis, University of California, Department of Chemistry and Lawrence Radiation Laboratory, Berkeley, 1964 (unpublished).
34. C. E. Johnson, J. F. Schooley, and D. A. Shirley, Phys. Rev. 120, 2108 (1960).
35. A. Zalkin, J. D. Forrester, and D. H. Templeton, J. Chem. Phys. 39, 2881 (1963).
36. A. H. Cooke, H. J. Duffus, and W. P. Wolf, Phil. Mag. 44, 623 (1953).
37. J. M. Daniels and F. N. H. Robinson, Phil. Mag. 44, 630 (1953).
38. F. G. Brickwedde, H. Van Dyk, M. Durieux, J. R. Clement, and J. K. Logan, J. Res. Nat. Bur. Std. 64A, 1 (1960).
39. H. E. Gove and A. R. Rutledge, Chalk River Report CRP-755 (1958).
40. R. J. Elliott and K. W. H. Stevens, Proc. Roy. Soc. (Lond.) A219, 387 (1953).
41. J. B. Gruber, J. Chem. Phys. 38, 946 (1963).
42. D. A. Shirley and C. A. Lovejoy, Bull. Am. Phys. Soc. 6, 512 (1961).
43. S. S. Alpert, University of California Radiation Laboratory Report UCRL-9850

44. B. Bleaney, private communication (1963).
45. C. H. Townes, in Handbuch der Physik, edited by S. Flugge (Springer-Verlag, Berlin, 1958) vol. 38/1, p. 377.
46. A. Bohr and B. R. Mottelson, Kgl. Dan. Vid. Selsk., Mat. Fys. Medd. 27, no. 16 (1953).
47. O. Hansen, M. C. Olesen, O. Skilbreit, and B. Elbek, Nucl. Phys. 25, 634 (1961).
48. J. de Boer and J. D. Rogers, Phys. Letters 3, 304 (1963).
49. E. M. Bernstein and J. de Boer, Nucl. Phys. 18, 40 (1960).
50. R. M. Levy, Ph.D. Thesis, University of California, Department of Chemistry and Lawrence Radiation Laboratory, Berkeley, 1964 (unpublished).
51. W. H. Kelly and M. L. Wiedenbeck, Phys. Rev. 102, 1130 (1956).
52. Y. Ting, Phys. Rev. 108, 295 (1957).
53. R. G. Barnes, R. L. Mossbauer, E. Kankeleit, and J. M. Poindexter, Phys. Rev. 136, A175 (1964).
54. C. J. Lenander and E. Y. Wong, J. Chem. Phys. 38, 2750 (1963).
55. D. K. Ray, Proc. Phys. Soc. (Lond.) 82, 47 (1963).
56. R. E. Watson and A. J. Freeman, Phys. Rev. 133, A1571 (1964).
57. G. Burns, Phys. Rev. 128, 2121 (1962).
58. R. M. Sternheimer, Phys. Rev. 132, 1637 (1963).
59. R. E. Watson and A. J. Freeman, Phys. Rev. 135, A1209 (1964).
60. S. Hufner, Z. Physik 169, 417 (1962).
61. B. R. Judd, Mol. Physics 2, 407 (1959).
62. E. H. Erath, J. Chem. Phys. 34, 1985 (1961).
63. E. Y. Wong and I. Richman, J. Chem. Phys. 34, 1182 (1961).
64. J. R. Hull and R. A. Hull, J. Chem. Phys. 9, 465 (1941).
65. N. Kurti and F. E. Simon, Proc. Roy. Soc. (Lond.) A152, 21 (1935).
66. D. L. Mumaugh, COILS- magnetic properties of current systems using elliptic integrals, University of California, Radiation Laboratory Computer Library, Berkeley (1963).
67. N. J. Stone, private communication (1965).
68. B. R. Mottelson and S. G. Nilsson, Mat-fys. Skr. Dan Vid. Selsk. 1, no. 8 (1959).

69. A. J. Tavendale and G. T. Ewan, Nucl. Inst. and Methods 25, 185 (1963).

70. E. Bodensted, P. Meyer, L. Schanzler, M. Forker, H. Wagner, and J. Radeloff, Physikalische Verhandlungen 5, 87 (1965).

71. S. Devons and L. J. B. Goldfarb, in Handbuch der Physik, edited by S. Flugge (Springer-Verlag, Berlin, 1957) vol. 42, p. 362.

72. Landolt-Bornstein Numerical Data and Functional Relationships in Science and Technology, New Series, ed, K. H. Hellwege, group I, vol. 1 (Springer-Verlag, Berlin, 1961).

73. S. S. Alpert, University of California, Radiation Laboratory Report UCRL-9850.

74. G. T. Ewan and A. J. Tavendale, Can. J. Phys. 42, 2286 (1964).

75. Yu. T. Grin' and I. M. Pavlichenkov, Soviet Physics JETP 14, 679 (1962).

76. S. G. Nilsson, Mat. Fys. Medd. Dan. Vid. Selsk. 29, no. 16 (1955).

77. J. O. Rasmussen and L. W. Chiao, Proc. of the Int. Conf. on Nuclear Structure, Kingston, Canada, (University of Toronto Press, 1960) p. 646.

78. W. W. Black and A. C. G. Mitchell, Phys. Rev. 132, 1193 (1963).

79. S. Ofer, Phys. Rev. 114, 870 (1959).

80. N. I. Kaliteevskii, M. P. Chaika, I. Kh. Pacheva, and E. E. Frudkin, Soviet Physics JETP 10, 629 (1960).

81. R. B. Frankel, D. A. Shirley, and N. J. Stone, Phys. Rev. 136, B577 (1964).

82. C. Jeffries, private communication to D. A. Shirley.

83. W. H. Kelley and M. L. Wiedenbeck, Phys. Rev. 102, 1130 (1956).

84. H. H. Bolotin, C. H. Pruett, P. L. Roggenkamp, and R. G. Wilkinson, Phys. Rev. 99, 62 (1955).

85. G. P. Bishop and J. P. Perez y Jorba, Phys. Rev. 98, 89 (1955).

86. R. C. Bannerman, G. W. Lewis, and S. C. Curran, Phil. Mag. 42, 1097 (1951).

87. R. M. Sternheimer, Bull. Am. Phys. Soc. 10, 597 (1965).

88. K. D. Bowers and J. Owen, Reports on Progress in Physics 18, 304 (1955).

89. D. T. Edmonds, private communication to D. A. Shirley (1964).

90. H. H. Wickman, private communication (1965).

91. W. Low, Phys. Rev. 103, 1309 (1956).

This report was prepared as an account of Government sponsored work. Neither the United States, nor the Commission, nor any person acting on behalf of the Commission:

A. Makes any warranty or representation, expressed or implied, with respect to the accuracy, completeness, or usefulness of the information contained in this report, or that the use of any information, apparatus, method, or process disclosed in this report may not infringe privately owned rights; or

B. Assumes any liabilities with respect to the use of, or for damages resulting from the use of any information, apparatus, method, or process disclosed in this report.

As used in the above, "person acting on behalf of the Commission" includes any employee or contractor of the Commission, or employee of such contractor, to the extent that such employee or contractor of the Commission, or employee of such contractor prepares, disseminates, or provides access to, any information pursuant to his employment or contract with the Commission, or his employment with such contractor.